ALGORITHM THEORETICAL BASIS DOCUMENT (ATBD)
FOR THE
THE AMSR-E SEA ICE ALGORITHM

Donald J. Cavalieri
Laboratory for Hydrospheric Processes
NASA Goddard Space Flight Center
Greenbelt, Maryland 20771
Phone (301) 614-5901
Fax (301) 614-5644
email: Donald.J.Cavalieri.1@gsfc.nasa.gov

and

Josefino C. Comiso
Laboratory for Hydrospheric Processes
NASA Goddard Space Flight Center
Greenbelt, Maryland 20771
Phone (301) 614-5708
Fax (301) 614-5644
email: comiso@joey.gsfc.nasa.gov

December 1, 2000

Table of Contents

1.0 Introduction

Polar sea ice is a vital component of the global climate system because of its high albedo, its low heat conductivity which limits the exchange of heat between ocean and atmosphere, and its role in altering oceanic water mass properties and circulation. The high albedo of sea ice, which ranges from about 80% (Grenfell, 1983) to 98% (Vowinckel and Orvig, 1970), relative to that of the open ocean (10% to 15%) results in a sharp contrast in surface energy flux at the edge of the ice pack. This abrupt change in energy exchange can, under appropriate conditions, affect atmospheric circulation and give rise to violent weather systems known as polar lows (Carleton, 1985; Businger and Reed, 1989; Gloersen et al., 1989). Atmospheric general circulation model studies suggest an association between heavy and light ice years and larger-scale general atmospheric circulation changes (Honda et al., 1996).

As an effective insulator, sea ice with its snow cover limits the exchange of energy and momentum between the ocean and atmosphere. For example, in winter, the heat flux in an open lead exceeds by two orders of magnitude the heat flux through an adjacent thick ice cover (Badgley, 1966; Maykut, 1978). Sea ice also influences oceanic structure and circulation through the production of cold, saline dense water during ice growth. The cold, dense water formed from sea ice growth in Arctic coastal polynyas helps maintain the Arctic Ocean halocline (Aagaard et al., 1981; Cavalieri and Martin, 1994). This dense water can also induce convection and deepen the mixed layer. A large fraction of world's deep and bottom water is believed to be formed at polar latitudes (Stommel, 1962; Gordon, 1978; Killworth, 1983). Among the key sources of bottom water are the coastal polynyas in the Antarctic (Zwally et al., 1985; Comiso and Gordon, 1999; Thorsten et al., 1999) and the Odden in the Greenland Sea (Schuman et al., 1998; Comiso et al., in press) which are regarded as sea ice factories.

Current interest in long-term sea ice changes results from the observed increase of CO_2 in the atmosphere. Because of expected feedback effects, the anticipated global warming from an increase in CO_2 was postulated to be amplified in the polar regions (Budyko, 1966). Some coupled ocean-atmosphere model results (e.g., Manabe and Stoufer, 1994) suggest that a doubling of CO_2 would lead to a significant thinning and reduction in the extent of the Arctic sea ice cover, especially during the summer periods. A long-term, large-scale characterization of the global sea ice cover is needed for sea ice trend studies and for climate model validation studies. The most consistent source of such data continues to be satellite passive microwave sensors (Zwally et al., 1983; Parkinson et al., 1987, 1999; Gloersen et al., 1992). Visible and infrared satellite data (e.g., AVHRR) are not as useful because coverage is limited by persistent cloud cover, but nevertheless, they have higher resolution and have used for mesoscale studies on surface temperature, albedo, and cloud statistics (Key, 1998; Comiso, 2000; Comiso, in press). Detailed characterization of sea ice under all weather conditions has recently been provided by the ERS-1 and JERS-1 synthetic aperture radar (SAR) data, but only a small fraction of the entire ice cover can be monitored at a time because of operational and data acquisition constraints and a narrow swath width (100 km). Radarsat data with its wider swath (500 km) is an improvement but adequate temporal resolution is still lacking. Such data are nonetheless useful for regional studies and may provide information to improve the interpretation of passive microwave data.

The principal quantitative measure of the global sea ice cover is sea ice concentration. It is this parameter that continues to be produced routinely from satellite passive microwave systems for both global change research and operational requirements. In addition to sea ice concentration, other sea ice parameters that are important to the accurate determination of surface energy fluxes are snow depth on sea ice and the physical temperature of the ice. The surface heat flux through sea ice critically depends on the depth of snow which is a very effective insulator. While snow fall is an externally prescribed quantity in sea ice models, there is nevertheless a need for information on the distribution of snow depth on sea ice to permit modelers to determine whether observed biases in simulated sea ice (e.g. thickness) can be attributed to biases in the climatologically prescribed snowfall (Preller et al., 1992).

Another major source of uncertainty in energy balance calculations is ice surface temperature. Direct measurement of ice surface temperature is particularly valuable for ice prediction models (Preller et al., 1992). The monitoring of long-term changes in ice temperature may also provide valuable information about changes in the thickness of the ice and its snow cover. AVHRR ice surface temperature algorithms have been developed (e.g., Comiso, 1983; Schluessel and Grassl, 1990; Key, 1998; Comiso, 2000), and although coverage is limited by the presence of clouds as noted earlier, they provide the only spatially detailed information about the snow surface over ice. Monthly surface temperatures from AVHRR data have been shown to agree with in situ surface temperature data to within 3 K (Comiso, 2000). For the seasonal sea ice cover, the sea ice temperature measured by microwave radiometers represents the snow/ice interface temperature, whereas in the perennial sea ice regions, it represents approximately the average temperature of the freeboard layer of the ice. When combined with the snow depth measurements, ice temperature data from microwave data, and surface snow temperature from infrared data would considerably reduce current uncertainties in polar energy budgets.

The AMSR-E system as configured to be launched on board the EOS-Aqua satellite will be a significant improvement over previous and current passive microwave systems. The most obvious improvements are its finer spatial resolution and its wider spectral range. This capability will allow an improved determination of our three standard products: total sea ice concentration, snow depth on sea ice, and sea ice temperature. The AMSR-E sea ice algorithms presented below will provide daily maps of sea ice concentration and sea ice temperature, and 5-day-averaged maps of snow depth.

The objectives of this document are (a) to describe the standard sea ice products that will be derived from AMSR-E, (b) to provide the theoretical basis of the algorithms that will produce these products, and (c) to assess the accuracy of these products. Since the previous ATBD, written in November 1997, significant improvements have been made to the algorithms. These revisions are described in section 3.

2.0 Overview and Background Information

2.1 Historical Perspective

The first global view of sea ice was achieved in the early 1960s with the launch of earth-viewing satellite sensors such as those aboard the Nimbus, Tiros, and Earth Resources and

Technology (ERTS, later, Landsat) satellites. Because these sensors operated in the visible and infrared bands of the electromagnetic spectrum, they were limited to cloud-free and well-illuminated regions only, making them incapable of providing the synoptic observations of the Earth's surface needed for monitoring the polar sea ice covers.

Microwave sensors, not limited by weather conditions or light levels, are particularly well suited for monitoring sea ice, because of the strong contrast in thermal microwave emission between areas of ice-free ocean and ice-covered waters. The first passive microwave sensor used extensively for studying the global distribution of sea ice was the Electrically Scanning Microwave Radiometer (ESMR) on board the NASA Nimbus 5 satellite (Gloersen et al., 1974; Zwally et al., 1983). The single channel ESMR, operating at 19.35 GHz, provided daily coverage of the polar regions and allowed for the first time synoptic observations of sea ice concentration needed for undertaking a detailed study of global sea ice variability. The ESMR sea ice algorithm was based on a linear relationship between the radiometric brightness temperatures of ice-free water and consolidated sea ice. Temperature variability effects were reduced using climatological data. At the ESMR frequency the contrast between ice and water is ~100 K. Although the estimated accuracy was only 15% (Comiso and Zwally, 1982), these data were used successfully to document sea ice changes in both hemispheres (Zwally et al.,1983; Parkinson et al., 1987).

The Scanning Multichannel Microwave Radiometer (SMMR) was launched on the SeaSat satellite in July 1978 and on the Nimbus-7 satellite in October 1978 (Gloersen and Barath, 1977; Gloersen et al. 1992). With its multichannel capability, SMMR provided more information about the ice cover than ESMR. Multichannel SMMR algorithm provided an opportunity to derive sea ice concentrations more accurately (Svendsen et al., 1983; Cavalieri et al., 1984; Comiso et al., 1984; Swift et al., 1985; Comiso, 1986). Others also extended their algorithm to include the discrimination of two ice types (first-year and multiyear) in the Arctic (Svendsen et al., 1983; Cavalieri et al., 1984; Swift et al., 1985) and the determination of sea ice temperature (Gloersen et al., 1992). The various algorithms take advantage of two or more channels to reduce errors associated with physical temperature variability, emissivity anomalies, and weather effects.

In 1987, the first in a new series of passive microwave radiometers was launched as part of the Defense Meteorological Satellite Program (DMSP). This sensor, called the Special Sensor Microwave/Imager (SSMI), operates at frequencies ranging from 19.4 GHz to 85.5 GHz. The SSMI measures both horizontally and vertically polarized components at all frequencies except at 22.2 GHz for which only a vertically polarized component is obtained. Using these data, several new algorithm improvements have been made (e.g., Cavalieri, 1994; Comiso, 1995, Markus and Cavalieri, 1998; 2000).

The AMSR-E sensor, which will have a wider range of frequencies and an improved spatial resolution, should provide the basis for improving the current suite of sea ice algorithms and for developing a new generation of algorithms.

2.2 AMSR-E Instrument Characteristics

The EOS-Aqua AMSR-E is a twelve channel, six frequency total power passive microwave radiometer system. It measures vertically and horizontally polarized radiances at 6.925, 10.65, 18.7,

23.8, 36.5, and 89.0 GHz. The instrument, modified from the design used for the ADEOS-II AMSR, consists of an offset parabolic reflector 1.6 m in diameter, fed by an array of six feedhorns. The AMSR-E rotates continuously at 40 rpm about an axis parallel to the local spacecraft vertical. At an altitude of 705 km, it measures the upwelling scene brightness temperatures over an angular sector of + 61^{o} about the sub-satellite track, resulting in a swath width of 1445 km. During a period of 1.5 seconds the spacecraft sub-satellite point travels 10 km. Even though the instantaneous field-of-view (IFOV) for each channel is different, active scene measurements are recorded at equal intervals of 10 km (5 km for the 89 GHz channels) along the scan. The half-cone angle at which the reflector is fixed is 47.4 ^{o} which results in an Earth incidence angle of 55.0 ^{o}. Table 1 lists the pertinent performance characteristics

The radiometer calibration error budget, exclusive of antenna pattern correction effects, is composed of three major contributors: warm load reference error, cold load reference error, radiometer electronics nonlinearities and errors. An estimate of the warm load reference error is ~0.5 K, based on the RSS of the various components. The error in the cold reference measurement is mainly produced by the error in coupling between the cold sky reflector and the feedhorn. This is estimated to be ~0.5 K. The radiometer electronics nonlinearity results in an error that can be estimated during the thermal vacuum calibration testing (on SSMI this error was ~0.4 K). A source of error in the receiver electronics is the gain drift resulting from temperature variations over one orbit. This error depends on the design of the receiver and overall design of the sensor. The gain drift can be as much as ~0.24 K for a temperature variation of less than 10 K over one orbit. Accounting for all errors, the total sensor bias error is 0.66 K at 100 K and changes with temperature to 0.68 K at 250 K.

Table 1. EOS PM-1 AMSR-E SENSOR PERFORMANCE CHARACTERISTICS

CHARACTERISTICS	CENTER FREQUENCIES (GHz)					
	6.9	10.7	18.7	23.8	36.5	89.0
BANDWIDTH (MHz)	350	100	200	400	1000	3000
SENSITIVITY (K)	0.3	0.6	0.6	0.6	0.6	1.1
IFOV (km x km)	76x44	49x28	28x16	31x18	14x8	6x4
SAMPLING RATE (km x km)	10x10	10x10	10x10	10x10	10x10	5x5
INTEGRATION TIME (ms)	2.6	2.6	2.6	2.6	2.6	1.3
MAIN BEAM EFFICIENCY (%)	95.3	95.0	96.3	96.4	95.3	96.0
BEAMWIDTH (degrees)	2.2	1.4	0.8	0.9	0.4	0.18

2.3 Standard Products

The standard products for sea ice are those deemed essential to meet the overall objectives of NASA's MTPE. These are Level 3 sea ice concentration, sea ice temperature, and snow depth on sea ice (Table 2). These products will be mapped to a standard polar grid currently used for the SSMI (NSIDC, 1992). The grid resolutions for the AMSR-E brightness temperatures and sea ice concentrations were selected to take advantage of the full spatial resolution of the AMSR-E, while still providing continuity with similar data products spanning 20 years from SMMR and SSMI.

Table 2. AMSR-E LEVEL 3 TB and SEA ICE PRODUCTS

PARAMETER	APPROX. FOOTPRINT SIZE	GRID RESOL.	TEMPORAL RESOL.
TBs (H&V POL.)			
6.9	58 KM	25.0 KM	ASCEND., DESCEND. & DAILY
10.7	37 KM	25.0 KM	ASCEND., DESCEND. & DAILY
18.7, 23.8,	21 KM	25.0, 12.5 KM	ASCEND.,DESCEND. & DAILY
36.5	11 KM	25.0, 12.5 KM	ASCEND., DESCEND. & DAILY
89.0	5 KM	25.0, 12.5, 6.25 KM	ASCEND., DESCEND. & DAILY
25-km SEA ICE PRODUCTS			
SEA ICE CONC.			
Antarc. (Bootstrap)		25 KM	ASCEND., DESCEND. & DAILY
Antarc. (NASA Team-Bootstrap)		25 KM	ASCEND., DESCEND. & DAILY
Arctic (NASA Team)		25 KM	ASCEND., DESCEND. & DAILY
Arctic (Bootstrap-NASA Team)		25 KM	ASCEND., DESCEND. & DAILY
SEA ICE TEMP. Arctic & Antarc.		25 KM	ASCEND., DESCEND. & DAILY
12.5-km SEA ICE PRODUCTS			
SEA ICE CONC.			
Antarc. (Bootstrap)		12.5 KM	ASCEND., DESCEND. & DAILY
Antarc. (NASA Team-Bootstrap)		12.5 KM	ASCEND., DESCEND. & DAILY
Arctic (NASA Team)		12.5 KM	ASCEND., DESCEND. & DAILY
Arctic (Bootstrap-NASA Team)		12.5 KM	ASCEND., DESCEND. & DAILY
SNOW DEPTH Arctic & Antarc.		12.5 KM	5-DAY AVERAGE

NOTES:

(a) The AMSR-E sampling rate is 10x10 km for the 6.9GHz to 36.5 GHz channels and is 5x5 km for the 89 GHz channels.

(b) The AMSR-E Level 2A brightness temperature data are used as input for gridding to the standard “SSMI” grid at resolutions of 25-km, 12.5-km and 6.25-km. Level 2A brightness temperature data have been convolved using the Backus-Gilbert method to provide the spatial averaging. Observations at 6 and 10 GHz are produced at a spatial interval of approximately 20-km and at the sensor sampling rate for the other frequencies.

These products will be generated using three algorithms: the first is based on a modified NASA Team algorithm, the second is a modified Bootstrap algorithm that calculates both sea ice concentration and surface ice temperature, and the third is an algorithm for determining snow depth on sea ice. In the Arctic, the modified NASA Team algorithm will be used to provide the standard sea ice concentration along with the difference between the Bootstrap and NASA Team concentrations. In the Antarctic, the modified Bootstrap algorithm will provide the standard concentration product and the difference between the NASA Team and the Bootstrap concentrations will be provided. The ice temperature will be produced from the Bootstrap algorithm for both hemispheres (Comiso and Zwally, 1998) and snow depth will be produced from the algorithm described by Markus and Cavalieri (1998) for both hemispheres excluding the Arctic perenial ice region. Accuracies of all these products will be determined with the aid of a comprehensive validation program described in section 5. In addition to the sea ice parameters, gridded brightness temperatures will also be provided at grid resolutions commensurate with the Level 2A spatially-averaged data (Table 2).

3.0 Algorithm Description and Theoretical Basis

The proposed multichannel AMSR-E sea ice algorithms build on our experience with the Nimbus 7 SMMR and the DMSP SSMI sensors and on the expected configuration of the AMSR-E sensor itself. . The block diagram shown in Figure 1 illustrates the overall plan for computing the standard

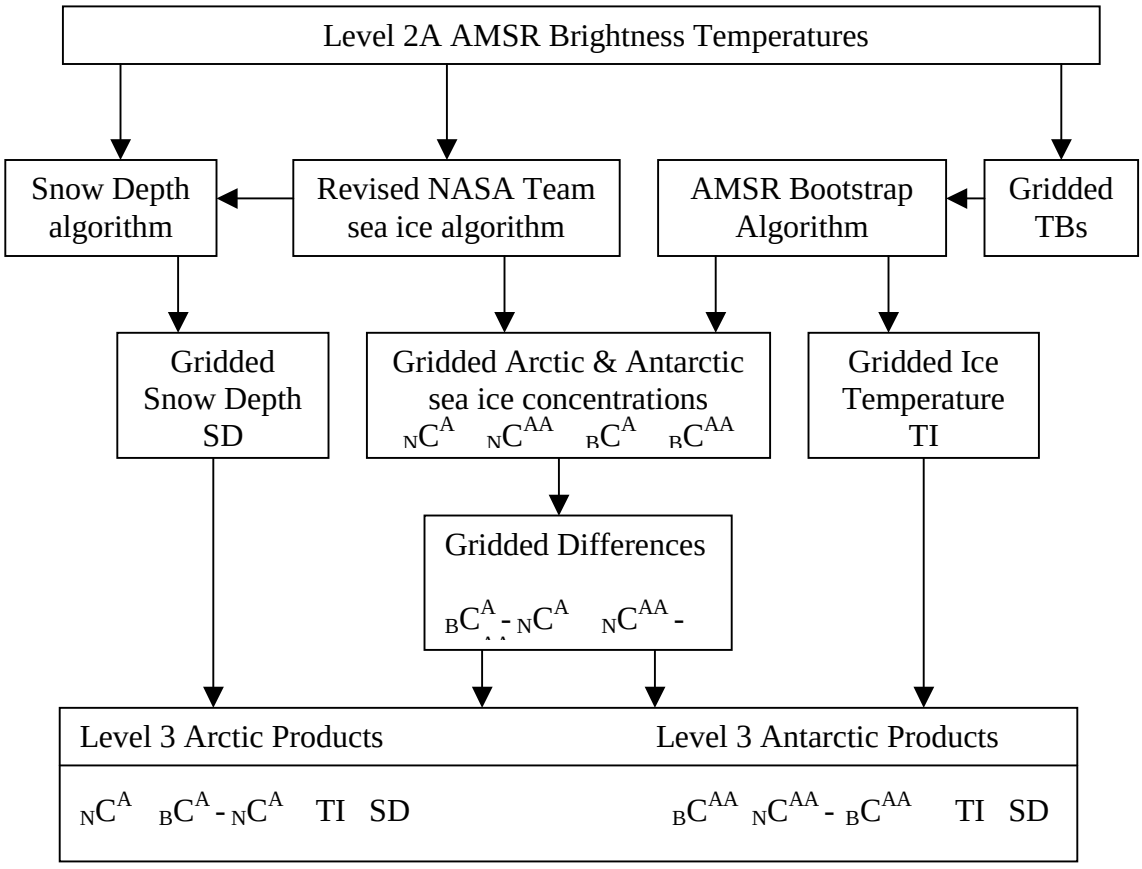

Figure 1. AMSR-E Sea Ice Data Flow Chart

AMSR-E sea ice products. The enhanced NASA Team algorithm (Markus and Cavalieri, 2000) and the revised Bootstrap algorithm are described in the following sections. The physical basis of the sea ice temperature algorithm is similar to that used in Gloersen et al. (1992) but the implementation is different (e.g., temperatures where ice concentration is less than 80% are not set to 271 K) as will be discussed in a later section. Snow depths will be calculated for the entire Antarctic sea ice pack and for Arctic seasonal sea ice zones. The rationale for this Arctic limitation is discussed in section 3.3.

3.1 Sea Ice Concentration

The principal sea ice parameter derived from AMSR-E brightness temperatures is sea ice concentration. It is this product that enables the spatial characterization of the sea ice cover and the calculation of sea ice extent and area that are used in long-term trend analyses and processes studies (Zwally et al., 1983, Gloersen et al., 1992, Parkinson et al., 1987, Cavalieri et al., 1997, Parkinson et al., 1999, Gloersen et al., 1999). The calculation of the two other standard products, ice temperature and snow depth on sea ice, also requires sea ice concentration as input. All three products are important to the calculation of the surface heat exchange which affects global atmospheric and oceanic circulations.

Historically, the two basic assumptions made in the development of sea ice concentration algorithms are (1) that the received radiation by the satellite sensor comes from two polar ocean surfaces: sea ice (I), and ice-free (open) water (W), and (2) that the atmospheric contribution is approximately constant. As will be discussed in the next section, the enhanced NASA Team algorithm allows for three ice types and a varying atmosphere. The selection of algorithm coefficients (tie-points) is based on observed brightness temperatures which include an atmospheric component. Weather filters are employed to eliminate spurious sea ice concentrations over open ocean resulting from a varying atmospheric emission.

Using a linear mixing formulation, the received radiation expressed as a brightness temperature is given by

$$TB = TB_W C_W + TB_I C_I \qquad (1)$$

where TB_W and TB_I are the brightness temperatures of ice-free ocean and sea ice. C_W and C_I are the corresponding fractions of each of the two ocean surface components within the field-of-view of the instrument and add to unity. The two sea ice concentration algorithms described make use of Equation (1), but the sets of channels and the form of the algorithms used to derive C_I are different as will be discussed in the following sections. It should be noted that none of these algorithms have been tested with actual AMSR data. Further algorithm refinements are thus anticipated when the actual AMSR data are used.

3.1.1 Revised NASA Team Algorithm

The physical basis for distinguishing among the three polar ocean components (open ocean and two ice types) is best described by considering the brightness temperature spectra of Arctic polar ocean surfaces shown in Figure 2. Examination of this figure illustrates two important

characteristics. First, the difference between the vertically and horizontally polarized radiances is small for either first-year (FY) or multiyear (MY) ice in comparison to that for the ocean. Second, the discrimination between ice types increases with decreasing wavelength (increasing frequency).

In particular, discrimination between FY and MY ice is greater at 0.8 cm (37 GHz) than it is at 1.7 cm (18 GHz). These characteristics are parameterized in terms of two independent variables, the polarization (PR) and the spectral gradient ratio (GR), defined by:

$$PR(19) = (TB(19V)-TB(19H))/(TB(19V)+TB(19H)) \quad (2)$$

$$GR(37V/19V) = (TB(37V)-TB(19V))/(TB(37V)+TB(19V)) \quad (3)$$

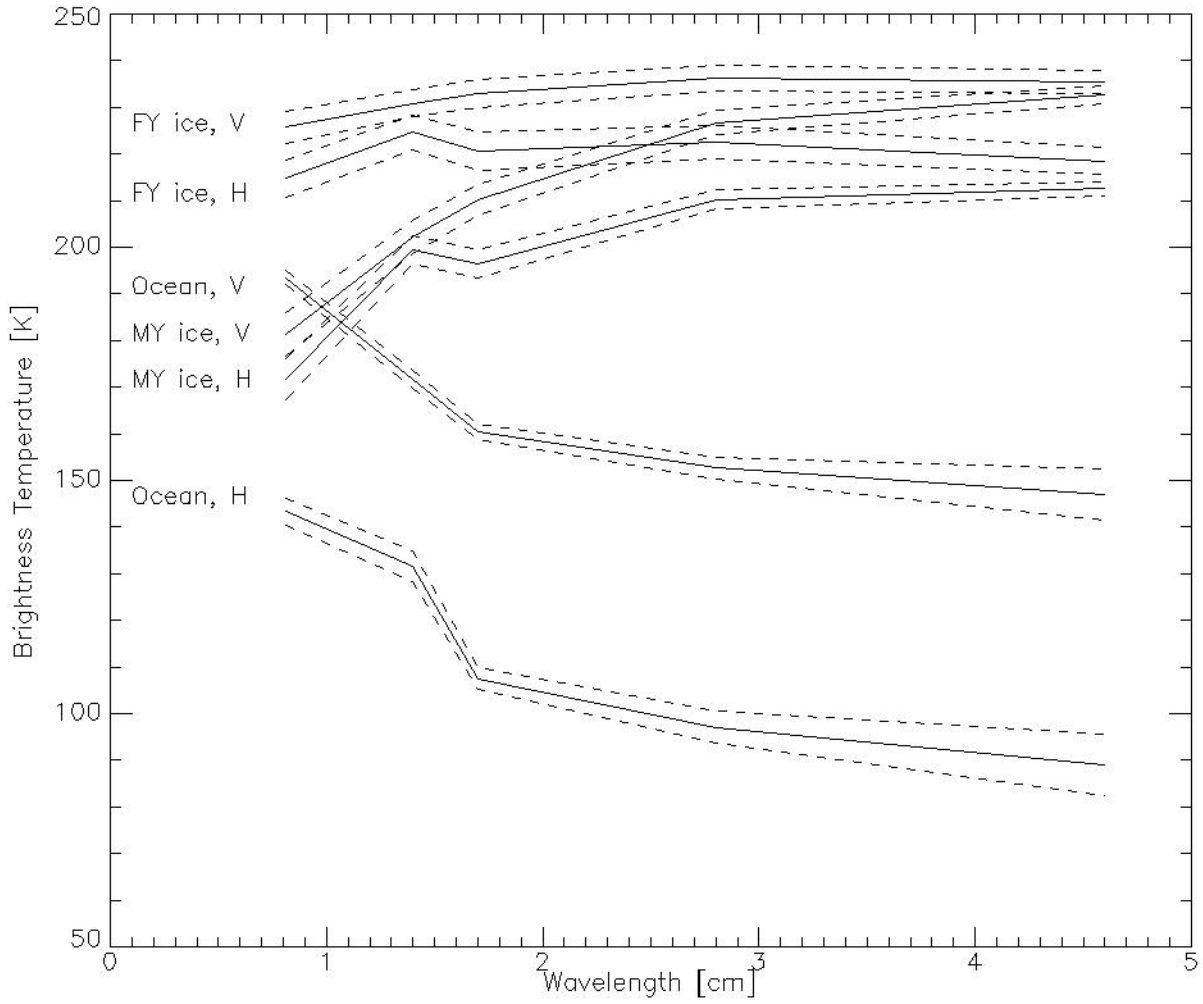

Figure 2. Microwave spectra of first-year and multiyear sea ice and ice-free ocean for horizontal and vertical polarizations. The plotted values represent the mean ±1 standard deviation (data from Cavalieri et al., 1984).

These variables have been shown to have the same functional form as principal components and differ only in that these variables are normalized (Rothrock et al., 1988). An advantage of using normalized principal components is that they are less susceptible to geophysical crosstalk. Another advantage of these variables is that they are largely independent of ice temperature variations, which eliminates the problem of estimating ice temperature variability both temporally (e.g., day-to-day and seasonal) and spatially (e.g., temperature gradients across the Arctic basin).

In the revised NASA Team sea ice algorithm as in the original NASA Team sea ice algorithm the two ratios of brightness temperatures used are the polarization and the spectral gradient ratio defined by equations (2) and (3). The NASA Team algorithm identifies two ice types which are associated with first-year and multiyear ice in the Arctic and ice types A and B in the Antarctic. A PR(19) versus GR(37V19V) scatter plot for the Weddell Sea region on September 15, 1992 is shown in Figure 3a. The A-B line represents 100% ice concentration. The distance from the open water point (OW) to line A-B is a measure of the ice concentration. In the NASA Team algorithm, the primary source of error in wintertime Antarctic sea ice concentration retrievals is attributed to conditions in the surface layer such as surface glaze and layering [Comiso et al., 1997], which can significantly affect the horizontally polarized 19 GHz brightness temperature [Matzler et al., 1984]. These surface effects lead to increased PR(19) values which result in underestimates of ice concentration. In Figure 3a, pixels with significant surface effects create a cloud of points under representing ice concentrations (labeled C). The use of the SSMI horizontally polarized channels makes it imperative to resolve a third ice type to overcome the difficulty of surface effects on the emissivity of the horizontally polarized component.

3.1.1.1 Approach

The revised NASA Team algorithm approach makes use of the 85 GHz channels, because the horizontally polarized 85 GHz data are much less affected by surface effects than the horizontally polarized 19 GHz data [Matzler et al., 1984]. Furthermore, the 85 GHz channels have successfully been used in sea ice concentration retrievals under clear atmospheric conditions [Lubin et al., 1997]. Here we use the 85 GHz channels together with a forward radiative transfer model to provide weather-corrected ice concentrations.

Starting with the NASA Team PR(19)-GR(37V19V) domain (Figure 3a), we rotate the axes by $\phi 19$, the angle between the GR-axis and the A-B line (FY-MY line for the Arctic). With the A-B line now vertical, the rotated PR is defined by

$$PR_R(19) = - GR(37V19V)\sin(\phi) + PR(19)\cos(\phi) \qquad (4)$$

and is independent of ice types A and B as defined by the tieponts shown in Figure 3. A similar rotation is also done in the PR(85)-GR(37V19V) domain (not shown). The angles expressed in radians are given in Table 3.

Table 3. Angles in radians between the GR-axis and the A-B line (FY-MY line for the Arctic) for the PR(19)-GR(37V19V) domain and the PR(85)-GR(37V19V) domain.

Hemisphere	ϕ19	ϕ85
Antarctic	-0.59	-0.40
Arctic	-0.18	-0.06

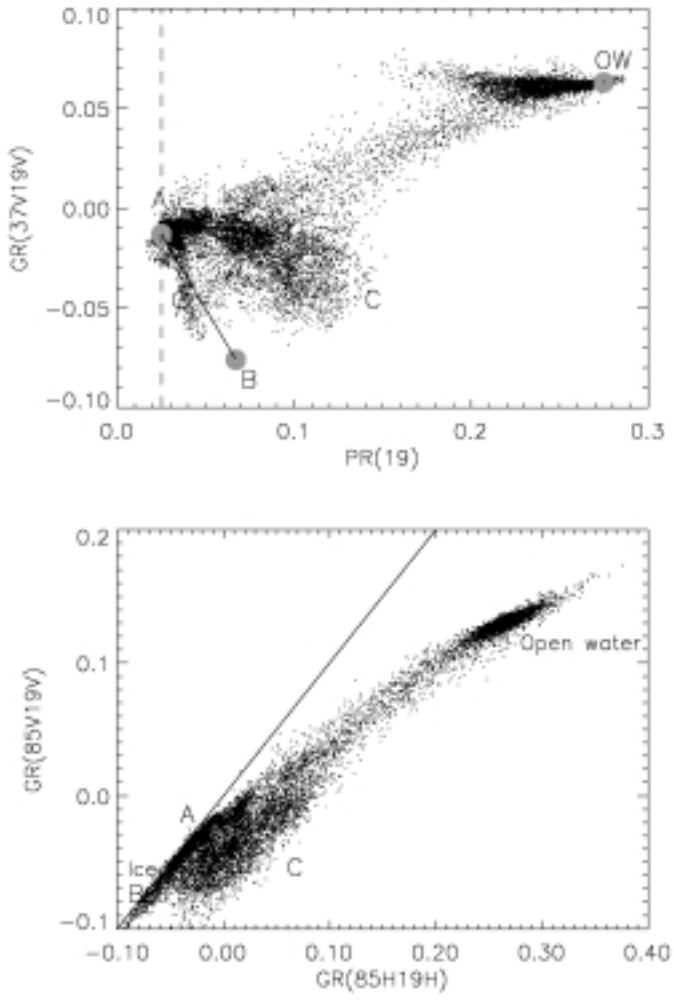

Figure 3. (a) Scatterplot of PR(19) versus GR(37V19V) in the Weddell Sea for September 15, 1992, The gray circles represent the tiepoints for the ice types A and B as well as for open water as used by the Nasa Team algorithm. Label C indicates pixels with significant surface effects. ϕ is the angle between the y-axis and the A-B line. (b) GR(85V19V) versus GR(85H19H) for the same data set as in (a). Ice types A and B cluster close to the diagonal. The amount of layering corresponds to the horizontal deviation from this line towards label C.

Next, we make use of GR(85V19V) and GR(85H19H) to resolve the ambiguity between pixels with true low ice concentration and pixels with significant surface effects. A plot of these two ratios is found to form narrow clusters except for areas where surface effects decrease TB(19H) and consequently increase GR(85H19H) (Figure 3b). Values of high GR(85V19V) and high GR(85H19H) are indicative of open water; the range of GR(85H19H) values is larger because of the greater dynamic range between ice and water for the horizontally polarized components. With increasing ice concentration, the two ratios have more similar values (Figure 3b). The narrow cluster of pixels adjacent to the diagonal shown in Figure 3b represents 100% ice concentration with different GR values corresponding to different ice types. When surface effects come into play, points deviate from this narrow cluster towards increased GR(85H19H) values (cloud of points to the right of the diagonal) while GR(85V19V) remains constant This cloud of points labeled C in Figure 3b also corresponds to the cluster of points labeled C in Figure 3a. Therefore the difference between these two variables, $\Delta GR = GR(85H19H) - GR(85V19V)$, will be used in the retrieval of ice concentration as an indicator of the presence of ice type C.

Finally, we need a third parameter to avoid the ambiguity between changes in ice concentration and changes in atmospheric conditions, because of the higher sensitivity of the 85 GHz channels to atmospheric variability compared to the lower frequency channels,. This third parameter is the rotated PR(85), $PR_R(85)$, computed from the PR(85)-GR(37V19V) domain analogous to the calculation of PR_R (19) (Table 3). In Figure 4, ΔGR is plotted against $PR_R(19)$ (top) and PR_R (85) (bottom) for the same region of the Weddell Sea as used for Figure 3. Two primary clusters can be identified in each plot. One cluster with high PR and ΔGR values is representative of open water with increasing weather resulting in lower PR_R values. The other cluster with low PR_R and ΔGR values are pixels with high ice concentrations. The cloud of points in the NASA Team PR-GR domain associated with surface effects (labeled C in Figure 3) has now become a linear cluster. Ice without surface effects has $PR_R(19)$ and ΔGR values close to zero. $PR_R(19)$ and ΔGR increase with increasing surface effects. In agreement with the results from Matzler et al. [1984], $PR_R(85)$ is nearly independent of surface effects resulting in an almost vertical cluster of points. Ice type C, which lies near the top end of the cluster and represents ice with a large amount of surface effects, is a radiometrically distinct ice type in this rotated domain. The scatter of points results partially from weather effects, partially from the natural variability in emissivity, and partially from real ice concentration changes.

3.1.1.2 Atmospheric conditions

In order to investigate quantitatively how different atmospheric conditions affect the retrievals, we calculated brightness temperatures for each SSMI channel using a forward atmospheric radiative transfer model [Kummerow, 1993] for each of the three ice types and open water. The model was run for different sea surface temperatures, atmospheric temperature and humidity profiles, and cloud conditions. The model considers absorption by water vapor and atmospheric oxygen as well as absorption and scattering by liquid and frozen hydrometeors.

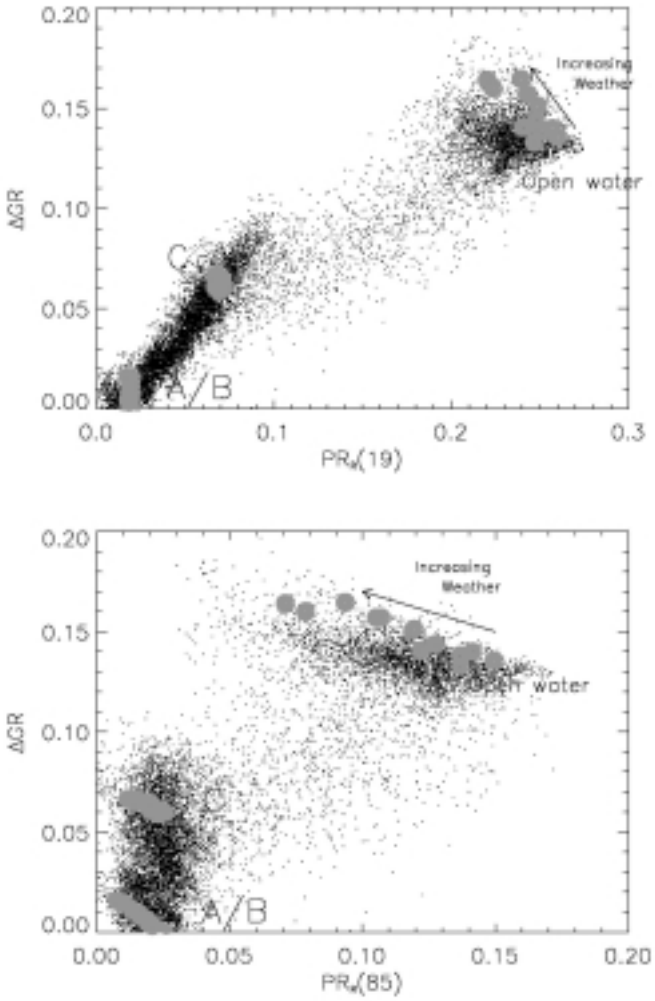

Figure 4. ΔGR versus $PR_R(19)$ (top) and ΔGR versus $PR_R(85)$ (bottom) for the same data set as in Figure 3. The gray circles represent the modeled ratios for the three pure surface types with different atmospheric conditions.

Model inputs are:

- Climatological winter and summer atmospheric temperature and humidity profiles from the Antarctic Georg-von-Neumayer station [Konig-Langlo, 1992].
- Surface emissivities from Eppler et al. [1992] adjusted to match the observed ratios under clear atmospheric conditions. (adjusted to match the tiepoints).
- Temperatures of the emitting surface:
  - Open water, summer: 274 K
  - Open water, winter: 271 K
  - Sea ice, summer: 268 K
  - Sea ice, winter: 248 K
- Different cloud types from cirrus to cumulus congestus taken from Fraser et al. [1975].

The various atmospheric conditions used are presented in Table 4.

The modeled $PR_R(19)$, $PR_R(85)$, and ΔGR values for different atmospheres over the three pure surface types are overlain in Figure 4 as gray circles. The figure shows that the model results in most cases span the width of the observed clusters. Clear atmosphere results have the lowest ΔGR and highest PR_R values for each surface type. As shown by Maslanik [1992] for the Arctic and Oelke [1997] for the Antarctic, weather effects on the NASA Team algorithm result in significant changes in ice type but not in total ice concentration for consolidated ice. This is reflected both in the vertical orientation of the gray circles and in the relatively tight ice cluster in the $PR_R(19)$- ΔGR plot. In contrast, the model results show a decrease in the $PR_R(85)$ plot with increasing weather explaining the broader ice cluster.

Using the radiative transfer model, we compute brightness temperatures for each SSMI channel and calculate $< PR_R(19)>$, $< PR_R(85)>$ and $<\Delta GR>$ which are matrices containing all combinations of ice concentration (0% to 100% in 1% increments) and atmospheric conditions used (Table 4). Both the ice concentration and the atmospheric contribution are found by locating the minimum of the quantity ΔR, defined by

$$\Delta R=(PR_Ri(19)-< PR_R(19)>)^2+(PR_Ri(85)-< PR_R(85)>)^2+(\Delta GRi -<\Delta GR>)^2 \qquad (5)$$

where $PR_Ri(19)$, $PR_Ri(85)$, and ΔGRi are the ratios calculated from the observed brightness temperatures for a pixel i; bracketed parameters indicate the modeled ratios. A schematic diagram summarizing key elements of the revised NASA Team sea ice algorithm is shown in Figure 5.

Table 4. Model atmospheres.

#	Season	Cloud Type	LWC [g m^{-2}]	Base Height [km]	Top height [km]
0	summer	clear	0.0	n/a	n/a
1	winter	clear	0.0	n/a	n/a
2	summer	cirrus	50.0	5.0	5.5
3	winter	cirrus	50.0	5.0	5.5
4	summer	stratus	15.0	0.4	0.7
5	winter	stratus	15.0	0.4	0.7
6	summer	stratus cumulus	75.0	0.5	1.0
7	winter	stratus cumulus	75.0	0.5	1.0
8	summer	stratus cumulus	125.0	0.5	1.0
9	winter	stratus cumulus	125.0	0.5	1.0
10	summer	cumulus congestus	250.0	1.0	3.0
11	winter	cumulus congestus	250.0	1.0	3.0

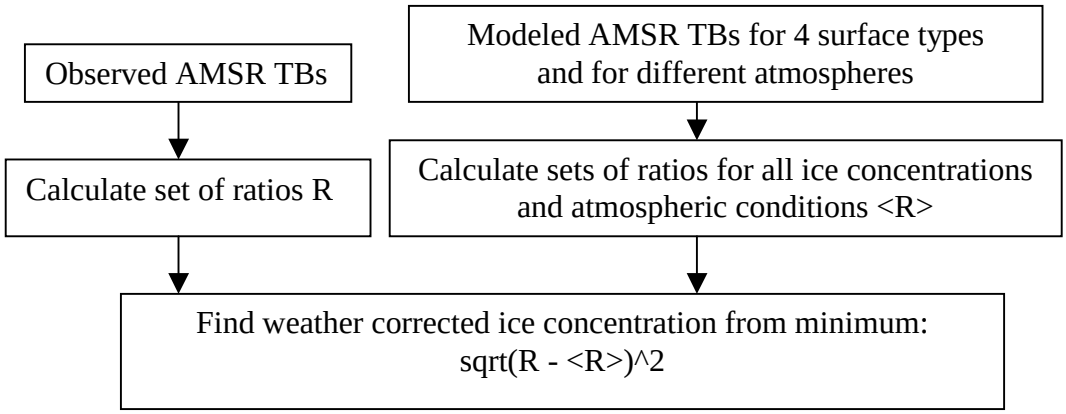

Figure 5. Revised NASA Team Sea Ice Algorithm

3.1.1.3 Thin ice conditions

The NASA Team algorithm is capable of distinguishing among three Arctic Ocean surface types: open water (OW), first-year (FY) ice, and multiyear (MY) ice. The problem of not being able to discriminate among new, young and first-year ice leads to a negative bias in the retrieved sea ice concentration (Cavalieri, 1994). To help understand how the algorithm misinterprets the presence of new and young sea ice, reference is made to the Arctic PR-GR distributions for April 4, 1988 shown in Figure 6. The distributions presented are for (a) ice-free and ice-covered oceans in the Northern Hemisphere; (b) the central Arctic region; and (c) only the Bering Sea, a seasonal sea ice zone. The algorithm triangle with labeled vertices and lines of constant ice concentration at intervals of 20% is superimposed on each of the three distributions.

In Figure 6a, the cluster of points representing ice-free ocean as well as weather related effects is located at the upper right vertex of the triangle labeled OW. The almost vertical cluster of points between the two other vertices corresponds to FY and MY ice types of high concentration. The cluster of points extending to the right of the FY ice vertex and having GR values close to zero is associated with new and young ice types. The horizontal spread of points in this cluster along a line nearly parallel to the PR direction depends on the age and thickness of the new ice. The position of this new and young ice cluster relative to the algorithm triangle (Figure 6a) explains why the algorithm underestimates ice concentrations in the presence of these ice types and why false indications of MY ice are often found in areas of new and young ice. At the right-hand end of this cluster (near the 40% iso-line of concentration), the algorithm interprets the corresponding PR and GR values as an ice cover of about 45% concentration and of mostly MY ice.

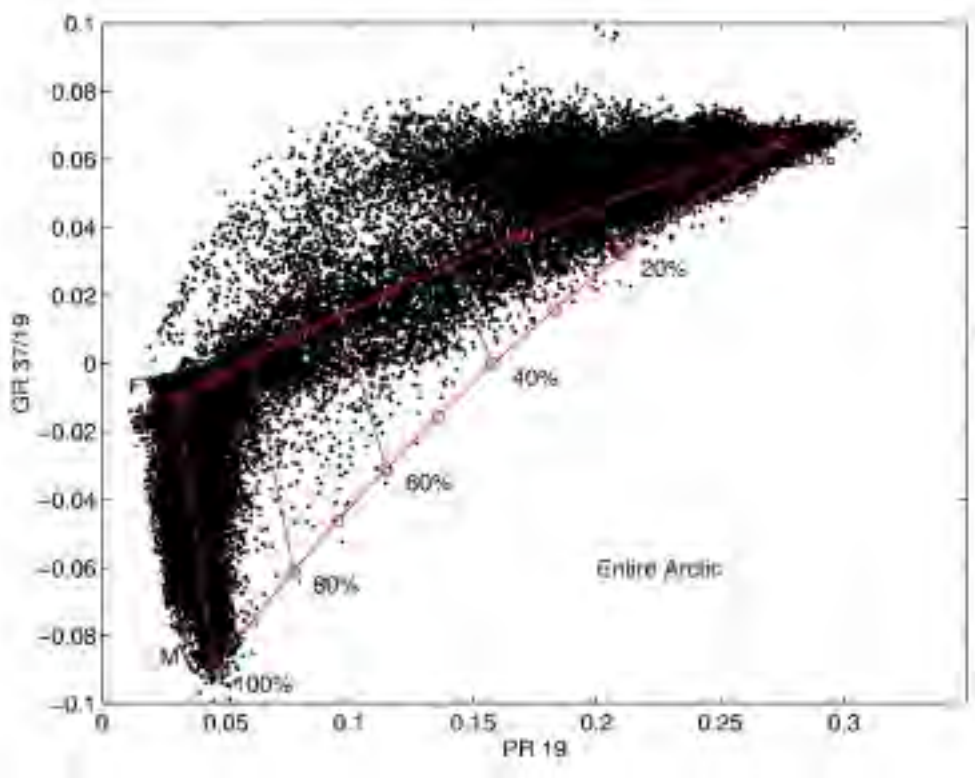

Figure 6a. PR-GR distribution for the entire Arctic on April 4, 1988 (after Cavalieri, 1994).

For the central Arctic (Figure 6b), the cluster is almost vertical and has a relatively small degree of scatter (approximately $\pm$10 percent) about the 100 percent ice concentration line. In contrast, the distribution for just the Bering Sea region (Figure 6c) consists of points clustered near the OW vertex and along the upper leg of the angle (OW to FY). Points with GR values close to zero form a nearly horizontal cluster which cuts into the algorithm triangle. The other seasonal sea-ice zones contribute to the remaining portion of the totality of points shown in Figure 6a. The distribution of points in Figure 6c is characteristic of seasonal sea-ice zones where there is little, if any, perennial ice and forms the basis of the algorithm following Cavalieri (1994).

The original thin ice algorithm described by Cavalieri (1994) is represented in (PR, GR) space by a triangle with vertices defined by open water (OW), first-year (FY), and new (N) ice points (Figure 7). The revised NASA Team algorithm is modified for the presence of thin ice as follows. First, the algorithm will use GR(37V/19V) instead of ΔGR and only two ice types will be used following Cavalieri (1994). Both PR19 and PR85 are still used as in the revised NASA Team algorithm described above. The retention of both PRs will allow an atmospherically corrected sea ice concentration to be retrieved. Most of the points in Figure 7 fall between the 80% and 100% ice-concentration contours, indicating that this algorithm may provide an improved estimate of total ice concentration in regions of new and young ice. Points falling below the lower leg of the triangle in Figure 7 have low GR values that may result from volume scattering by deep snow accumulated in areas of ridged ice or on shore-fast ice adjacent to the coasts. Sea ice concentrations of pixels

with GR values below –0.01 are calculated using the revised NASA Team algorithm described above. The rationale here is that ice with a heavy snow cover is not thin ice and the revised NASA Team algorithm is appropriate to use. For the present, the use of this revised thin ice algorithm will be limited to the Bering Sea and the Sea of Okhotsk, regions that have relatively large areas of thin ice.

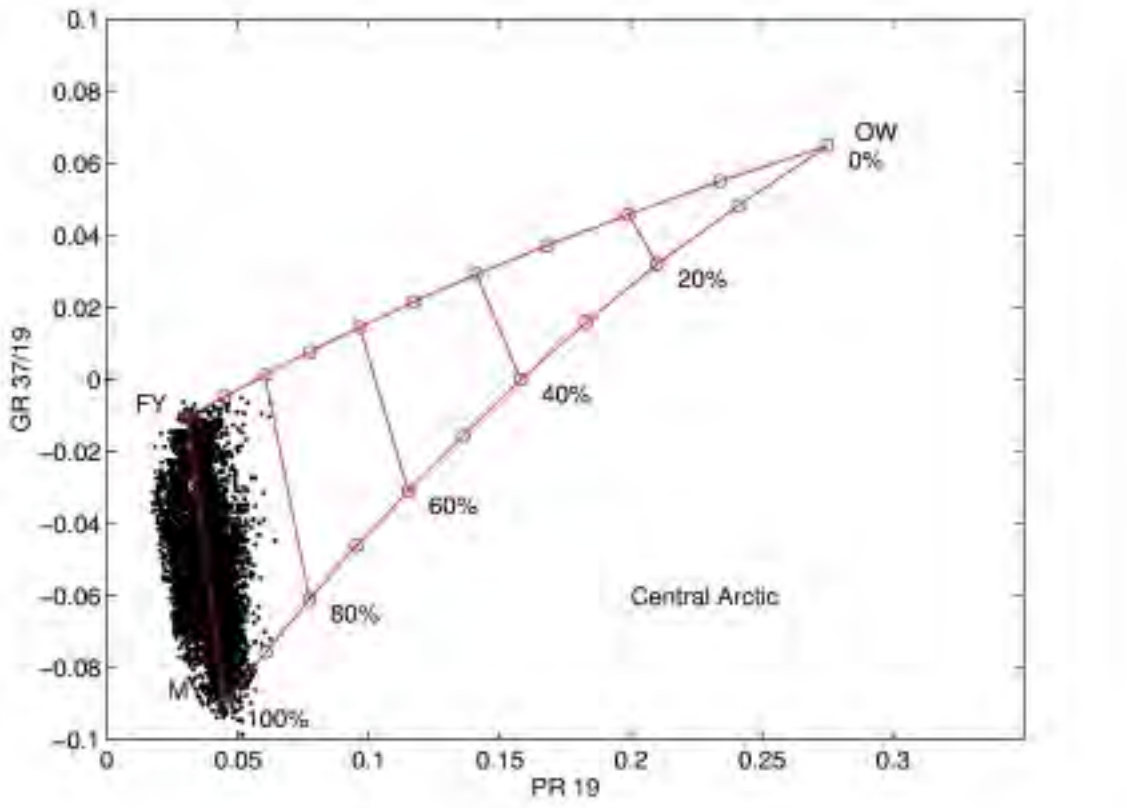

Figure 6b. PR-GR distribution for the central Arctic on April 4, 1988 (after Cavalieri, 1994).

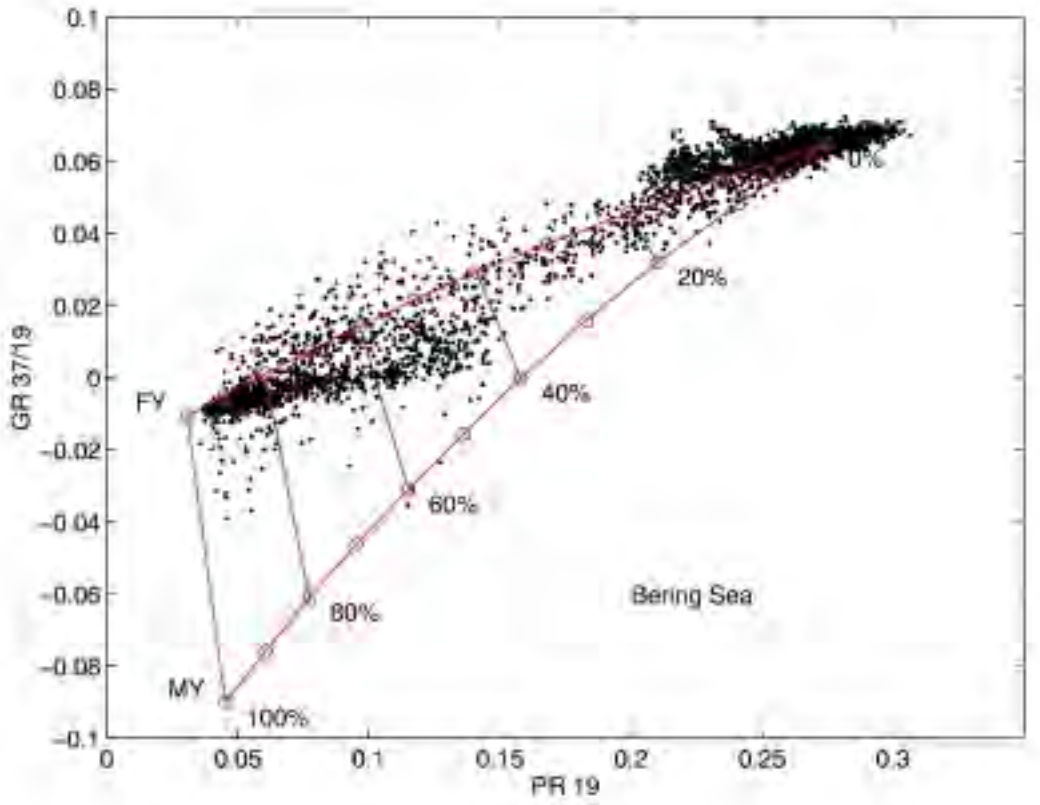

Figure 6c. PR-GR distribution for the Bering Sea only on April 4, 1988 (after Cavalieri, 1994).

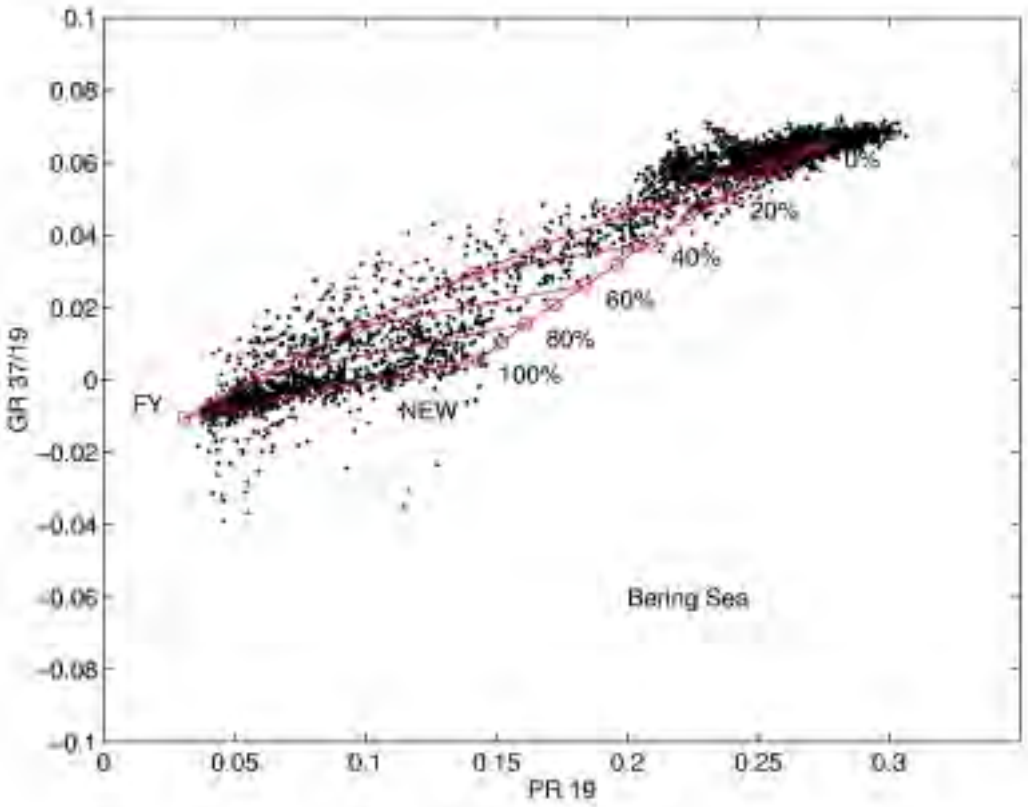

Figure 7. The thin ice algorithm is represented in (PR, GR) space by a triangle with vertices defined by open water (OW), first-year (FY), and new (NEW) ice points. The distribution of data points is for the Bering Sea on April 4, 1988 (after Cavalieri, 1994).

Four Bering Sea ice concentration maps derived using the NASA Team algorithm, the thin ice algorithm, the revised NASA Team algorithm, and the revised thin ice algorithm for April 4 is presented in Figure 8. Comparison of the four maps shows that the two thin ice algorithms yield substantially higher ice concentrations in the coastal polynya regions than do either of the other two NASA Team algorithms. Higher ice concentrations in these regions are consistent with a supervised principal component analysis of DMSP SSMI data which indicates open water concentrations of no more than 20-30% (Wensnahan et al., 1993) and by an ice-type classification of AVHRR imagery which shows that there is only a thin band of open water and new ice hugging the southern coasts of Alaska, Siberia, and St. Lawrence Island (see Plate 2c in Massom and Comiso, 1994). The sea ice concentrations in the southeast corner of the Bering Sea have not increased as much, suggesting that this is a low concentration area.

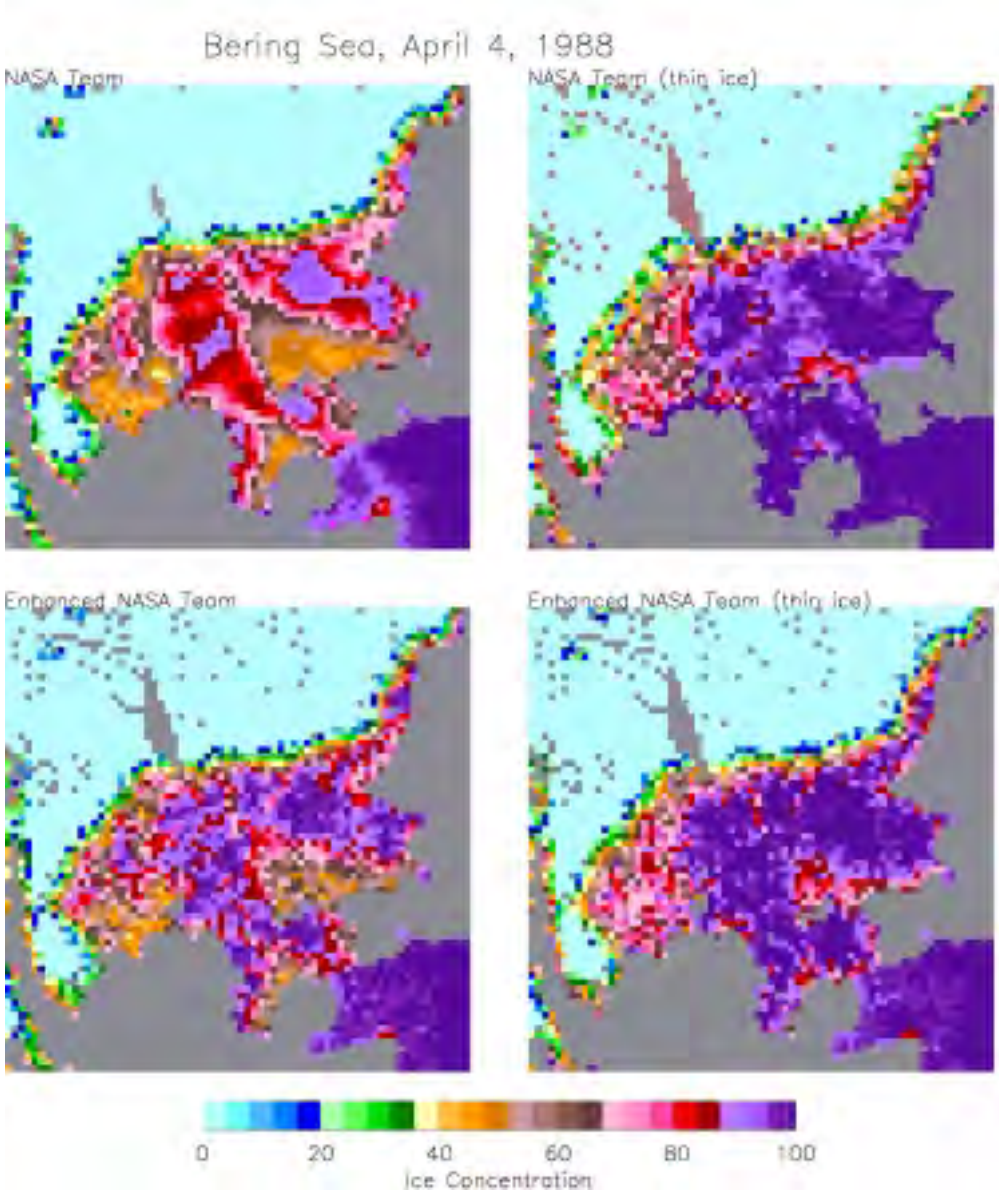

Figure 8. Bering Sea ice concentration maps for April 4, 1988 from (a) the NASA Team algorithm, (b) the NASA Team thin ice algorithm, (c) the enhanced NASA Team algorithm, and (d) enhanced NASA Team algorithm modified for thin ice.

3.1.1.4 Weather filter

Residual weather effects over ice-free ocean areas are apparent in some of the sea ice concentration retrievals with the enhanced NASA Team sea ice algorithm. Thus, to eliminate or at least greatly reduce these spurious sea ice concentrations over open ocean, the sea ice algorithm will employ a pair of weather filters as has been done for the SSMI (Cavalieri et al., 1995). The filters are based on threshold values for GR(37/19) and GR(22/19). Ice concentrations for image pixels with GR(37/19) values greater than 0.05 and GR(22/19) values greater than 0.045 are set to

zero. This technique was originally used with GR(37/18) for eliminating weather effects in sea ice concentration maps derived from SMMR data (Gloersen and Cavalieri, 1986), and the addition of the second filter (GR(22/19)) was needed for the SSMI sea ice concentration maps (Cavalieri et al., 1995).

3.1.1.5 Results and Comparisons

A comparison of Arctic sea ice concentrations using the original NASA Team algorithm and the enhanced NASA Team algorithm modified for the presence of thin ice in the Bering Sea and Sea of Okhotsk is presented in Figure 9. The Arctic sea ice concentrations are for January 27, 1997. Overall the retrievals look quite similar except in the seasonal sea ice zones such as the Bering Sea, and portions of the Sea of Okhotsk and the Greenland Sea. As noted previously, the low ice concentration bias observed in seasonal sea ice zones with the original NASA Team algorithm results from the presence of thin ice types (Cavalieri, 1994). The Arctic retrievals with the revised algorithm are next compared with a National Ice Center (NIC) ice chart for the Greenland Sea and AVHRR-derived sea ice concentrations for the Sea of Okhotsk.

The NIC ice chart of the Greenland Sea is presented in Figure 10 for comparison with the SSMI retrievals. As one can see from the chart legend, the ice concentrations are derived from visible/infrared and radar images giving an estimate not dependent on SSMI data. The two SSMI retrievals are shown in Figure 11. In general, the NASA Team and revised NASA Team algorithms give similar results, but there are significant local differences. For example, in the southern part of the Odden sea ice tongue, the ice concentrations are higher in the revised NASA Team results (70% to 80%) compared to the original NASA Team results. Overall, the enhanced NASA Team retrievals are in better agreement with the NIC ice chart than are the original NASA Team retrievals.

A cloud-free LAC AVHRR infrared image of the Sea of Okhotsk for February 4, 1995 (Figure 12) is used to compare sea ice concentrations derived from the NASA Team algorithm, the thin ice algorithm (Cavalieri, 1994), the revised NASA Team algorithm (Markus and Cavalieri, 2000), and the revised thin ice SSMI algorithm (Figure 13). A transect (black line in Figure 12), chosen to avoid cloudy areas, is used to compare AVHRR and SSMI sea ice concentrations. AVHRR concentrations were computed by first mapping the high resolution AVHRR data to a 1.5625 km SSMI grid. Because the regional air and surface temperature variability prohibits the calculation of AVHRR ice concentration using simple thresholds, the minimum AVHRR temperature for a 16 by 16 1.5625-km grid cell (equivalent 25 by 25 km) plus one standard deviation for consolidated ice (about 3 K) is taken to represent the 100% ice concentration temperature. The open water temperature is assumed to be 271.2 K. Ice concentrations are then calculated using a linear relationship between these two temperatures and the measured temperature.

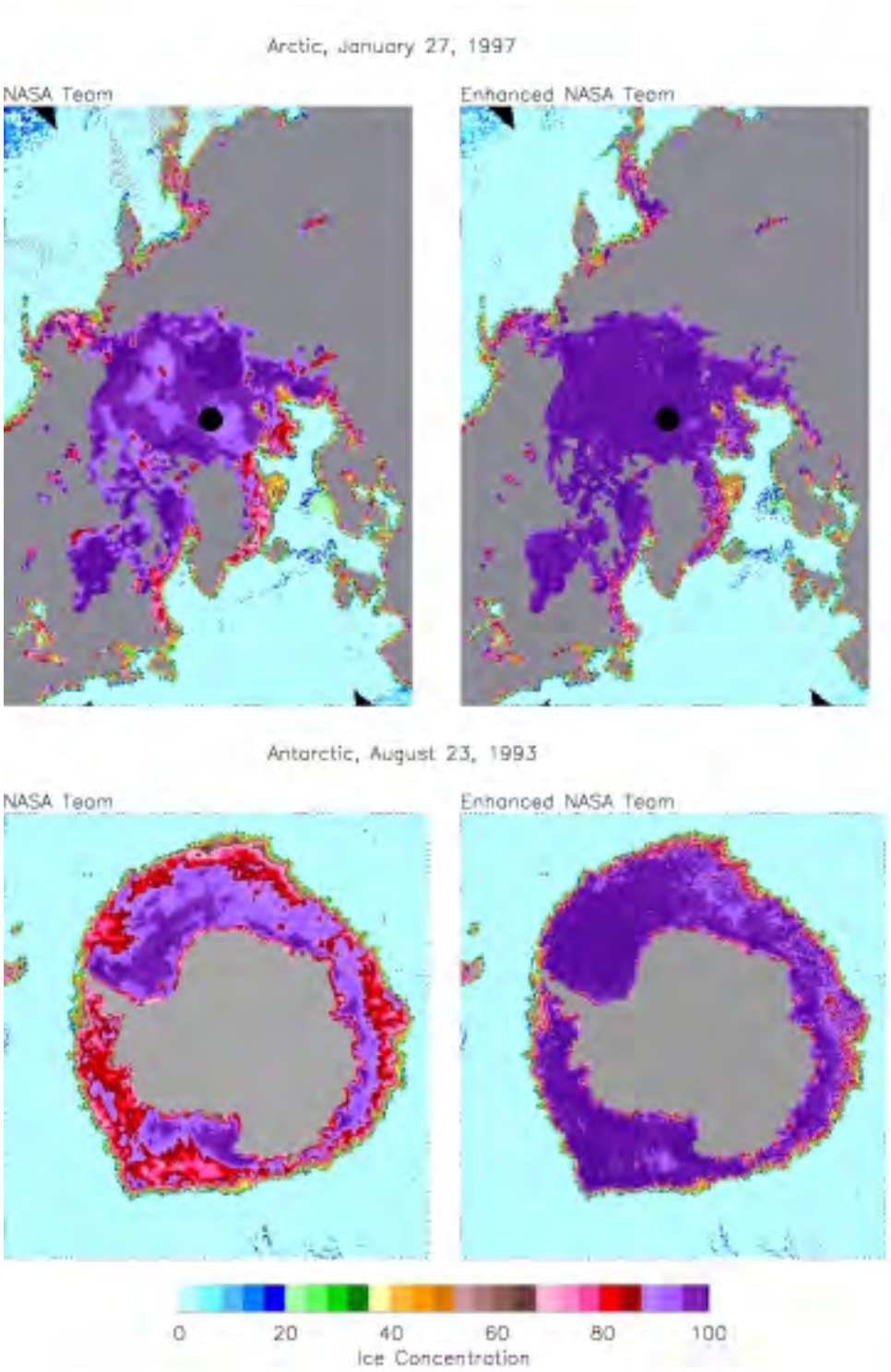

Figure 9. Comparison between Arctic sea ice retrievals using (a) the NASA Team algorithm and (b) the enhanced NASA Team algorithm and between Antarctic sea ice retrievals using (c) the NASA Team algorithm and (d) the enhanced NASA Team algorithm.

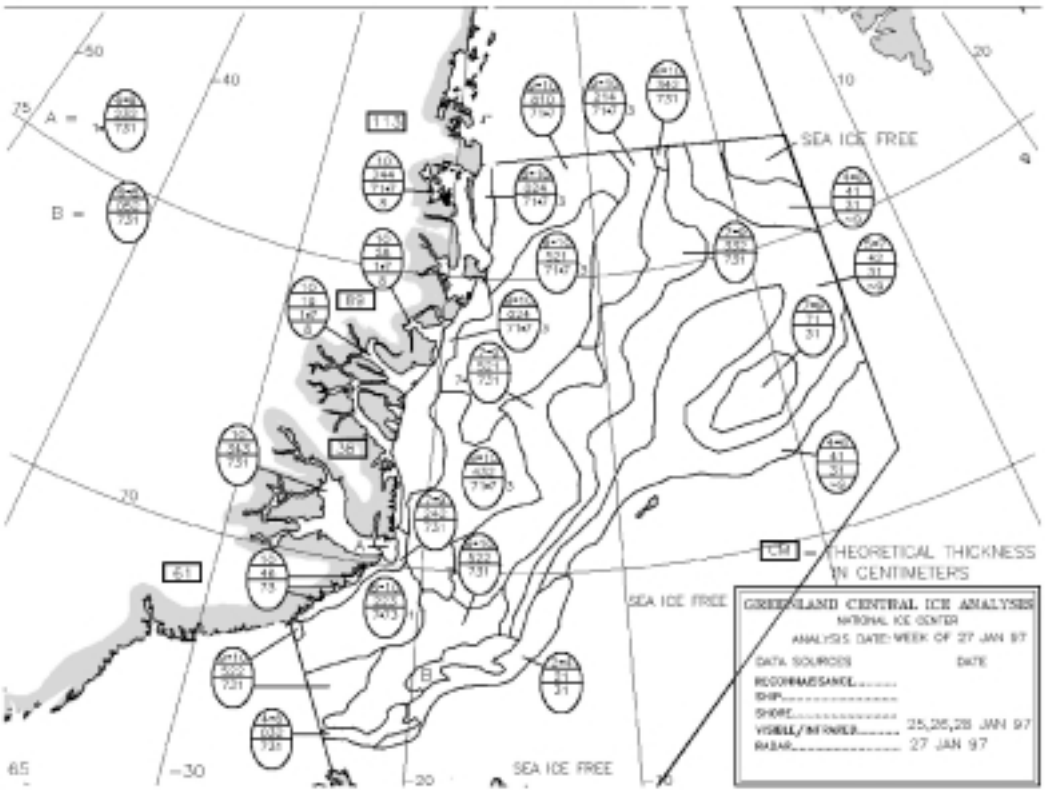

Figure 10. National Ice Center ice analysis of the Greenland Sea for the week of 27 January 1997.

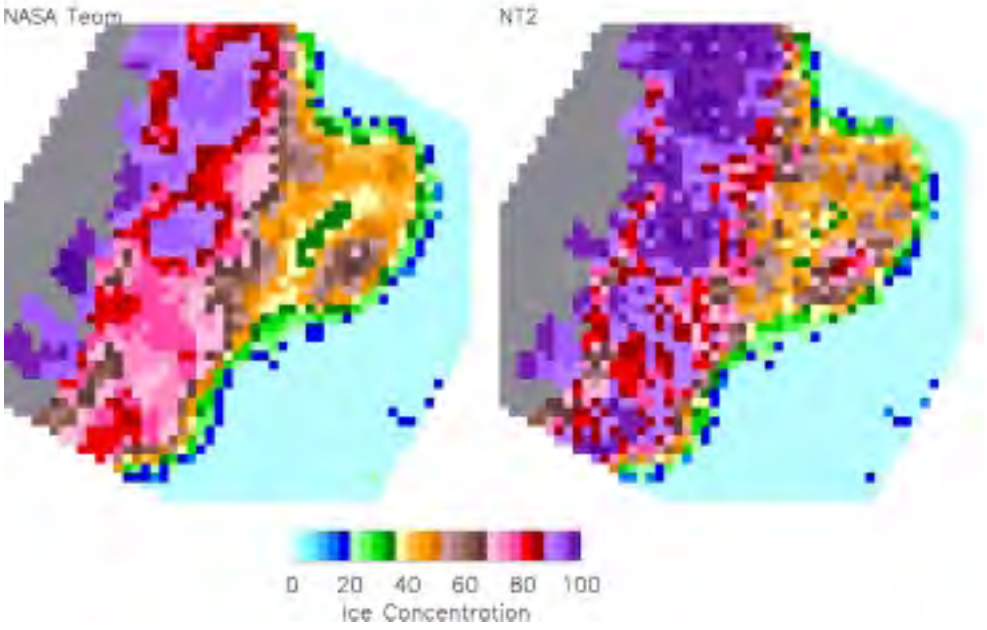

Figure 11. Sea ice concentrations for the Greenland Sea using the NASA Team and revised NASA Team (NT2) sea ice algorithms.

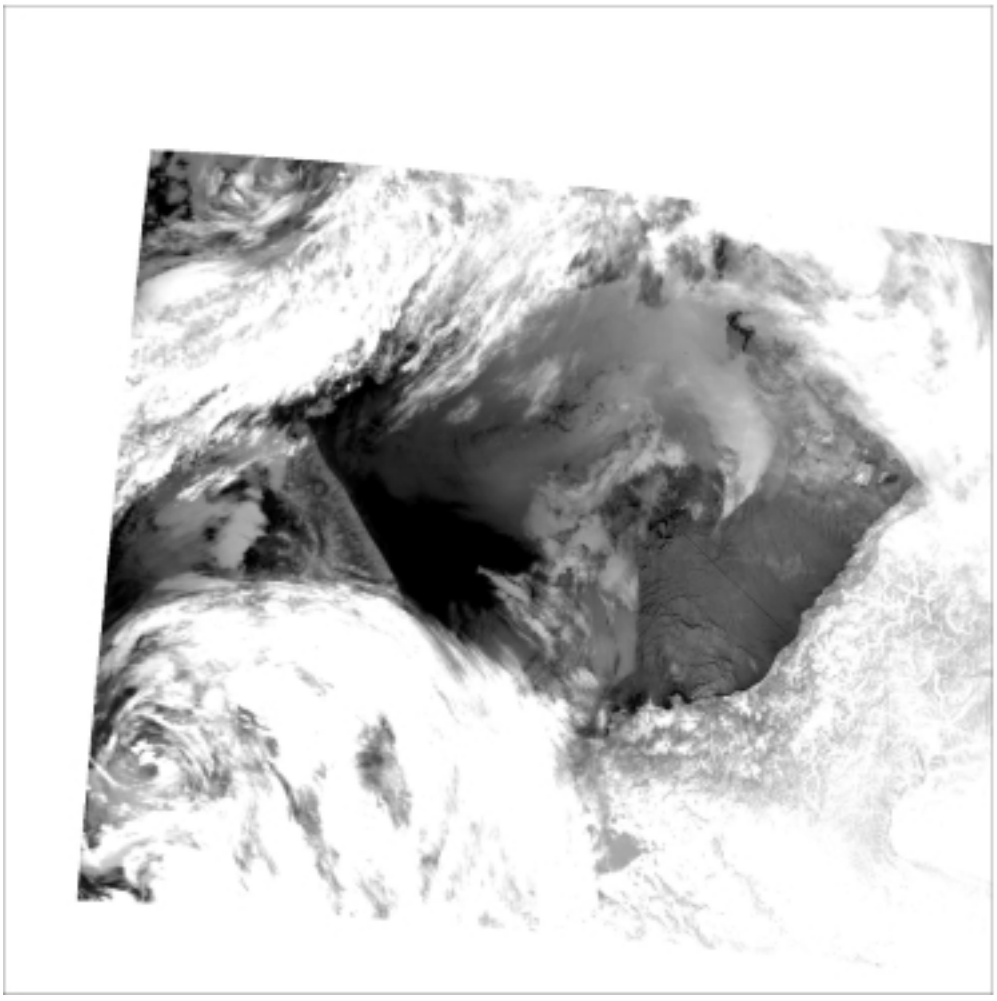

Figure 12. AVHRR image of the Sea of Okhotsk for February 4, 1995.

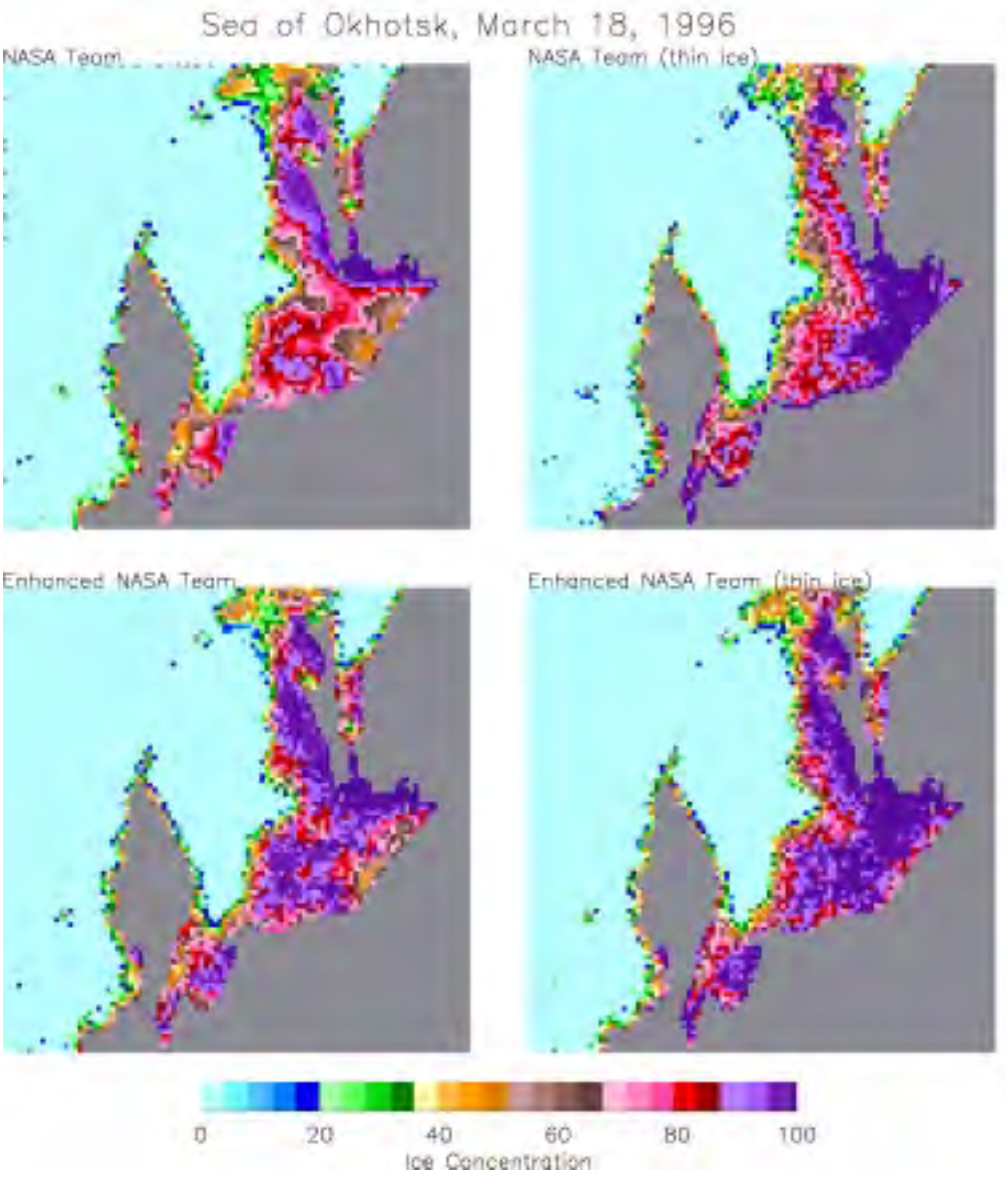

Figure 13. Sea of Okhotsk sea ice concentrations for March 18, 1996 derived using the NASA Team, the NASA Team thin ice, the enhanced NASA Team, and the enhanced NASA Team thin ice algorithms.

AVHRR and SSMI-derived sea ice concentrations for the Sea of Okhotsk are compared in Figure 14. All of the algorithms resolve the open water at pixel 7, but are in rather poor agreement with the AVHRR concentrations from pixel 10 on. While the reason for this is uncertain, we suspect that unresolved clouds in the image cause the AVHRR ice temperature peaks observed in Figure 14 and result in underestimates of ice concentration by the AVHRR algorithm. For example, the peak between pixels 170 and 180 in Figure 14a results in the AVHRR ice concentration drop at pixels 10 and 11 shown in Figure 14b. The ratios shown in Figure 14c reflect the general variation in sea ice concentrations observed by all the SSMI algorithms. The correlation coefficients and the mean differences relative to the AVHRR retrievals are given in Table 5. The correlation coefficients are equal for the NASA Team (thin) and the enhanced NASA Team (thin) algorithms, but the latter algorithm gives a smaller mean difference.

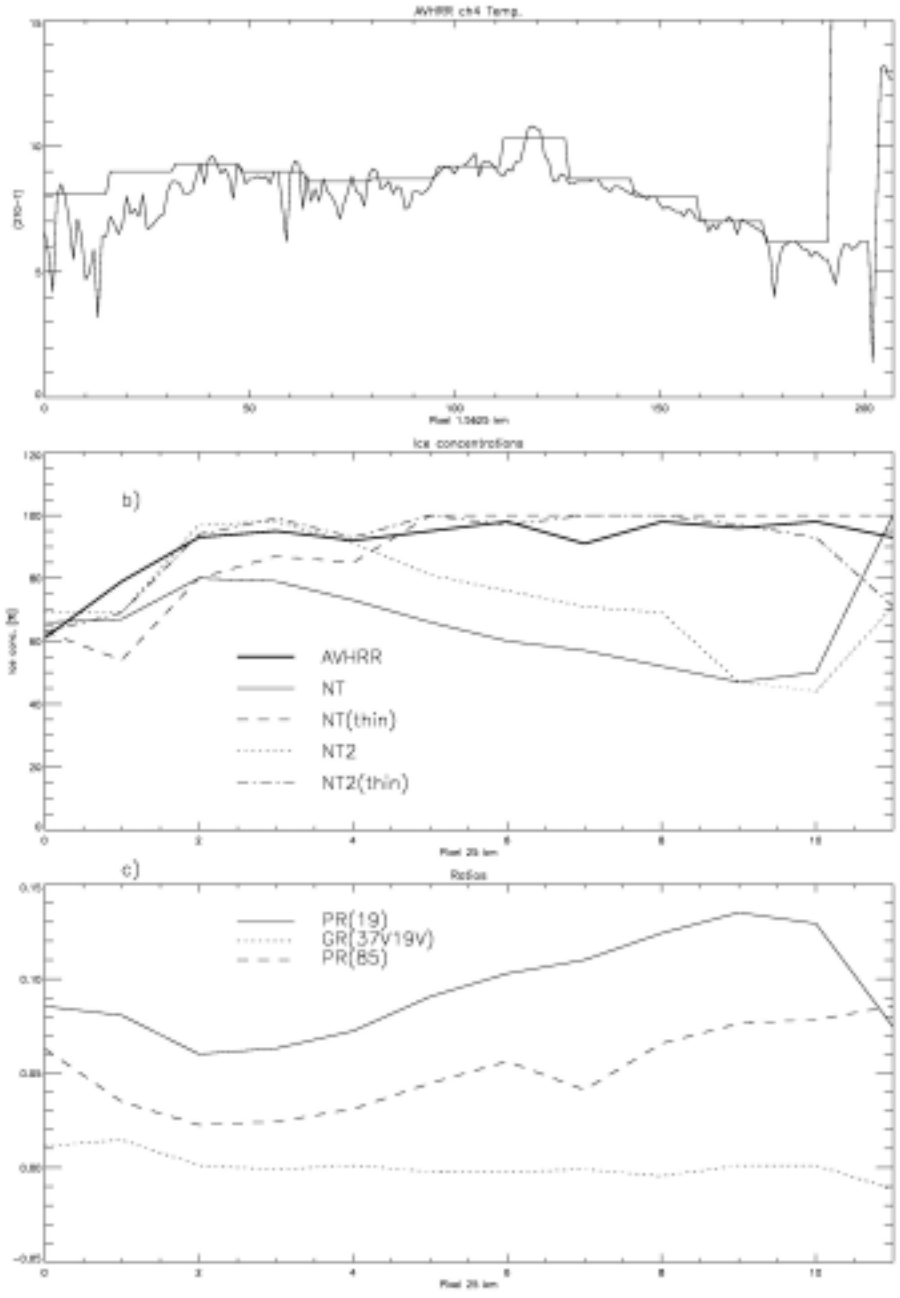

Figure 14. (a) AVHRR infrared data and reference 100% ice concentration temperatures derived from 16X16 pixel boxes; (b) ice concentrations derived from the SSM/I data using the NASA Team, the NASA Team thin ice, the enhanced NASA Team, and the enhanced NASA Team thin ice algorithms as well as the AVHRR concentrations; (c) brightness temperature ratios.

Table 5. Correlation coefficient and mean difference between the ice concentrations from AVHRR and each of the four SSMI algorithms for the Sea of Okhotsk as plotted in Figure 13.

Algorithm	Corr. Coeff.	Avg. (C_{AVHRR} - C_{SSMI})
NASA Team (NT)	-0.11	24.3%
NASA Team (thin)	0.80	1.7%
Enhanced NASA Team	0.01	17.2%
Enhanced NASA Team (thin)	0.80	1.1%

Examination of Figure 9 illustrates the difference between the original and enhanced NASA Team sea ice concentration retrievals for the Antarctic on August 23, 1993. Areas of low sea ice concentration in portions of the Weddell, Ross, and Bellingshausen seas observed in the original NASA Team retrievals result from surface layering effects as discussed previously in contrast to the enhanced NASA Team algorithm results. Comparisons with AVHRR-derived sea ice concentrations for the Ross Sea is discussed next to quantify these differences.

A mostly cloud-free AVHRR image of the Ross Sea for the same day shown in Figure 9 is presented in Figure 15. Except for a narrow coastal polynya along the Ross Ice Shelf and in Terra Nova Bay the sea ice is highly consolidated, although contains numerous leads. A blow-up of the Ross Sea (Figure 16) shows that the NASA Team algorithm seems to underestimate ice concentration in the outer pack whereas with the enhanced NASA Team algorithm this deficiency is not apparent. Analysis along a transect (black line in Figure 15) from the ice shelf towards the outer pack provides a more quantitative measure of the observed differences.

In Figure 17a, we plot the difference between 271.2 K and the AVHRR channel 4 temperatures. The horizontal line segments represent the derived ice temperatures corrsponding to a 100% ice concentration for each 16X16 pixel box. After the coastal polynya (pixel 60) adjacent to the shelf (pixels 0 to 30) the temperature decreases gradually until pixel 100. Leads can be identified as sharp drops in the temperature record. From about pixel 520 to pixel 550, some small polynyas have opened which are also recognizable in the AVHRR image (Figure 15). The 25 km ice concentrations (Figure 17b) capture the coastal polynya but only the enhanced NASA Team algorithm shows a rapid increase in ice concentration in agreement with the AVHRR concentrations. In general, the enhanced NASA Team retrievals provide a better match with the AVHRR concentrations. This good agreement is also reflected in the correlation coefficient of 0.83 compared to 0.65 for theNASA Team algorithm (Table 6). The small average difference of -0.8% (Table 6) shows that the bias is almost insignificant. The better performance of the enhanced NASA Team algorithm compared to the original NASA Team can be explained with the help of the PR(19), GR(37V19V), and PR(85) values (Figure 17c). Only at PR(85) do the two polynya areas result in distinct peaks. From pixel 5 to pixel 20, PR(19) is fairly constant, whereas GR(37V19V) decreases from 0.0 to -0.03. This decrease in GR(37V19V) indicates a probable increase in snow cover resulting in the warming of the snow-ice interface. At pixel 20 the NASATeam ice concentrations begin to decrease as a result of an increase in PR(19). Because GR(37V19V) stays at values well below zero, this increase in PR(19) is probably caused by snow cover effects. This increase is not seen in PR(85).

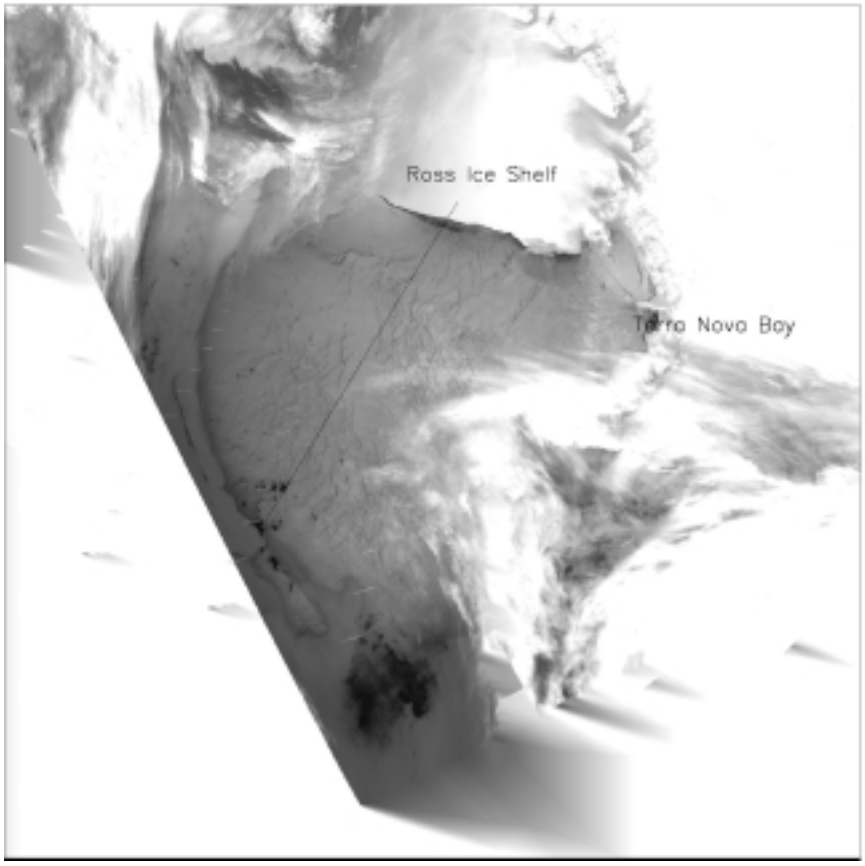

Figure 15. AVHRR image of the Ross Sea for August 23, 1993. Sea ice concentrations were calculated along the transect shown in black.

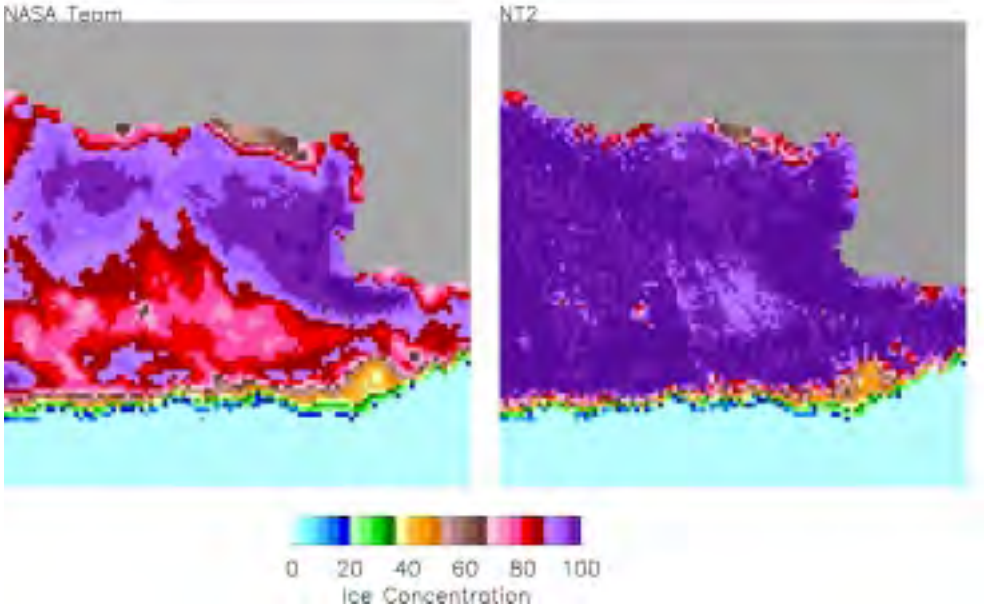

Figure 16. Sea ice concentrations for the Ross Sea using the NASA Team and revised NASA Team (NT2) sea ice algorithms.

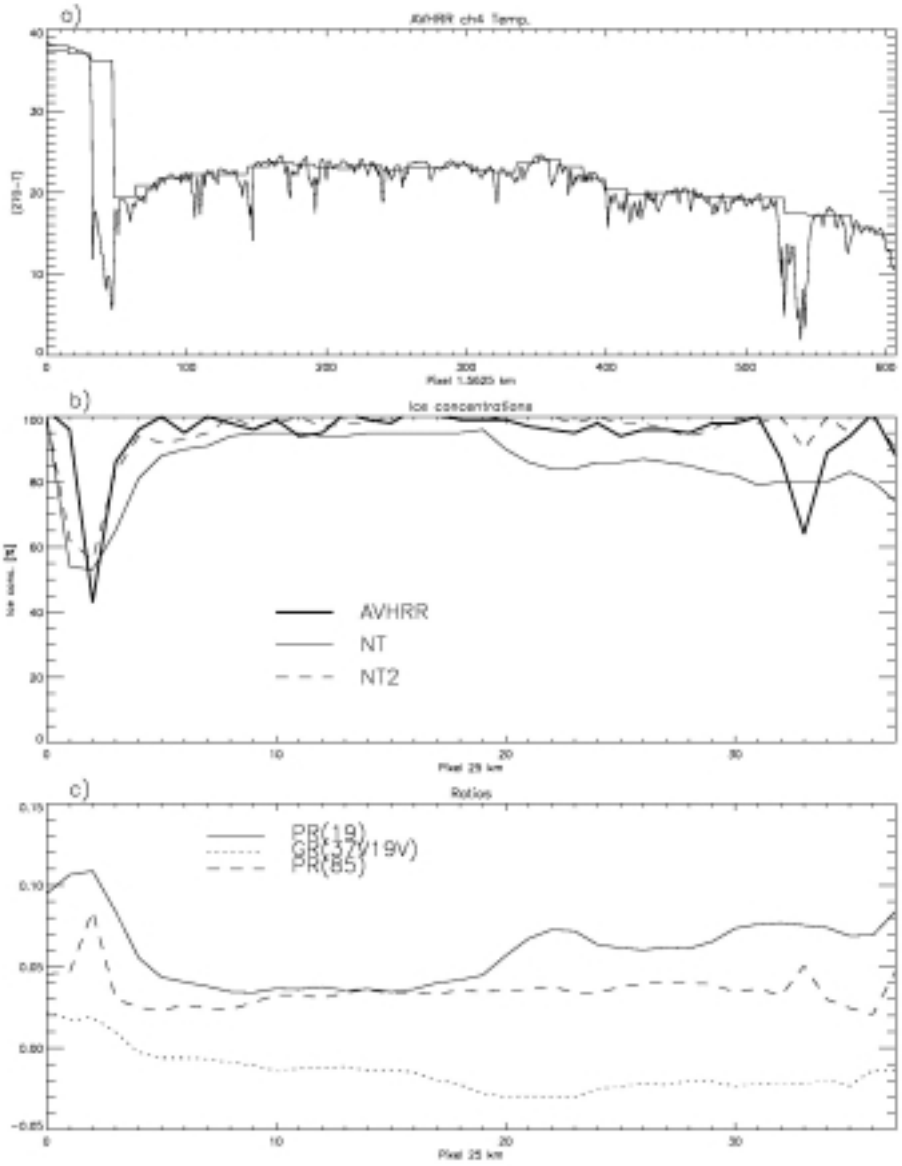

Figure 17. For the Ross Sea transect shown in Figure 15: (a) AVHRR infrared data and reference 100% ice concentration temperatures derived from 16X16 pixel boxes; (b) ice concentrations derived from the SSM/I data using the NASA Team and the revised NASA Team algorithms as well as the AVHRR concentrations; (c) brightness temperature ratios.

Table 6. Correlation coefficient and mean difference between the ice concentrations from AVHRR and NASA Team algorithms for the Ross Sea.

Algorithm	Corr. Coeff.	Avg. (C_{AVHRR} - C_{SSMI})
NASA Team (NT)	0.65	7.9%
Enhanced NASA Team	0.83	-0.8%

3.1.1.6 Uncertainty estimates

Estimates of uncertainties for the revised NASA Team algorithm are based on previous sensitivity and validation studies using SSMI data. The estimates of accuracy will be updated after our AMSR-E validation plan has been implemented following the launch of EOS Aqua.

First, with regard to sea ice temperature sensitivity, both the NASA Team and revised NASA Team algorithms are to first order independent of spatial and temporal variations in ice temperature because of the use of ratios of brightness temperatures, PR and GR. The potential sensitivity of GR to ice temperature variations has been discussed elsewhere and is not expected to be a problem (Gloersen et al., 1992; Comiso et al., 1997).

Second, in order to investigate how sensor noise affects the ice concentration retrievals the brightness temperatures for each SSMI channel was varied by $\pm$1K, the upper limit of sensor noise [Hollinger et al., 1987]. This was done for three sets of brightness temperatures corresponding to ice concentrations of 32%, 51%, and 98% in order to represent the range of ice conditions. The results are presented in Table 7 and are approximately the same order of magnitude as for the NASA Team algorithm [Swift and Cavalieri, 1985]. These noise sensitivity coefficients may also be used to estimate the effect of surface emissivity variations on the algorithm retrievals.

Table 7. Calculated ice concentrations resulting from changes of $\pm$1K in brightness temperature for each channel. The bottom row is the RMS change for all channels.

	C=32%		C=51%		C=98%	
ΔK	+1 K	-1 K	+1 K	-1 K	+1 K	-1 K
19V	34	31	52	49	99	95
19H	32	32	51	51	98	98
37V	31	33	50	52	95	99
85V	30	34	49	53	94	100
85H	34	30	45	48	100	94
$\sqrt{\Sigma i \Delta Ci}$	3.6	3.2	6.5	4.2	5.3	5.5

Next, to understand how the limited set of atmospheres used in the algorithm may affect the retrievals, three pixels with ice concentrations of 32%, 51%, and 98% analogous to the study of sensor noise were examined. The variable ΔR from equation 5 provides a measure of the difference between the measured set of ratios and the modeled ratios for each ice concentration combination and atmosphere. The values of ΔR are sorted by increasing difference. These, together with the corresponding ice concentrations are plotted in Figure 18. The top plot in this Figure shows that ΔR reaches a distinct minimum and that the ice concentrations converge to an ice concentration of about 50% (bottom plot). In Figure 19, the smallest one hundred ΔR values together with the corresponding ice concentrations and atmospheric indices for the 32%, 51%, and 98% cases are presented. For the 32% and 51% cases ΔR is almost zero for the best solution meaning that there

exists a set of modeled ratios which matches the measured ratios almost perfectly. For the 98% case the best ΔR is somewhat higher. For the 15 smallest differences, the ice concentrations vary only by ±2% for the 32% and 98% cases and by ±1% for the 51% case. Although the total ice concentrations are very stable for the last 15 solutions, oscillation in the atmospheric indices (Table 4) continues. For example, in the 32% case, oscillations occur between the atmospheric index 2 and 7, which represent a summer atmosphere with cirrus clouds (high water vapor, low cloud liquid water) and a winter atmosphere with more liquid water and less water vapor. Similar phenomena can be seen for the 51% and 98% cases. Other cases have been found where the atmosphere index oscillates between two odd or even values which correspond to the same season. This suggests that for those cases the ``true" atmosphere has probably a liquid water content between the two modeled atmospheres. Because all of the SSMI channels (except for the 22 GHz channel) lie in atmospheric ``window" frequencies, the atmospheric contribution is generally rather small (even at 85 GHz). Therefore, we cannot retrieve atmospheric parameters over the highly emissive sea ice but we can reduce the ``atmospheric noise" in the received radiances.

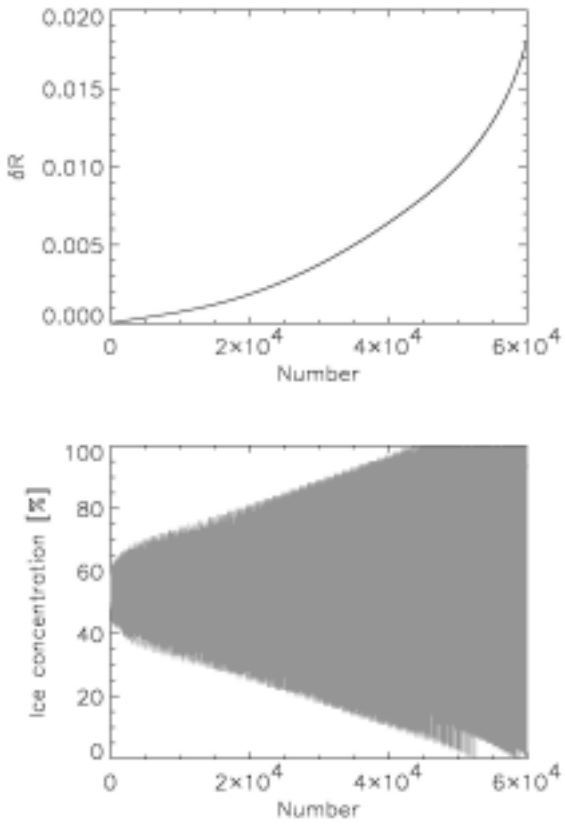

Figure 18. (a) All of the possible 60000 ΔR values (sorted by increasing ΔR value) and (b) the corresponding ice concentrations for a retrieved ice concentration of 51%.

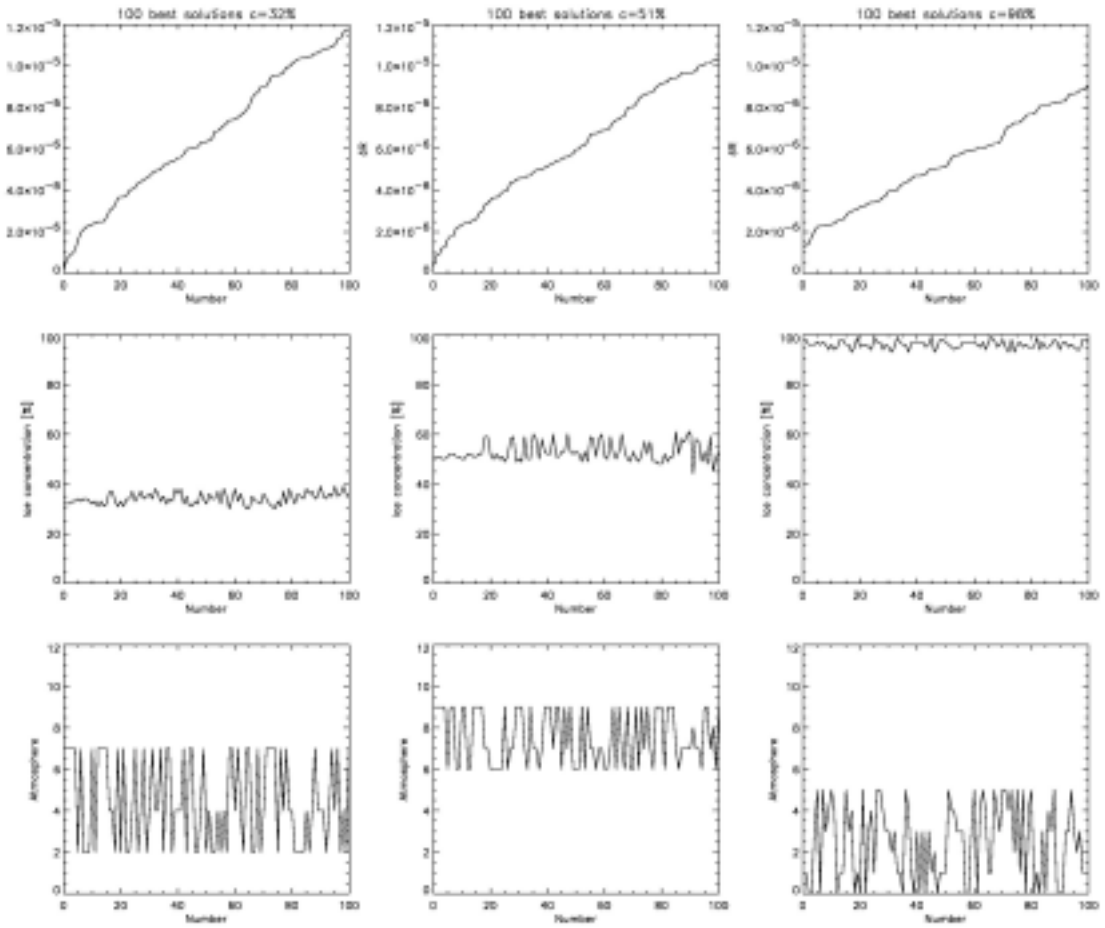

Figure 19. Smallest 100 ΔRs with corresponding ice concentrations and atmospheric indices for the 32% case (left column), the 51% case (middle column), and the 98% case (right column).

In Table 8, the ice concentrations with the smallest ΔR value for each atmosphere index (see Table 4) are listed separately. For the 32% case, the smallest ΔR corresponds to an atmosphere index of 7 followed by indices 2 and 4, which all have similar ice concentrations. The ΔR value is about an order of magnitude smaller for index 7 compared to indices 2 and 4. The range in ice concentration is approximately $\pm$10% indicating the error range without atmospheric correction. The 51% case has about the same range. Here, ΔR is high for small atmosphere indices and has a distinct minimum at index 9 followed by index 6, both of which give identical ice concentrations. The range in ice concentrations is smaller for the 98% case ($\pm$5%) with smallest ΔR values for atmosphere with little liquid water content. Based on these analyses we conclude that the atmospheric correction is necessary and that the retrieved ice concentration is stable.

The discussion of the revised NASA Team algorithm and in particular the comparison with other data sets suggest that the revised algorithm will do better than the original NASA Team algorithm. As such, results from the NASA SSMI Sea Ice Validation Program are relevant. The validation program was initiated in 1987 and completed in 1991. Results from the program have been published in a final report (Cavalieri et al., 1992) and in three journal publications (Cavalieri,

1991; Cavalieri et al., 1991; Steffen and Schweiger, 1991). Validation of the SSMI sea ice products centered on comparative analyses of multisensor satellite and aircraft data sets including Landsat MSS and NOAA AVHRR; aircraft sensors included C-, L-, and P-band SAR, a Ka-band scanning radiometer, a fixed-beam multichannel radiometer, and aerial cameras. The results from the Landsat comparisons, which covered all seasons and both hemispheres, showed that, on average, the difference between the NASA Team algorithm using SSMI data and the Landsat derived ice concentrations was -3.6%$\pm$ 6.6% for winter months, whereas for early spring in the Amundsen Sea the result was 1.3%$\pm$3.6%. We anticipate that with the enhanced algorithm the retrievals will be improved as the comparisons of section 3.1.1.5 suggest, but many more comparisons are needed and will be provided by the validation program described in section 5.0.

Table 8. Ice concentrations with the smallest ΔR for each atmosphere separately for the 32%, 51%, and 98% cases.

	C=32		C=51%		C=98%	
Atm. Idx	IC	ΔR	IC	ΔR	IC	ΔR
0	40	2.5E-5	61	7.0E-5	96	1.4E-6
1	44	1.2E-4	64	1.7E-4	98	1.3E-6
2	34	1.6E-6	58	1.2E-5	93	3.9E-6
3	39	6.6E-5	61	1.2E-4	96	2.0E-6
4	37	3.0E-6	60	1.5E-5	94	2.3E-6
6	29	6.1E-5	51	1.6E-6	94	5.5E-5
7	32	1.8E-7	59	3.3E-6	94	1.5E-5
8	28	4.1E-4	44	9.7E-6	94	1.6E-4
9	29	8.4E-5	51	3.2E-7	94	7.8E-5
10	23	1.4E-3	40	3.1E-4	94	4.1E-4
11	23	8.9E-4	41	1.3E-4	94	3.0E-4

3.1.2 AMSR Bootstrap Algorithm

3.1.2.1 Background and Theoretical Basis

The algorithm described in this section, which will be referred to the AMSR Bootstrap Algorithm (ABA), is the same algorithm that was proposed in the original AMSR ATBD. This algorithm has already been endorsed by previous reviewers and the latter's concerns have been addressed in a previous revision of the original ATBD. The Bootstrap algorithm has also been chosen by NASDA to be used for generating standard sea ice concentration products for both hemispheres to be archived in the Japanese Earth Observation Center (EOS). In this section, the pre-launch version of the algorithm will be presented including the enhancements made since the last review. The enhancements further improve the performance and accuracy of this algorithm without changing the physics of the technique. Since a true simulated AMSR data set with all the channels present does not currently exist, the algorithm as presented in this ATBD will need further tuning and refinement before it can be used in its final form. The algorithm has been tested using SMMR data which have the basic channels required. However, the latter is known to have

problems with calibration and resolution, especially with the 6 GHz channels, and with AMSR, it is expected that the derived products will be of much higher quality.

Passive microwave data have been specially useful for sea ice studies because of the relatively high contrast in the emissivities of open water and sea ice (Zwally et al., 1983). The contrast is frequency dependent and is much higher with the lower frequencies than with the higher frequencies. Thus, if resolution is not an issue, the 6.9 GHz data from AMSR would be best suited for ice retrievals since it provides the best contrast between ice and open water. This frequency is also less vulnerable to atmospheric and surface effects than the other channels and provides ice temperatures which are utilized by the algorithm to correct for residual temperature effects. The use of the 10.7 GHz data is also promising because of its better resolution than the 6.9 GHz data and its utility at further improving the accuracy of the ice concentration retrievals will be explored.

The choice of the set of channels for the algorithm is very important. Although low frequency channels are desirable because of the high contrast in the emissivity of ice and water and the low sensitivity to the atmosphere and surface scattering in these channels, the basic set of channels used for the Bootstrap algorithm are the 18.7 GHz and the 36.5 GHz channels. The reason for using this set is that it satisfies better the resolution requirement without much sacrifice on the accuracy. It also produces ice concentration products that are consistent with historical data that have been derived since 1978, starting with SMMR. This is not a minor consideration since climate change studies require long term data sets. A 6.9 GHz channel is used for correcting for temperature effects but on the average, the spatial change in temperature distribution is slow and it's use does not impose a resolution constraint on the product derived with the use of the 18.7 GHz and 36.5 GHz channels, as will be discussed later. The 89 GHz channels are not chosen because of practically no contrast between ice and water at this frequency and because of large sensitivity to atmospheric and surface effects.

Assuming a linear relationship between the brightness temperature and the fraction of ice cover as in equation (1), the ice concentration, C_I, corresponding to an observed brightness temperature, T_B, over a sea ice covered region can be derived from the mixing formulation with all ice types combined and is given by:

$$C_I = (T_B - T_O)/(T_I - T_O) \qquad (6)$$

where T_O and T_I are reference brightness temperatures of open water and sea ice, respectively. T_O, T_I , and T_B all include contributions from the intervening atmosphere, as described in Zwally et al. (1983). T_I varies spatially mainly because of spatial changes in the emissivity and temperature of the ice, while T_O is approximately constant for open water surfaces within the ice pack. Thus, the success of an ice concentration algorithm depends on how accurately the value of T_I is determined. The use of equation (6) without correcting for atmospheric effects is justified because over the ice pack, the atmosphere is relatively stable spatially for the set of frequency channels that are used in this algorithm as will be shown later. At the frequencies utilized, any advantage provided by an atmospheric correction through a radiative transfer model is usually negated by errors in the model due to inadequate atmospheric data on a pixel by pixel basis.

As indicated in Comiso et al. (1992), 100% new ice is will have on the average an ice concentration of about 85%. The reason for this is the generally lower emissivity of new ice which varies considerably with time being similar to that of open water during early formation stages, increasing to an intermediate value when it solidifies and forms either nilas or pancake ice, and finally reach its highest value that matches the tie points which it becomes young or first year ice. Beyond young ice, the emissivity still changes but such changes are accounted for through the use of the multichannel technique used by the algorithm. Unambiguous determination of the true open water area in thin ice regions is thus almost impossible and an accurate ice type classification is difficult even between first year ice and multiyear ice because of overlapping emissivities.

This brings in the question of scientific utilization of the data. The ice concentration data, in general, are meant to provide useful information for polar process and climate change studies, as part of the Earth Science Enterprise program. This requires ability to identify areas of polynyas and leads which are regions of high ice production, high heat and salinity fluxes, and low albedo. Failure to identify these features in an ice concentration map may render the data basically useless since the true area of open water within the ice pack has been estimated as about 1 to 2 % in winter (S. Ackley, private communication, 1992) which would make it difficult to identify the ice features. The size of polynyas and leads are usually larger than the true open water areas since within hours, a large fraction of these features gets covered by frazil or grease ice. The heat fluxes from these new ice types are also known to be about an order of magnitude higher than those from the thicker ice types (Maykut, 1978) and identification of the true size of the feature is important to accurately assess the net effect of the feature. The same ABA algorithm may be modified to allow for higher average ice concentration in primarily new ice areas through the introduction of higher frequency channels (i.e., both polarizations at 36.5 GHz or 89 GHz channels), which have lesser penetration depths through the ice, but the requirement must be driven by scientific needs.

3.1.2.2 Technique

In the original Bootstrap Algorithm (Comiso, 1995), T_I and T_O in equation (6) are determined with the aid of two sets of channels: (a) 19 GHz and 37 GHz brightness temperatures, both vertically polarized (called V1937); and (b) vertically and horizontally polarized 37 GHz brightness temperatures (called HV37). Scatter plots in the HV37 and V1937 two-dimentional spaces using P3a aircraft radiometer data flown over 100% or near 100% ice in the Arctic are shown in Figure 20a and 20b, respectively. In both plots, the data points are mostly along the line AD and are very similar in compactness to those of satellite data (Comiso, 1986). The linearity of these data points is the key information that is utilized by the Bootstrap Algorithm to identify the proper value of T_I, as indicated in equation (6). In the scatter plot shown in Figure 20a, data points of open water within the pack would fall near the location labeled O. Thus, for any given observation corresponding to the data point B in this 2-D space, T_I is inferred using the intercept of the lines AD and OB and ice concentration is determined from equation (6), or an equivalent formulation as described in Comiso (1995). The basic characteristics of the consolidated ice cluster shown in Figure 20 are consistent with satellite observations, with ship radiometer data over the Antarctic, and with portable radiometer data over artificial sea ice at CRREL. The compactness of the data points in the satellite scatter plot data is an indication that atmospheric effects, which are part of the observed data, do not contribute much to the error.

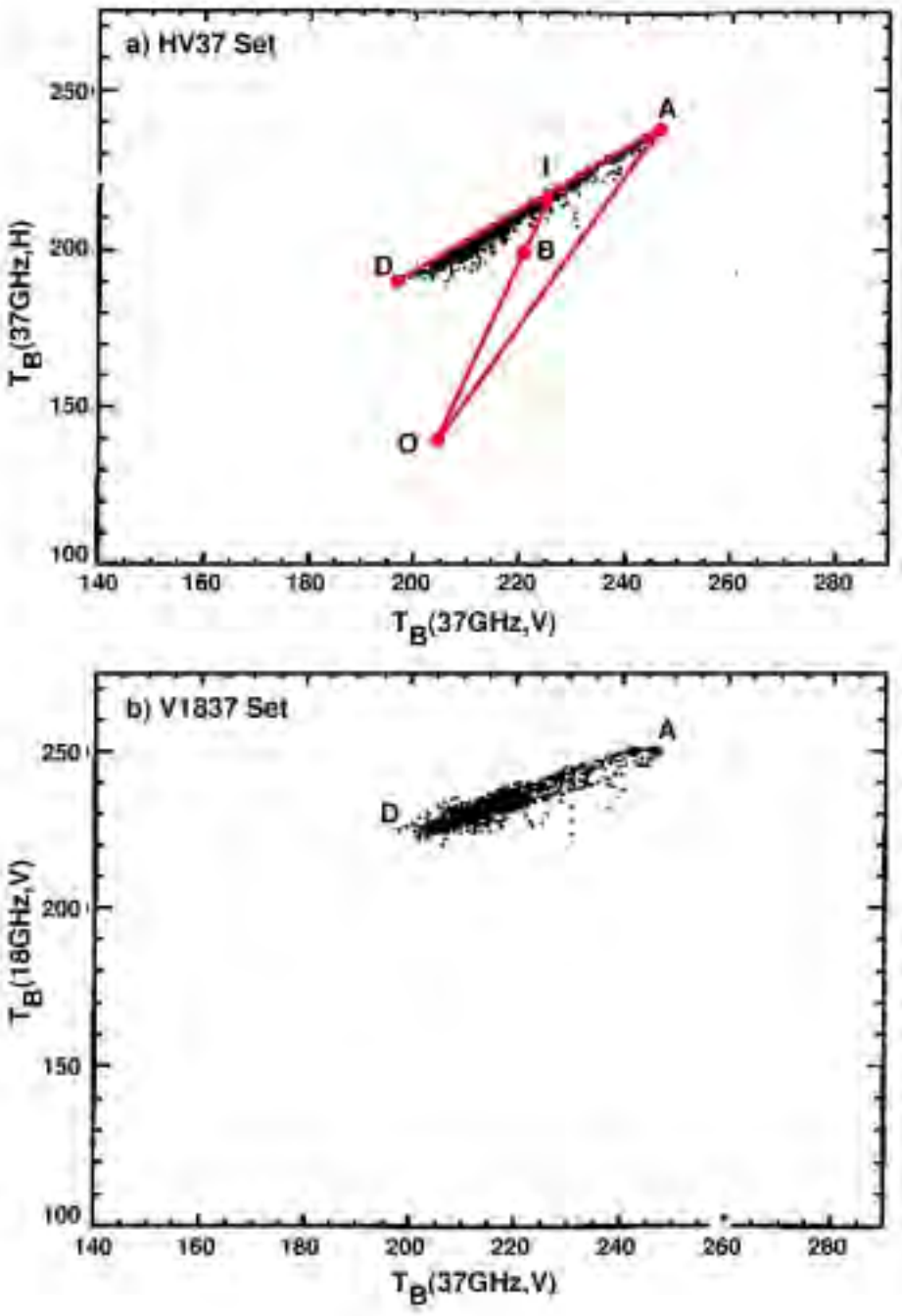

Figure 20. Scatter plot of P3a aircraft microwave radiometer data on May 20, 1987 in the Arctic using (a) 37H versus 37V channels and (b) 18V versus 37V channels. Most of the data points along the line AD have been confirmed to represent 100% ice using SAR, photography, and visual observations.

The use of V1937 is desirable because it uses solely the vertical channels which are less affected by layering and inhomogeneities in the ice (Matzler, 1984; Grenfell et al., 1994) than are the horizontal channels. This set has been found to be most suitable in the Antarctic Region (Comiso et

al., 1984; Comiso and Sullivan, 1986) where snow cover is known to have a very complex texture (Massom et al., 1996; Worby and Massom 1995). However, the V1937 set is more sensitive to fluctuations in ice temperature than the HV37 set (Comiso, 1995). Although spatial variations in surface ice temperature were observed in the Weddell Sea to be small (standard deviation of about 2K), other studies show larger variability (Sturm et al., 1996) in some areas especially for ice surfaces with little or new snow cover in the inner zone.

The enhanced AMSR Bootstrap Algorithm addresses this problem and makes use of the 6 GHz data to reduce if not eliminate temperature effects on the V1937 data set. The schematic of the procedure leading to the estimates of two parameters, namely, ice concentration and ice temperature, is shown in Figure 21. The effective emissivity of the surface within each data element is estimated from

$$\varepsilon_B = \varepsilon_I C_I + \varepsilon_O (1-C_I) \quad (7)$$

where C_I is obtained from equation (6) or equivalent formulation, while ε_I and ε_0 are emissivities of ice and open water, respectively, which can be derived from the data and assumed constant. Unlike equation (6), equation (7) is not exact but a sensitivity study indicates that the error is very small (<1%) and is highest when the concentration is 50%. The physical temperature of each data element is then given by

$$Tp = T_B (6V)/\varepsilon_B(6V) \quad (8)$$

where $T_B(6V)$ is the observed brightness temperature of the surface at 6 GHz (vertical polarization). The emissivity of the surface at 19 and 37 GHz can then be derived from

$$\varepsilon(19V) = T_B(19V)/Tp \quad (9)$$

$$\varepsilon(37V) = T_B(37V)/Tp \quad (10)$$

and

$$\varepsilon(37H) = T_B (37H)/Tp \quad (11)$$

with the assumption that Tp (19V), Tp(37V), and Tp (37H) are approximately equal to Tp (6V). The ice concentration can be inferred from these derived emissivities using a formulation similar to that described in Comiso (1995). The use of emissivity instead of brightness temperature is justified by the matching of reference data points of both consolidated ice (100% IC) and open water (0% IC). As in Comiso (1995), the tie points for the emissivity of 100% ice can be calculated from the following equations:

$$\varepsilon_{1I} = (\varepsilon_{1A} - \varepsilon_{1O} - \varepsilon_{A2} S_{AD} + \varepsilon_{2O} S_{OB})S_{OB} /(S_{OB} -S_{AD})+ \varepsilon_{1O} - S_{OB}\varepsilon_{2O} \quad (12)$$

$$\varepsilon_{2I} = (\varepsilon_{1A} - \varepsilon_{1O} - \varepsilon_{2A} S_{AD} + \varepsilon_{2O} S_{OB})/(S_{OB} -S_{AD}) \quad (13)$$

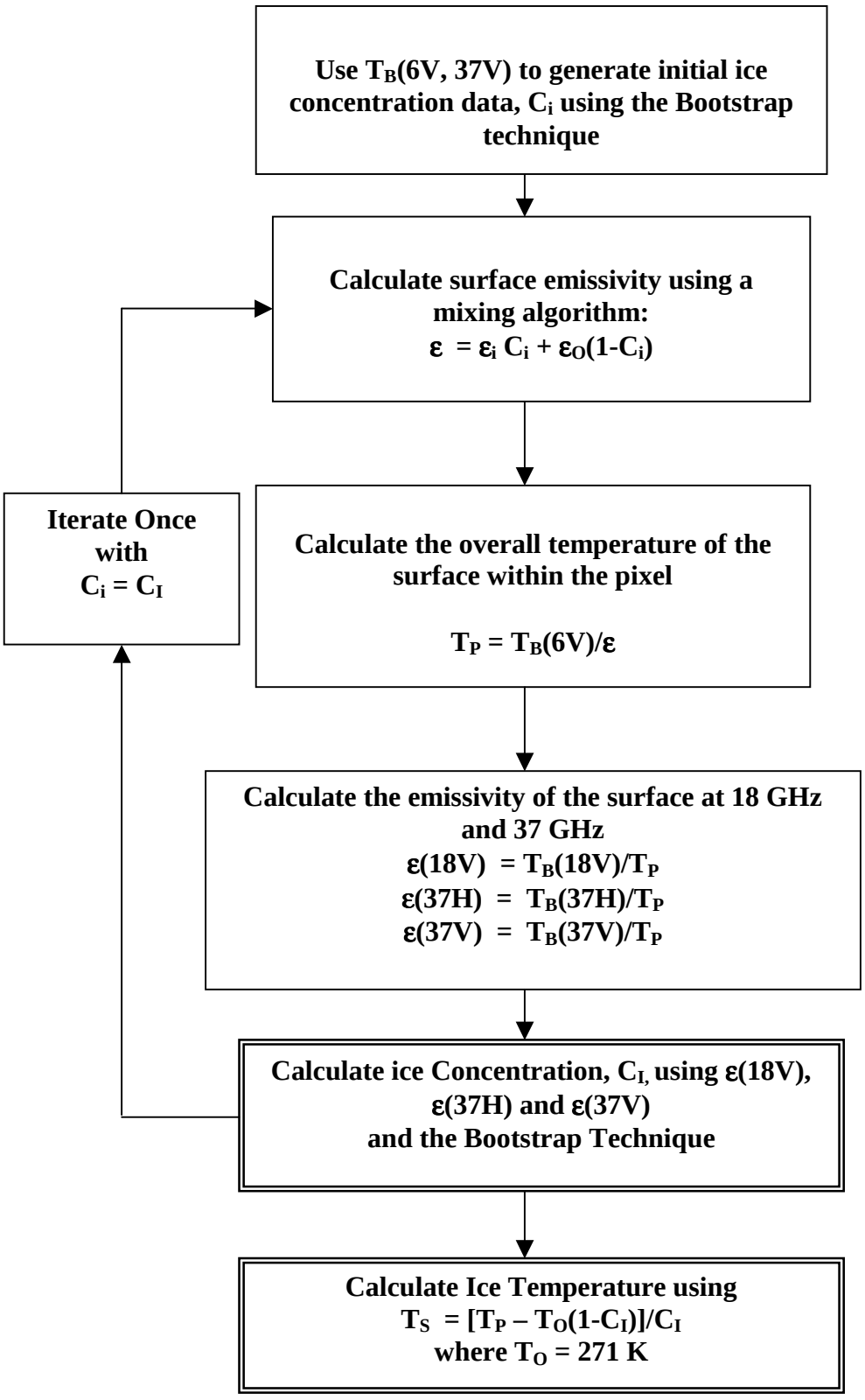

Figure 21. Schematic diagram illustrating how ice concentration and ice temperature are derived from AMSR brightness temperature and derived emissivity data.

where S_{AD} and S_{OB} are slopes of the lines AD and OB, respectively, (ε_{1A} , ε_{2A}) represents any point along the line AD, and (ε_{1O} , ε_{2O}) represents the open water reference brightness temperature. The ice concentration for any data point B can be derived from the ratio of the distances OB and OI given by the equation (see Figure 20):

$$C = [\{(\varepsilon_{1B} - \varepsilon_{1O})^2 + (\varepsilon_{2B} - \varepsilon_{2O})^2\} / \{(\varepsilon_{2I} - \varepsilon_{2O})^2 + (\varepsilon_{1I} - \varepsilon_{1O})^2\}]^{1/2} \qquad (14)$$

In the formulation, it is convenient to choose $\varepsilon_{2A} = 0$ at point A along AD with ε_{1A} the resulting offset. Additional details, including the determination of the line AD and the point O, are discussed in Comiso (1995). Since the initial calculation of the emissivity at 6 GHz makes use of ice concentration that has not been temperature corrected, the emissivity is recalculated using the more accurate result from equation (14) and using the same procedure, the ice concentration is recalculated. The final value will be the estimate of ABA for sea ice concentration. Also, the final value of Tp is the estimate of the physical temperature within the footprint of the satellite. To illustrate the performance of ABA in deriving surface ice temperatures, ice temperature maps during the first and final iterations are shown in Figures 22a and 22b. In Figure 22a, the distributions look more uniform than Figure 22b mainly because the map was derived using primarily the 6 GHz data which has relatively coarse resolution. In Figures 22b, there are more details since the data reflect those of the 18 and 37 GHz data which have much better resolution than the 6 GHz data. However, the overall distribution of temperatures is consistent with expectations. The coldest areas in the maps are in the Western Weddell and the Amundsen/Bellingshausen Seas where ice is known to survive during the summer. In the Weddell Sea, the cold area is further north because the summer ice had been advected north partly by the Weddel Gyre. Since these are the areas where ice begins to grow in autumn, they have thicker and more consolidated ice cover and hence generally colder surface temperatures than other areas. The differences between the two maps are mainly associated with the large footprint of the 6 GHz channel which provides average concentration over a much larger area than the other channels. It is expected that with the use of AMSR data, differences will be considerably reduced because of much better resolution.

For comparison, ice concentration maps derived using the original Bootstrap Algorithm and ABA are presented in Figures 23a and 23b, respectively. The two maps look very similar with the areas of high ice concentrations and reduced concentrations confined in the same general locations. The ice concentration maps are consistent with observations, as will be presented later, and with expected behavior of the ice cover based on known polar processes such as the formation of polynyas in the coastal regions and in some deep ocean regions (near the Maud Rise and the Cosmonaut Sea). A difference map between the original Bootstrap and ABA ice concentrations is shown in Figure 23c. Relatively higher concentrations (by about 5%) are observed with the ABA in the Bellingshausen /Amundsen Seas which is where improvements are expected because of colder temperatures. Also, lower concentrations are observed at the ice edges but this may just be due to a difference in the positioning of the open ocean tie points. These maps were generated using regional tie points as described in the following section.

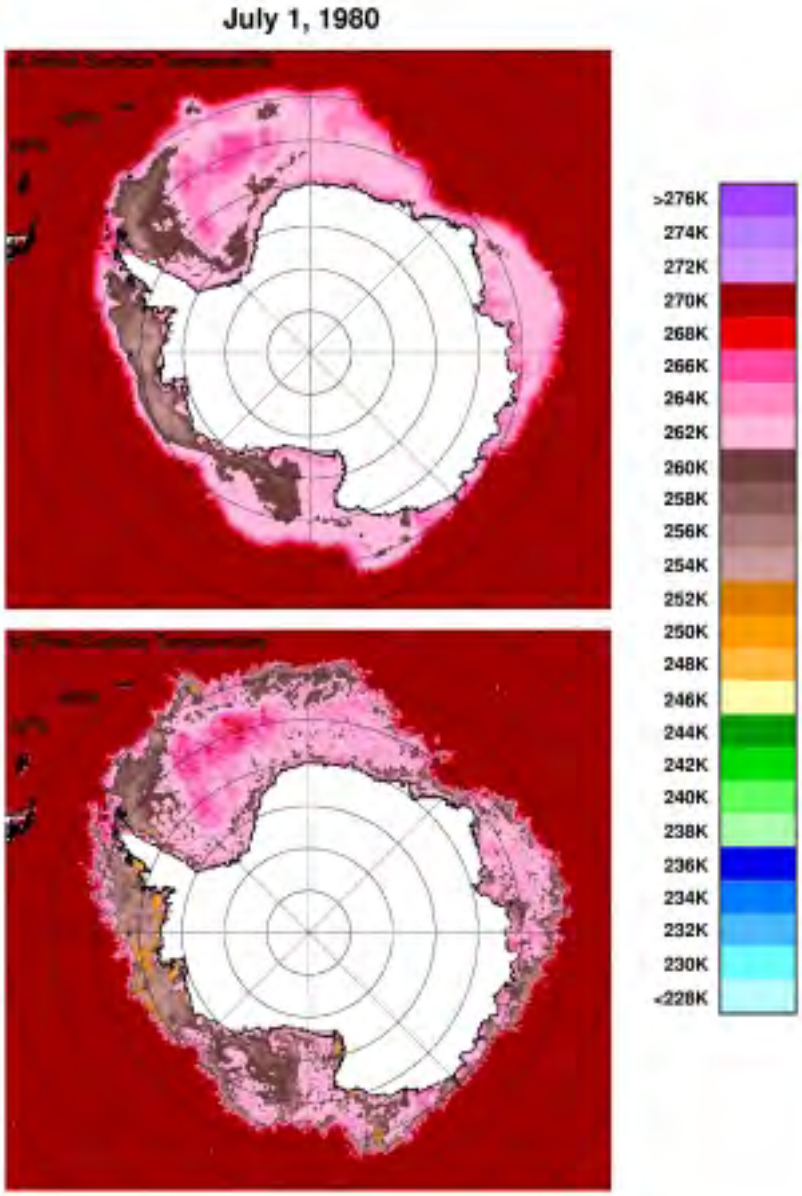

Figure 22. Antarctic ice temperatures on July 1, 1980 inferred from SMMR data (a) at first iteration, and (b) at the final iteration.

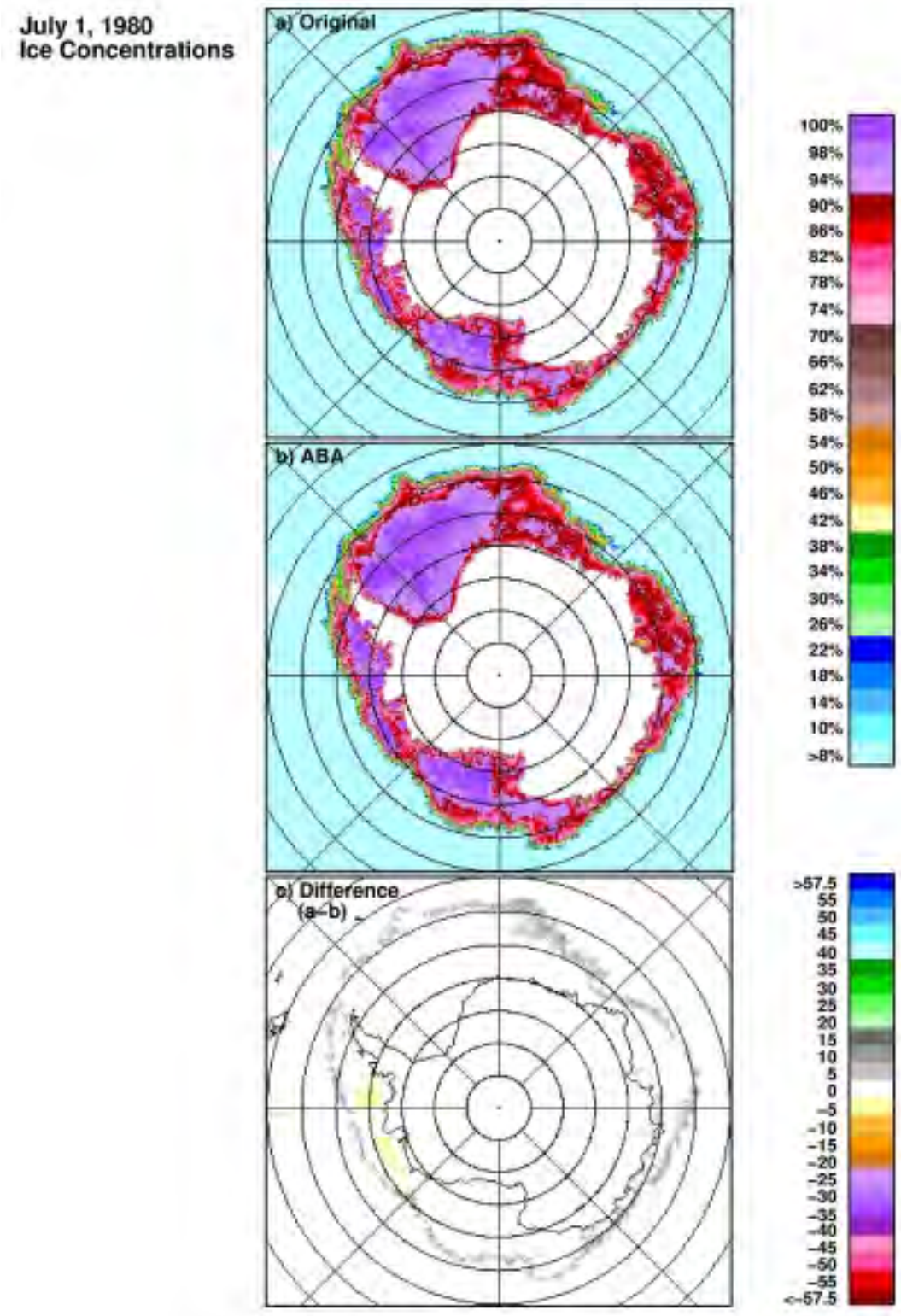

Figure 23. Antarctic ice concentrations derived (a) from the Original Bootstrap Algorithm using brightness temperatures alone, and (b) from the AMSR Bootstrap Algorithm using the 6 GHz to correct for spatial variations in temperature. (c) Difference of the ice concentrations derived using (a) and (b).

3.1.2.3 New Enhancements

The signature of the Antarctic sea ice cover has been considered to be similar to that of a seasonal sea ice cover since even in the Weddell Sea where a large fraction of the sea ice cover survives summer, the signature of ice in the Western Weddell Sea region is similar to those of other regions (Zwally et al., 1983). However, although the sea ice that survives the summer in the Bellingshausen/Amundsen Seas region appears to have a different signature in the subsequent winter, the sea ice algorithms, including the original Bootstrap Algorithm, did not take this into account. Accurate characterization of the sea ice cover in the region is desirable, especially since the region has been identified recently as a climatologically anomalous area (King and Harangozo, 1998; Jacobs and Comiso, 1997). In Figure 24a, a scatter plot of 19V versus 37V data points from the entire Antarctic region on June 17, 1979 is shown. The tie point for ice is along the line labeled AD. The same set of points are shown in Figures 24b and 24c but the data points in the Weddell, Indian, and West Pacific sectors (called region 1) were plotted separately from those in the Bellingshausen, Amundsen, and Ross Sea sectors (call region 2), as indicated. It is apparent that the slope of the data points for consolidated ice (i.e., along AD) in one region is different from that of the other region. The use of one set of tie points, as in Figure 24a, for the entire Antarctic region yielded the color coded ice concentration map shown in Figure 25a, while the use of a separate set of tie points for the two regions, as indicated in Figures 24b and 24c, yielded the map in Figure 25b. The ice concentration maps are basically the same in the two regions except towards the west of the Antarctic Peninsula where a large area with 70% ice concentration (brown) or less is apparent in the original data set (Figure 25a) but is shown to be much more consolidated and more consistent with observations from other sensors (e.g., AVHRR) in the new one (Figure 25b). The historical SMMR data indeed shows that in the previous summer of 1979, highly concentrated ice survived in the same area identified as a relatively low concentration area (brown) in Figure 25a. This indicates that there was a dominance of a type of multiyear ice in the region, the emissivity of which is different from those of other Antarctic regions.

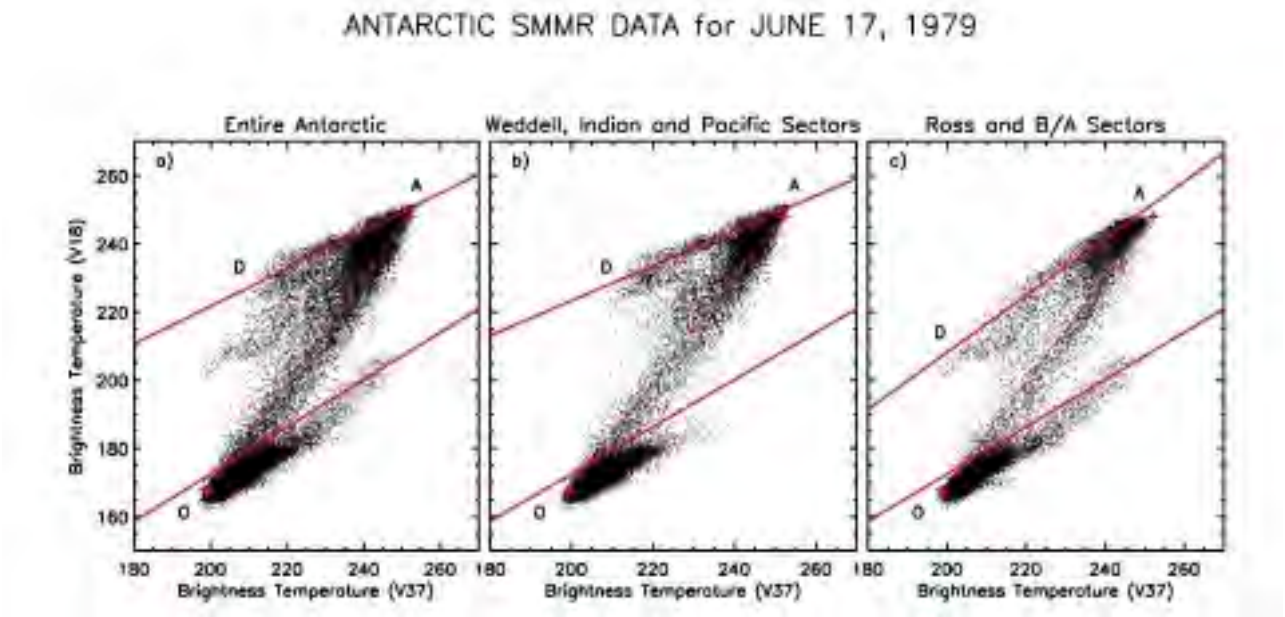

Figure 24. Scatter plots of 18 GHz(V) versus 37 GHz(V) on June 17 for (a) the entire Antarctic region, (b) the Weddell, Indian, and Pacific Sectors, and (c) the Ross and Bellingshausen/ Amundsen Seas sector.

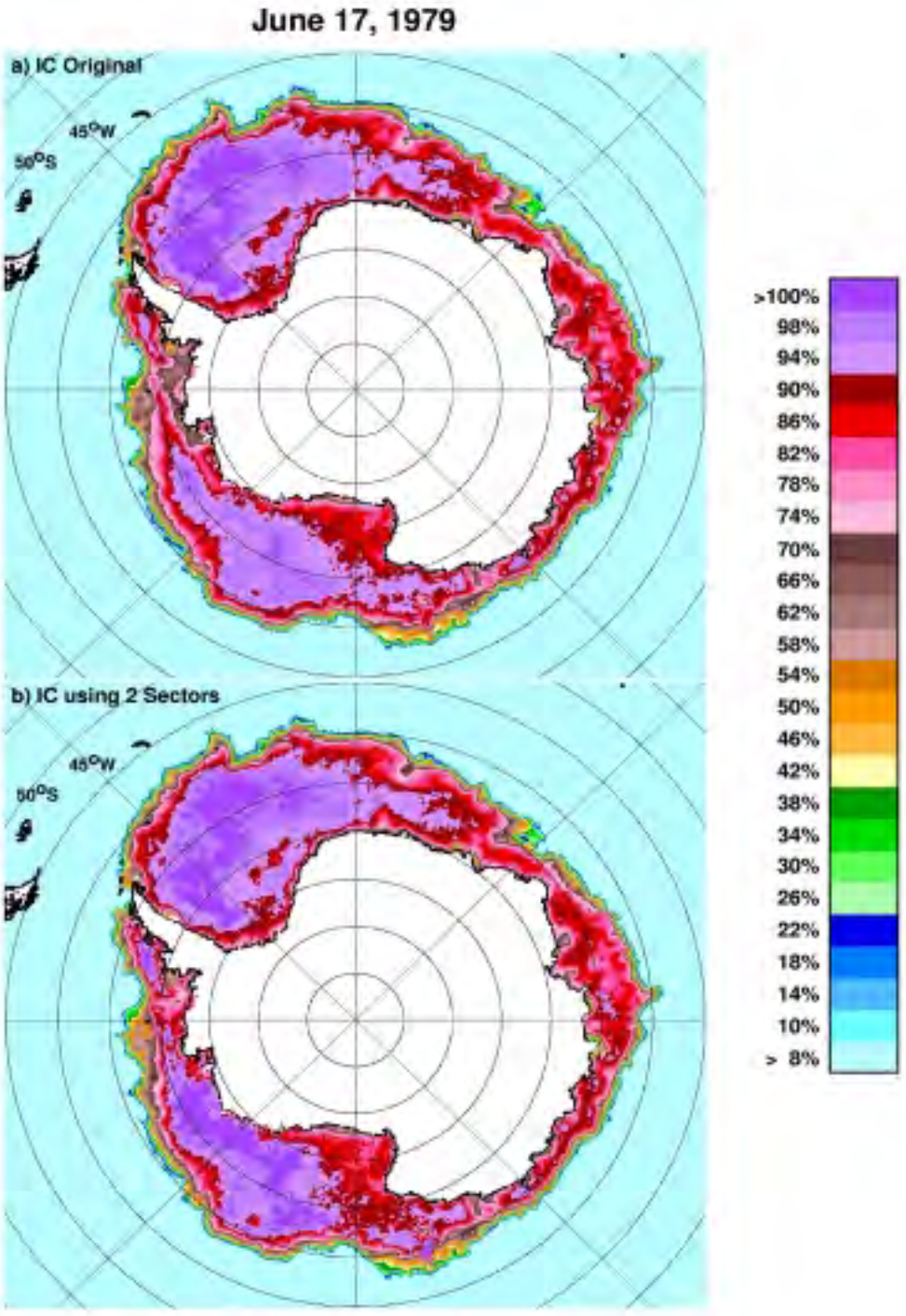

Figure 25. Antarctic ice concentration maps on June 17, 1979 (a) with tie-points taken from the entire Antarctic region, and (b) with tie-points separately for the two regions (1 and 2) as described in the text.

Tie-points have also been checked for compatibility of results in sea ice concentration determination as the source of brightness temperature data changes from one microwave instrument to another. When applying the original tie-points (Comiso 1995), the frequency distribution of ice concentrations (Figure 26a) are found to be different for SMMR (in black) when compared with SSM/I (in red) during overlap period. In highly consolidated ice areas, the amplitude and standard deviation of the SSM/I peak are considerably different from those of the SMMR peak. When combining data from the two sensors, this discrepancy can cause problems in assessing long term changes in sea ice cover. However, the peaks can be made almost identical by slightly adjusting the sea ice tie-points. The use of the linear regression technique for both SMMR and SSM/I turned out to be appropriate for this purpose since when applied, the results show much better agreement (Figure 26b). This technique also improves the consistency in the estimate of sea ice extent and area from SMMR (solid line) and SSM/I (dashed line) during the period of overlap (Figure 27). This makes it unnecessary to apply a normalization on one set of data to make the two data sets consistent during periods of overlap. The regression technique provides a new slope and offset daily for the line AD but the slope and offsets were found to change little during winter except during adverse weather conditions. These daily calculations improve data consistency not just between the SMMR and SSM/I sensors but also between the different SSM/I sensors (e.g., F8, F9, F11, and F14). The use of this technique thus provides a better representation of the time sequence of sea ice cover.

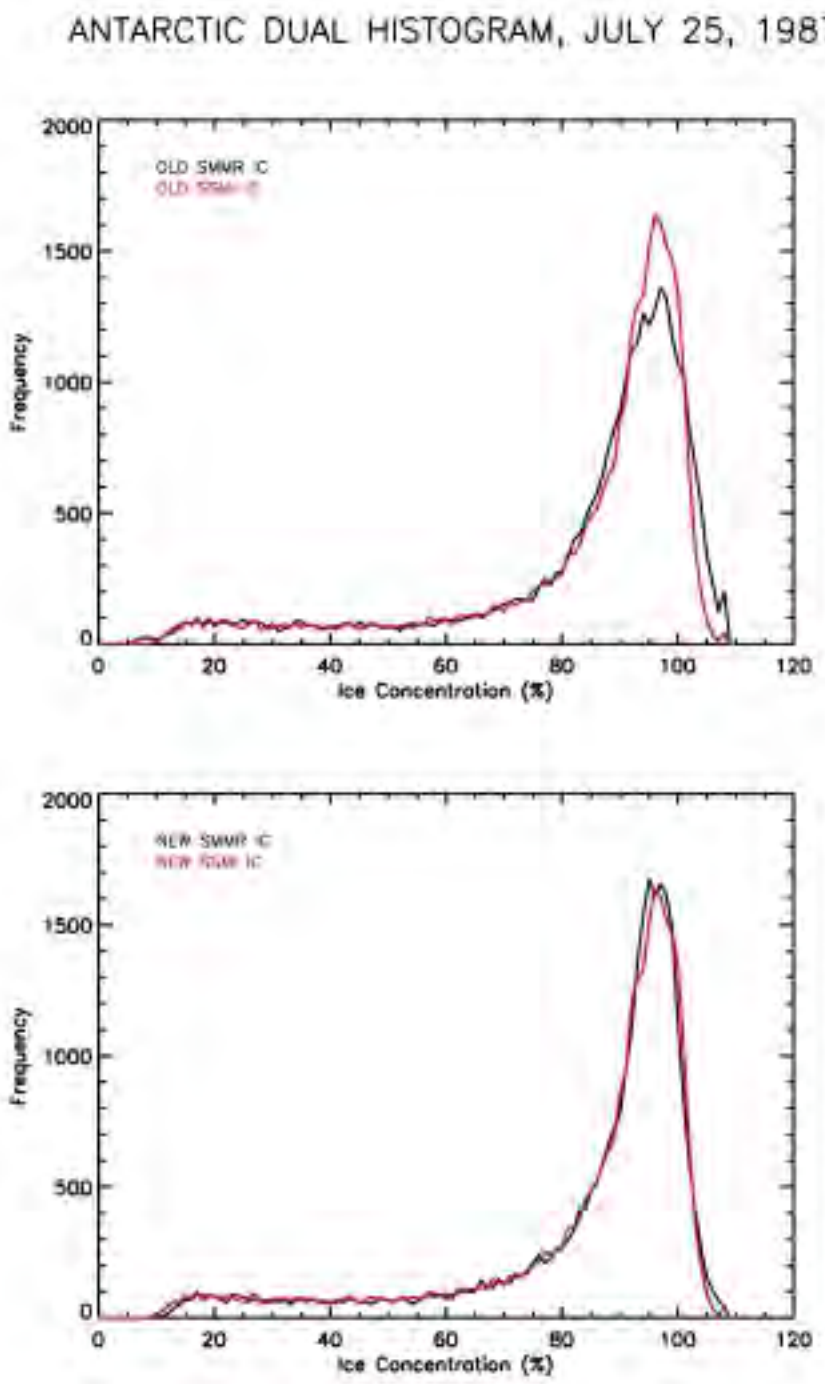

Figure 26. Ice concentration frequency distributions during periods of overlap of SMMR (black line) and SSMI (red line) data without and with regional tie-points.

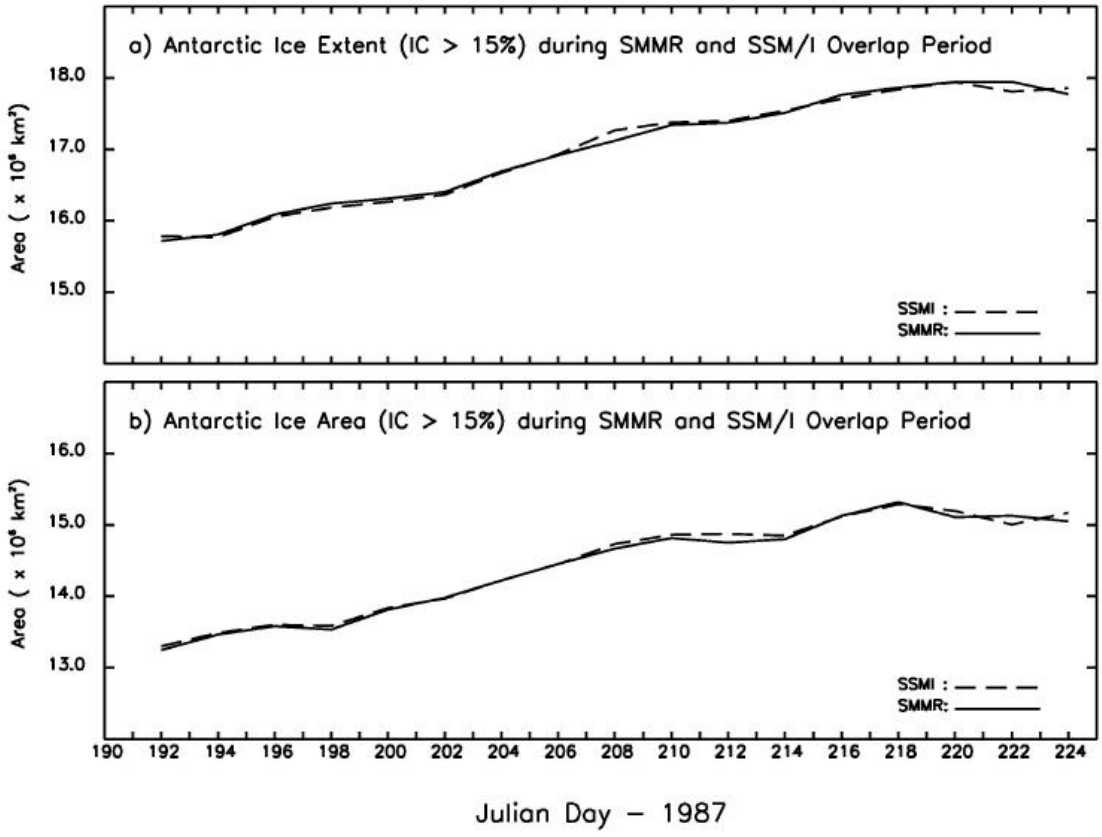

Figure 27. Ice extents from SMMR and SSMI during the period of overlap in 1987.

3.1.2.4 Sensitivity Studies and Uncertainty Estimates

The physical basis behind the Bootstrap algorithm has been confirmed using ground based radiometer experiments in the Antarctic and controlled sea ice experiments at the Cold Regions Research Laboratory (Comiso et al., 1989; Grenfell et al., 1994; Grenfell and Comiso; 1986). Comparative studies with aircraft, SAR, Landsat, and Helicopter data have also been made indicating consistencies generally within 5% in winter and higher in the summer, and confirming validity of the assumptions (Comiso et al., 1984; Comiso, 1986; Comiso et al., 1991; Comiso and Kwok, 1996). The 5% accuracy estimate is actually consistent with the standard deviation of the peak for the consolidated ice region in the ice frequency distribution shown in Figure 26b. The distribution is useful because an upper limit of 100% ice concentration is not applied on the data. In this case, the standard deviation is slightly less than 5% but could even be better if the distribution did not include contributions from data with some real open water surfaces, which contaminated the left side of the peak and caused the asymmetry in the distribution. In the Arctic during winter, the peak of a similar frequency distribution of consolidated ice has even lower standard deviation at about 2.5%. This implies that the uncertainty in the retrieved ice concentration

in this region can be as good as 2.5% which is small enough to enable the detection of true open water areas in the highly compact Arctic environment.

Sensitivity studies for errors due to variations in temperature and emissivity has been reported previously (Comiso, 1995; Comiso et al., 1997). Since the actual spatial variations in temperature and emissivity is not known, the best procedure for assessing errors due to these effects is through the use of available ancillary data. To study temperature effects, monthly surface temperatures derived from satellite infrared data are used, examples of which are shown in Figures 28a and 28b. Daily averages are not used since the percentage of missing data for the surface is usually large each day due to cloud cover. The monthly averages, however, are actually better representation of snow-ice interface temperatures, where much of the observed microwave radiation comes from, since the latter is usually much more stable than the temperatures on the snow surface (Comiso, 1995). The temperature maps show changes in temperature from the outer ice zone to the inner zone and are spatially coherent. The temperature distribution from a single month of July (Figure 28a) shows slightly more spatial variability than that for the multiyear averages (Figure 28b) but overall, regions of cold and relatively warmer temperatures are where you would expect them. In the July 1998 data, areas of relatively warm temperatures (oranges and yellows) are apparent in regions where open water and new ice are expected due to persistent coastal polynyas. These areas are also reflected as areas where the concentration approaches 90% in the ice concentration maps. The approximately 10% open water estimated in these areas may be an overestimate since new ice which are expected to dominate these areas have significantly lower emissivity than thick ice (Grenfell et al., 1992). However, as indicated earlier, such overestimates in these areas are likely more suitable for process and modeling studies since the heat fluxes from new and thin ice are considerably higher than those of thick ice (Maykut, 1978). It is thus fortuitous to have this sensitivity to new ice since it enables identification of polynyas and regions of divergence which are very important in polar processes. The multiyear average of temperature in July (Figure 28b) shows a more uniform progression of temperatures from the continent to the ice edge. However, the relatively warm areas in coastal regions around the continent are located at approximately the same regions as in July 1998 indicating persistence of the coastal polynyas in these regions. The latter includes the Ross Sea Polynya (Jacobs and Comiso, 1989) near 178^{o} E, the adjacent Terra Nova Bay Polynya (Bromwich et al., 1990), Cosmonaut polynya (Comiso and Gordon, 1998) and others (Gordon and Comiso, 1988).

The July 1998 monthly surface temperatures in Figure 28a were converted to ice surface temperature using the regression results in Comiso et al. (1989) and used by ABA, instead of a 6 GHz data (which is not available with SSM/I) to calculate ice concentrations. For comparison, ice concentration from the original Bootstrap Algorithm is also calculated and the results together with the differences are presented in Figure 29. The two results are actually practically the same and agree to within almost ±2%. This indicates that temperature effects are not really a big source of error for the original Bootstrap Algorithm as discussed in Comiso (1997). To gain more insight into the temperature effect, brightness temperature scatter plots are compared with emissivity scatter plots separately in the two Antarctic regions in Figure 30. The green dots are areas where the surface temperatures are 250 K and colder. What the scatter plots indicate is that after surface temperature corrections have been incorporated in the form of emissivity plots, the data points are rearranged in such a way that the cluster of data points have patterns which are very similar to those of the brightness temperature plots. This is a confirmation that surface temperatures plays a minor

role in the scatter of data points in the TB scatter plots and that the variability is likely due to different physical surface characteristics. Further studies, however, are needed since the conversion of surface temperature to ice temperature may not apply everywhere, especially where there is little or no snow cover as in young and thin ice regions. This will be further investigated through validation studies and analysis of more ship data.

The effect of spatial variations in emissivity can be studied through analysis of the characteristics of consolidated ice clusters as depicted in Figure 30. The variability of the data points in the clusters are associated with variations in both emissivity and temperature. The original Bootstrap Algorithm and ABA make use of the linear pattern of the clusters of actual satellite data of consolidated ice to estimate the emissivity of the ice that is used as tie point in each observation field. This is the intercept of the lines OB and AD in Figure 30a. The random error of the estimate of the tie point can be inferred from the compactness of the cluster of points along the line AD. The more defined the cluster of points, the less uncertainty there is at identifying the line. In the Arctic region where the 37 GHz (H) and 37 GHz (V) data are mainly used, the data points in winter and fall are very compact and well defined. The distribution of consolidated ice data points along the line OB have standard deviations of about 2% which makes the set of channels very valuable for identifying <5% open water regions in the Arctic. However, the same set of channels are not so effective in the Antarctic and the seasonal regions of the Arctic because of higher sensitivity of the horizontal channel than the vertical in these regions due to surface, layering and other effects. In these regions, the standard deviation of consolidated ice area data points along OB, using SSM/I and SMMR data, is greater than 5%. It is expected that this will improve when actual AMSR data are used due to better resolution.

During spring and summer, effects such as surface melt and meltponding cause larger errors in the retrieval. Previous studies using comparative studies with SAR data have indicated that errors in the ice concentration determinations over meltponded areas can be as large as 20% (Comiso and Kwok, 1996). These errors can be reduced through proper adjustment of tie points and perhaps with the use of other channels (e.g., 10 or 85 GHz) from AMSR.

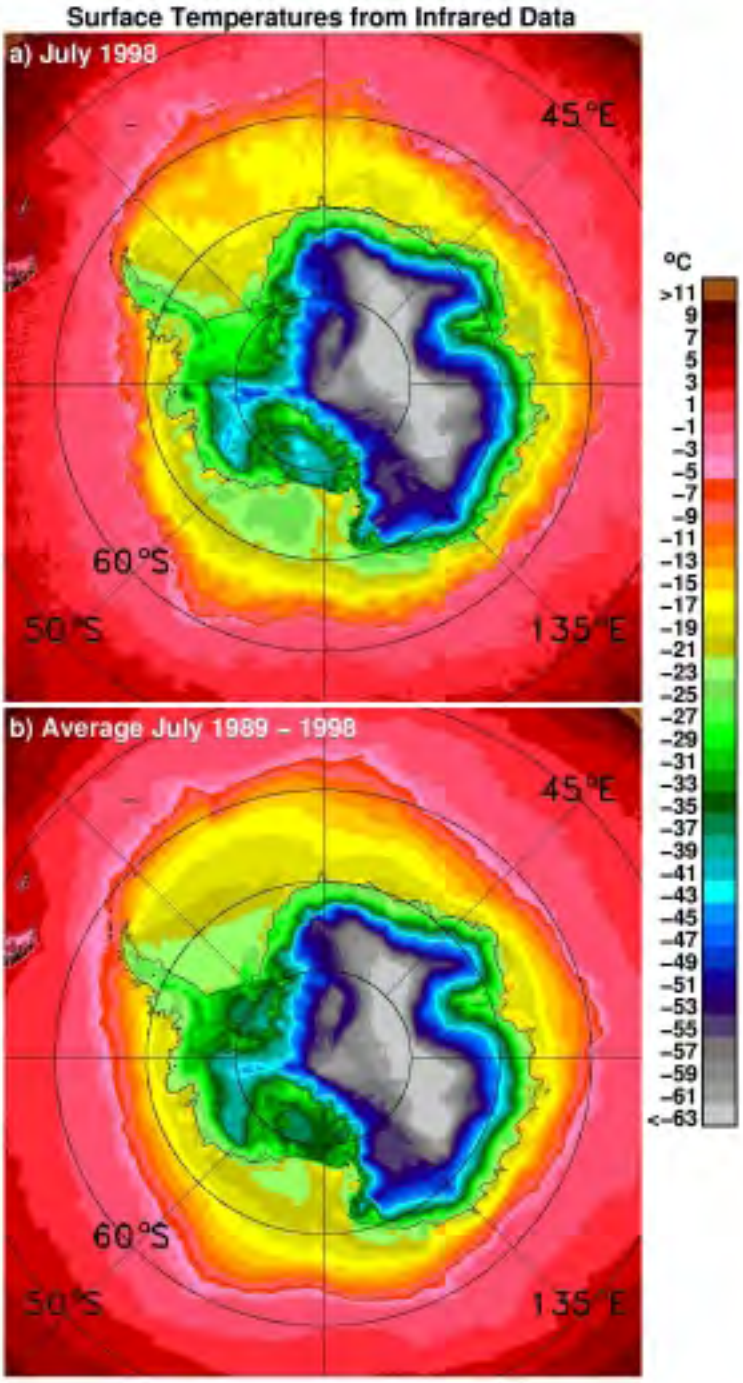

Figure 28. Surface temperatures derived from AVHRR (a) averaged for the month of July 1998 and (b) averaged for all months of July from 1979 through 1998.

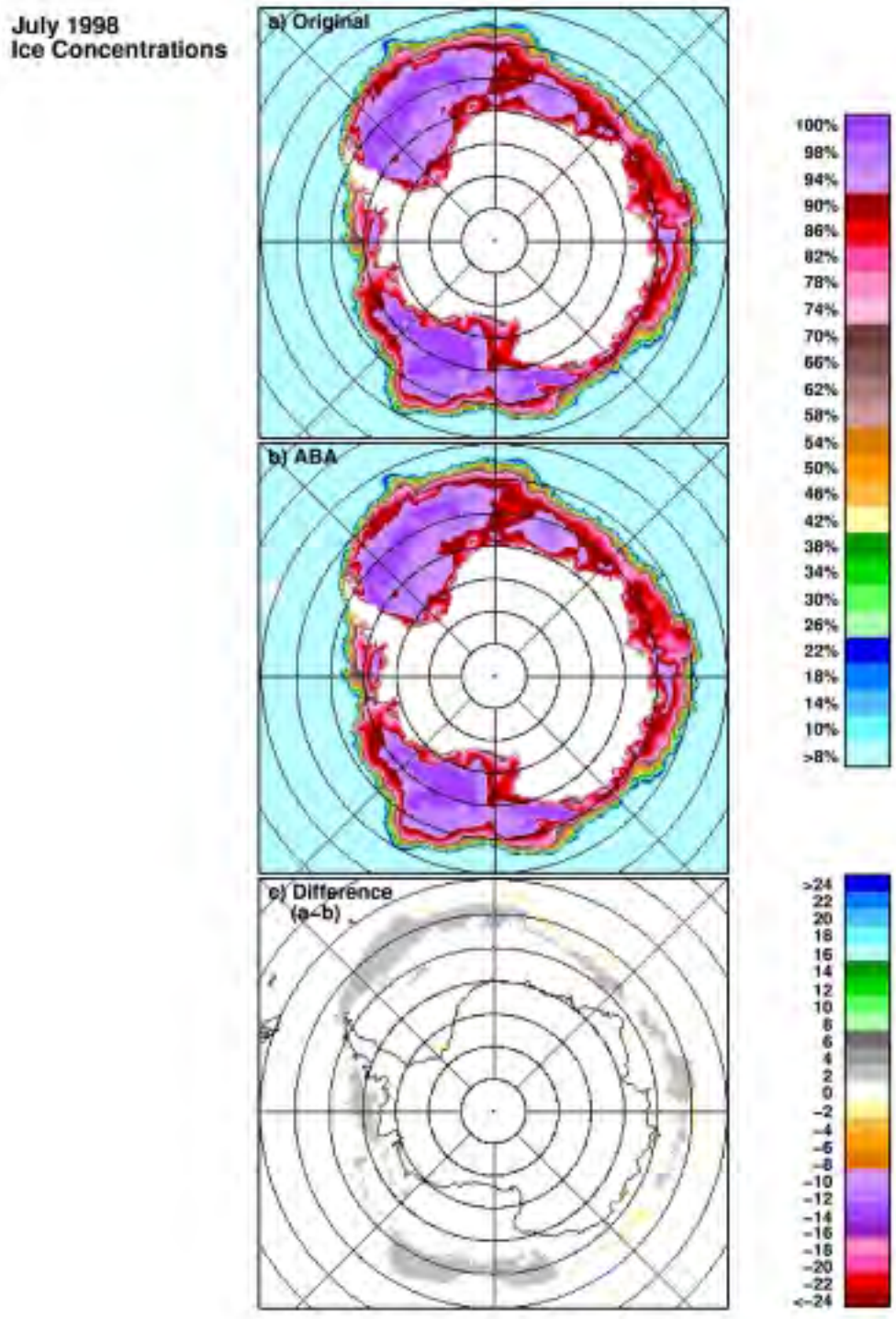

Figure 29. Sea ice concentrations in July 1998 using (a) the original Bootstrap Algorithm and (b) the AMSR Bootstrap Algorithm. (c) Difference of the original and the AMSR Bootstrap Algorithm.

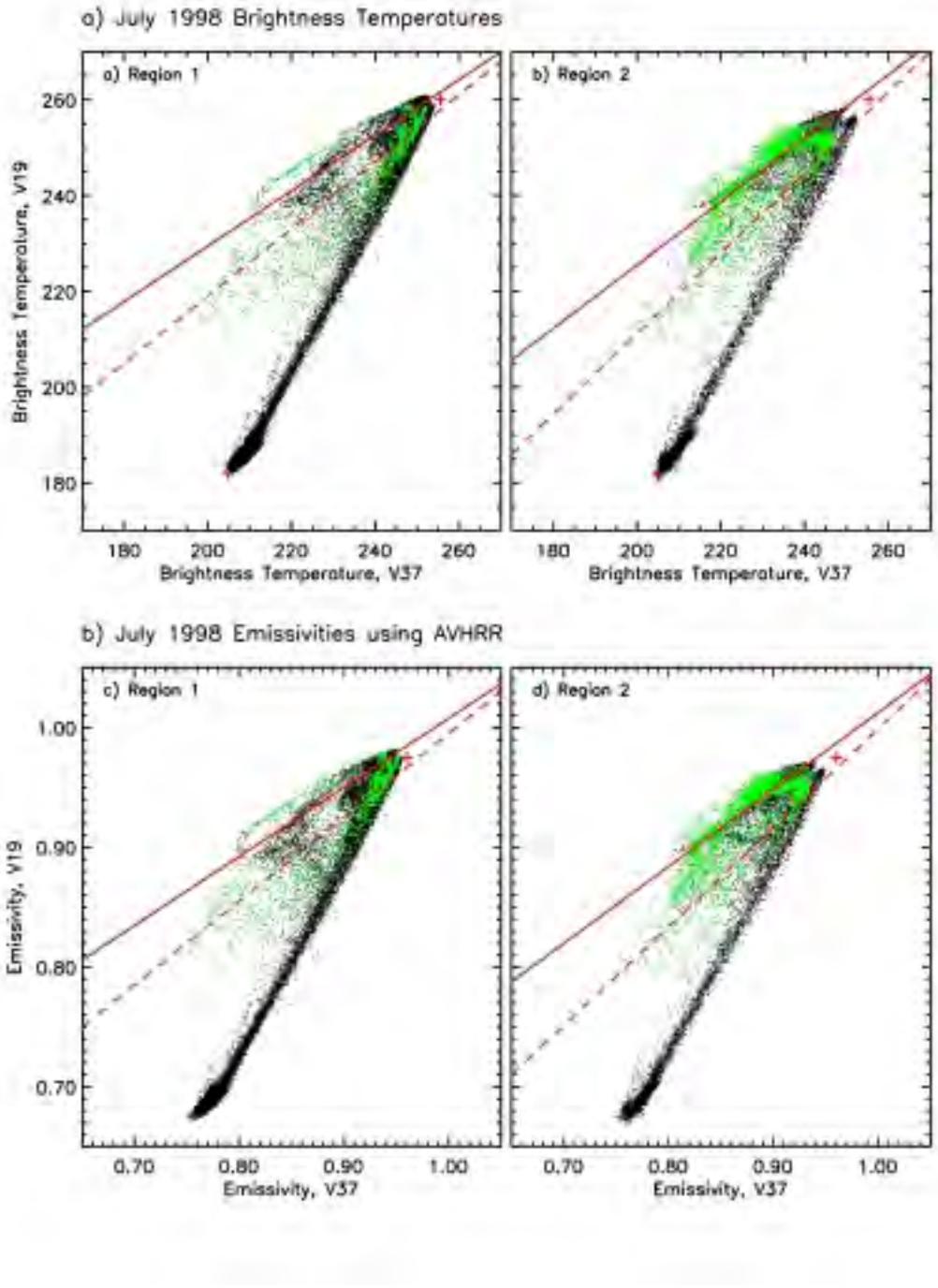

Figure 30. Scatter plots of brightness temperatures in July 1998 for 19 GHz(V) versus 37 GHz(V) for (a) region 1 and (b) region 2. Scatter plots of emissivities for 19 GHz(V) versus 37 GHz(V) for (c) region 1 and (b) region 2.

3.1.2.5 Validation Studies

The lack of a good validation data sets have made it difficult to assess the accuracy of the ice concentration products. This is specially true in the Antarctic where the availability of high resolution satellite data is very limited and aircraft validation data over sea ice is practically non-existent. With the advent of Landsat 7, however, it is expected that more cloud free data will be made available for validation. MODIS data from the currently launched EOS-Terra satellite will also be very useful. Furthermore, some aircraft overflights over the Antarctic and the Arctic are being planned as part of the validation program after the launch of AMSR. The overflights are needed to provide direct validation and to ensure that the interpretation of Landsat and other ancillary data are correct. In this section, validation studies using the limited data currently available set will be discussed.

Because of its high resolution (at 35m) and a swath width of 185 km, cloud free Landsat images usually provide the spatial detail and coverage that are needed to validate ice concentration products. Such data have not been available in the Antarctic during the last few years but it is anticipated that the advent of Landsat 7 in 1999 will provide much needed global and seasonal coverage. One of the very few cloud free data in winter that is available is an image on September 18, 1988. This data is especially useful because it is a winter image located in the middle of the pack. For this day, only SSMI data are available and there are no 6 GHz data to be used for correcting the Bootstrap Algorithm. To correct for temperature effects, this time climatological average of ice temperature from Gloersen et al., 1992 were used in conjunction with ABA to derive ice concentration. The emissivity is calculated in a similar manner as indicated earlier and the ice concentration map is shown in Figure 31a. As indicated earlier, the results from the original Bootstrap Algorithm is practically the same. The Landsat image for the same day is shown in Figure 31b with the location indicated as a box in the SSM/I ice concentration image. The result from ABA inside the box shows an average of about 100% while analysis of the Landsat data indicates the presence of 90% thick ice, 9% nilas and 1% open water. Assuming an emissivity of 0.8 instead of 0.92 for nilas, it is expected that passive microwave data should provide a concentration of 98%. The derived concentration product derived by ABA thus show good consistency with this Landsat image. Other Landsat images are available but very few are for a winter period and most are near the continental margins. In general, the derived concentrations agree with Landsat to within 1 to 10%. Larger discrepancies occur near the ice edges which are usually covered by wet pancake ice and during summer melt when the emissivity of the ice cover is less predictable. Cloud free OLS data have also been used and results show good agreement with results from the Bootstrap Algorithm.

A case that requires special consideration is the ice cover in coastal polynya regions such as the Ross Sea polynya where strong synoptic winds from the south are usually persistent. These winds cause ice advection to the north and the formation of new ice in the displaced areas along the coastal region. This phenomenon is illustrated in the SSM/I image of Figure 32a where concentrations along the coastal area are generally near 70% while the concentrations in the neighboring areas to the north are near 90%. An AVHRR image for the same day for the area in the box is shown in Figure 32b and although the image is of poor quality, it is apparent that the polynya region is a region of high dynamic activities that cause the formation of new ice. While

the concentration from the AVHRR image may be higher that what is derived from the Bootstrap Algorithm, the type of ice is different and associated more with new and young ice. The different emissivity for this ice type makes it difficult to obtain actual open water determinations as described by Comiso et al. (1992). However, as indicated earlier, the overestimate of the concentration of new and young ice may be fortuitous since it enables identification of polynyas and more accurate assessment of heat fluxes.

A similar situation is applicable in the Odden region, as shown in Figure 33. On March 15, 1979 the ice cover derived from the Bootstrap Algorithm (Figure 33a) shows ice concentrations as low as 70% within the Odden region. The corresponding AVHRR image in Figure 33b show similar ice distributions. However, a better accounting of the ice cover through the use of higher resolution data have indicated new and frazil ice between the bands making ice concentration higher than is apparent. Again, this is where an ice algorithm may not provide the actual percentage of open water but provides more useful information for ice process and modeling studies. In the Odden image of February 26, 1987, the ice was a lot more compact as revealed by both SSM/I and AVHRR data. In this case the agreement is very good except near the ice edge where instrument side lobes and effects of wetness can cause underestimates in ice concentration.

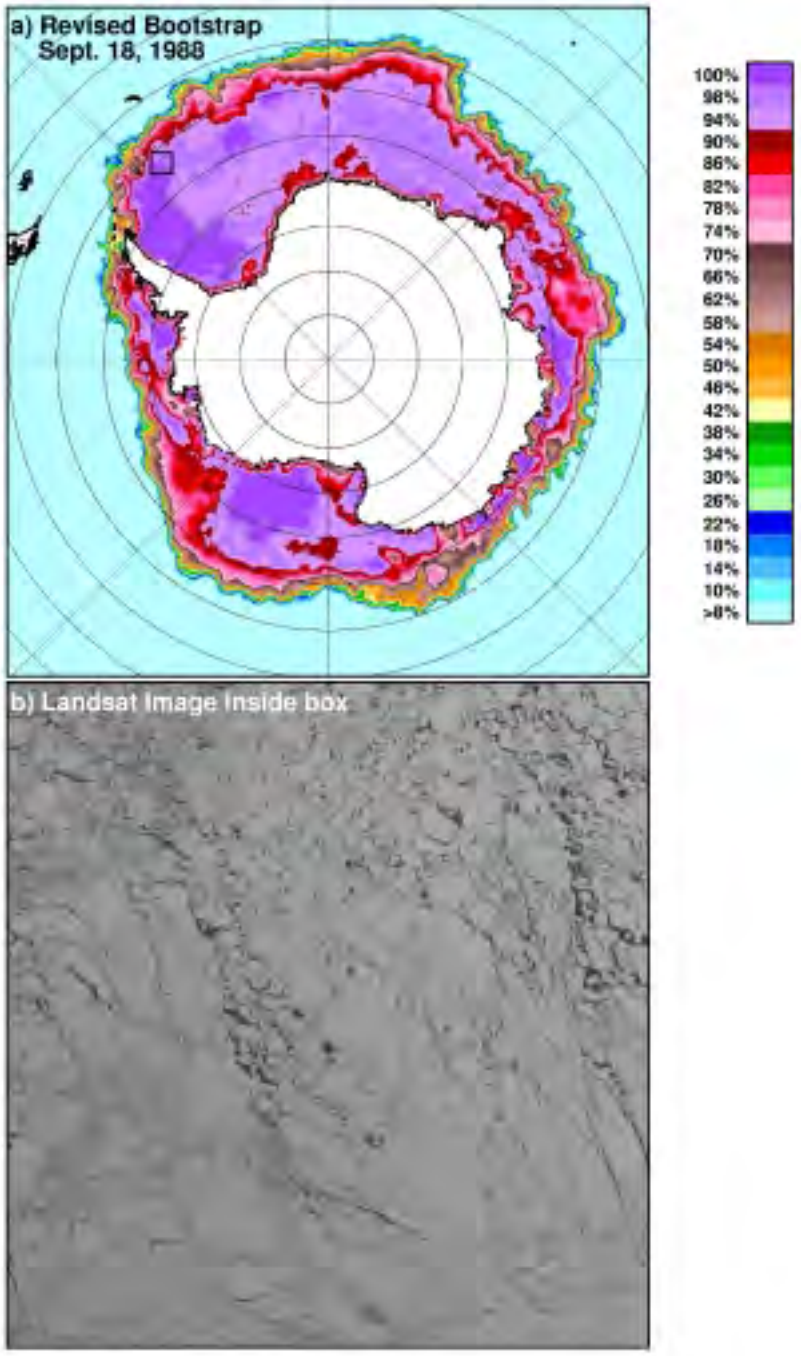

Figure 31. Comparison of (a) ice concentration map derived using the AMSR Bootstrap algorithm and temperature climatology and (b) Landsat image at the location indicated by a box in (a) for the same day (September 18, 1988). The general area of comparison is the Weddell Sea.

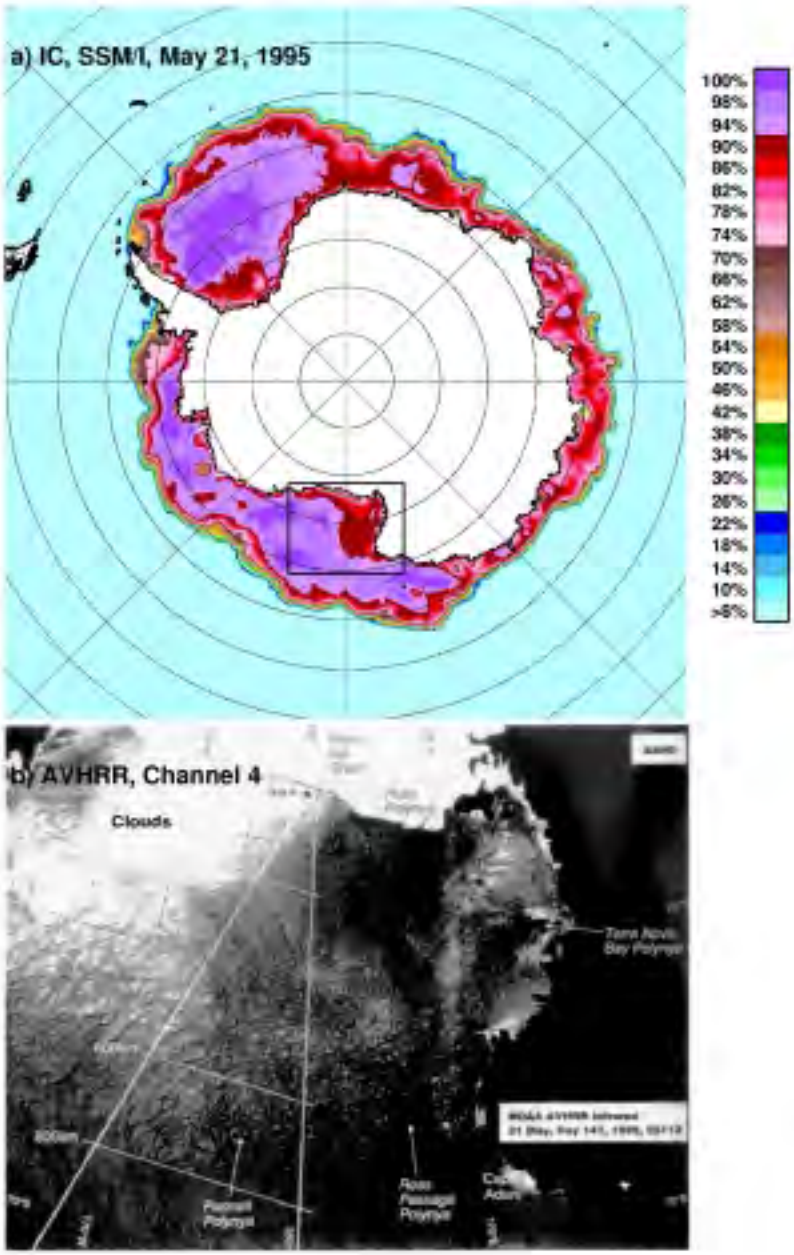

Figure 32. Comparison of (a) ice concentration map derived from SSMI using the Bootstrap Algorithm on May 21, 1995 and (b) AVHRR image on May 21, 1995. The general area of comparison is the Ross Sea polynya region.

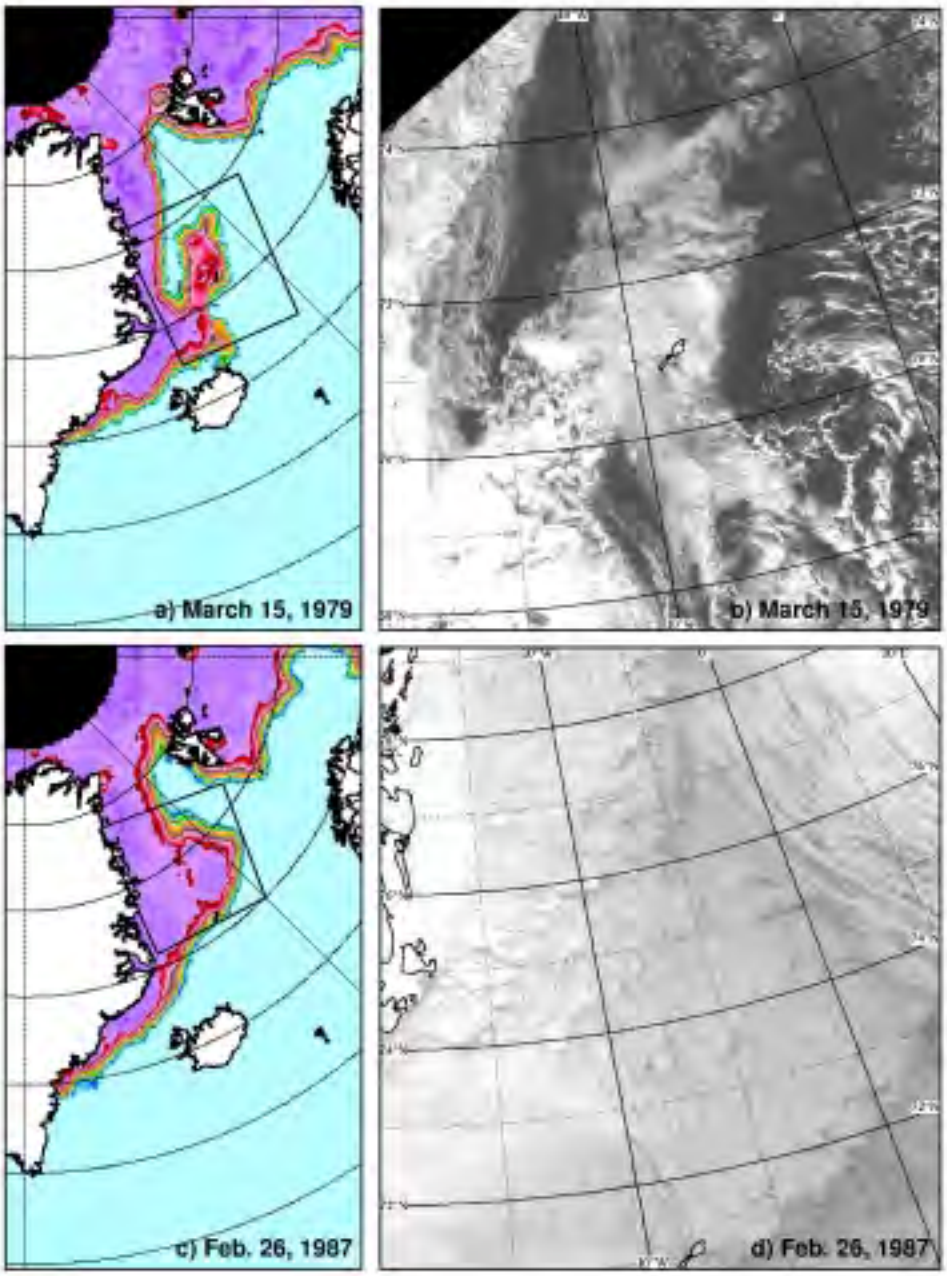

Figure 33. (a) Ice concentration map derived from SSMI using the Bootstrap Algorithm on March 15, 1979; (b) AVHRR channel 1 image on March 15, 1979; (c) ice concentration map derived from SSMI using the Bootstrap Algorithm on February 26, 1987; and (d) AVHRR channel 1 image for February 26, 1987. The general area of comparison is the Greenland Sea Odden region.

3.1.2.6 Open Ocean and Land/Ocean Boundary Masking

An ice concentration map of the Antarctic with an ocean mask applied was first presented by Comiso et al. (1984). The mask was based on the distribution of data points in the open ocean in the scatter plots of 18 GHz data against 37 GHz data. The open ocean clusters were linear with a positive slope. The ocean mask was designed so that any data points below a line paralleling the ocean cluster but two standard deviations higher were considered open ocean. This included areas with ice concentrations of 10 percent or lower. Areas with ice concentrations below 10 percent had the same signature as open water and are regarded as open water in the algorithm. While not perfect for SMMR, this mask is effective at removing a large fraction of bad data in the open ocean. Because the SSM/I carried the 19.4 GHz channel instead of the 18 GHz channel, the effectiveness of the mask became significantly reduced because 19.4 GHz is closer to the water vapor line and therefore more vulnerable to atmospheric effects. An additional mask that makes use of the difference between 19.4 and 22.2 GHz data as discussed in Comiso (1995) provided some improvements but the residuals were still worse than occurred for the SMMR data.

The 18.7 GHz channel for AMSR is at a frequency between those of SSMR and SSM/I. It is not obvious how effectively this channel could be used for open ocean masking but it will certainly be an improvement to SSM/I. An AMSR ocean mask will take advantage of experiences with SMMR and SSM/I but may also use water vapor and liquid water data extracted over the open ocean. Also, climatological temperatures from AVHRR will be utilized if necessary.

Because of side-lobe effects and sensor footprints greater than the grid size, ocean brightness temperatures in coastal regions are contaminated by land. As a consequence, ice concentrations of up to 40 percent may occur in such areas even in the absence of sea ice. To minimize the problem, a land/ocean boundary mask developed by Cho et al. (1996) for the Sea of Okhotsk was adopted and modified slightly for use in both hemispheres. This technique requires the inspection and modification of each pixel based on the characteristics of a surrounding 3 x 3 pixel matrix. If one pixel in the 3 x 3 matrix represents land while another represents open ocean, the mid-point of the matrix is set to an ocean value. The results from the use of a modified version of this technique is illustrated in Figure 34. In Figure 34a, ice concentration maps without any land/ocean mask is shown for the Sea of Okhotsk region. In Figure 34b, the same ice concentration map but with a masking applied. The masking provides a more accurate characterization of the sea ice cover and reduce the errors in trend analysis studies. The 85 GHz image shown in Figure 34c is consistent with the masking and provides a good validation of the procedure since it is less affected by sidelobe effects and has better resolution. Also, an infrared image from AVHRR, shown in Figure 34d, is basically in agreement with the masking as well.

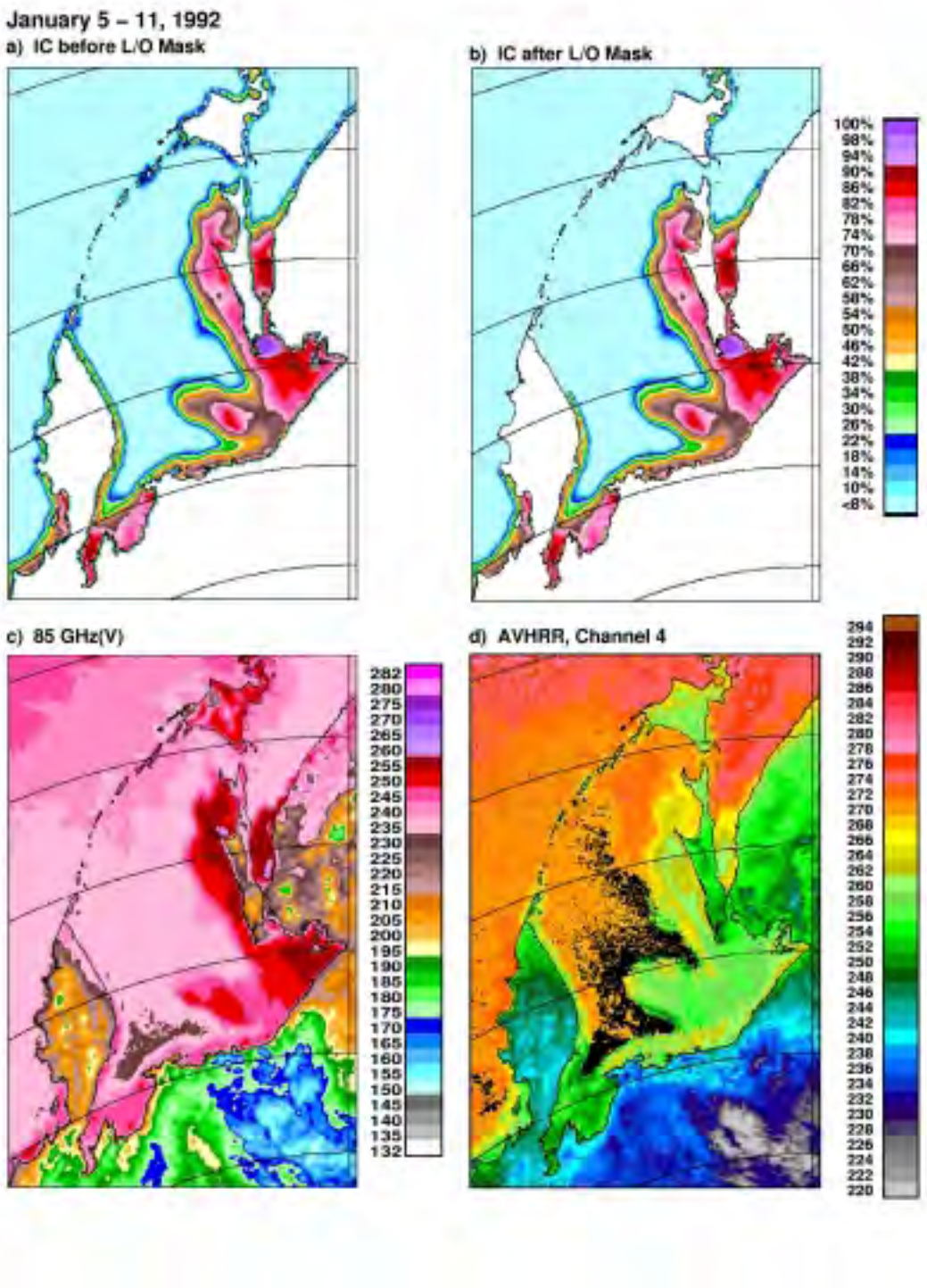

Figure 34. (a) Ice concentration map at the Sea of Okhotsk region without land/ocean boundary masking; (b) ice concentration map at the Sea of Okhotsk region with land/ocean boundary masking; (c) 85 GHz channel image at the Sea of Okhotsk; and (d) AVHRR infrared image at the Sea of Okhotsk.

Current techniques are not perfect and sometimes it takes some human intervention to convert SSM/I data to a more accurate data set. In Figure 35a, an Arctic ice map is presented showing some residual bad data in the open ocean after the ocean masking technique is applied and incorrect ice concentration values along land/ocean boundaries, such as the coasts of England and Spain. The black dots are data points not covered by the satellite when the SSM/I gridding system is applied. In Figure 35b, a land/ocean mask procedure was applied and the residual bad data in the open ocean were removed manually through computer interactive techniques. Also, the black dots were covered through spatial interpolation. With AMSR data, it is expected that a clean image like Figure 35b would be possible to generate in an unsupervised manner through the use of both an improved technique through the use of other AMSR channels (e.g., 6 GHz and 85 GHz data).

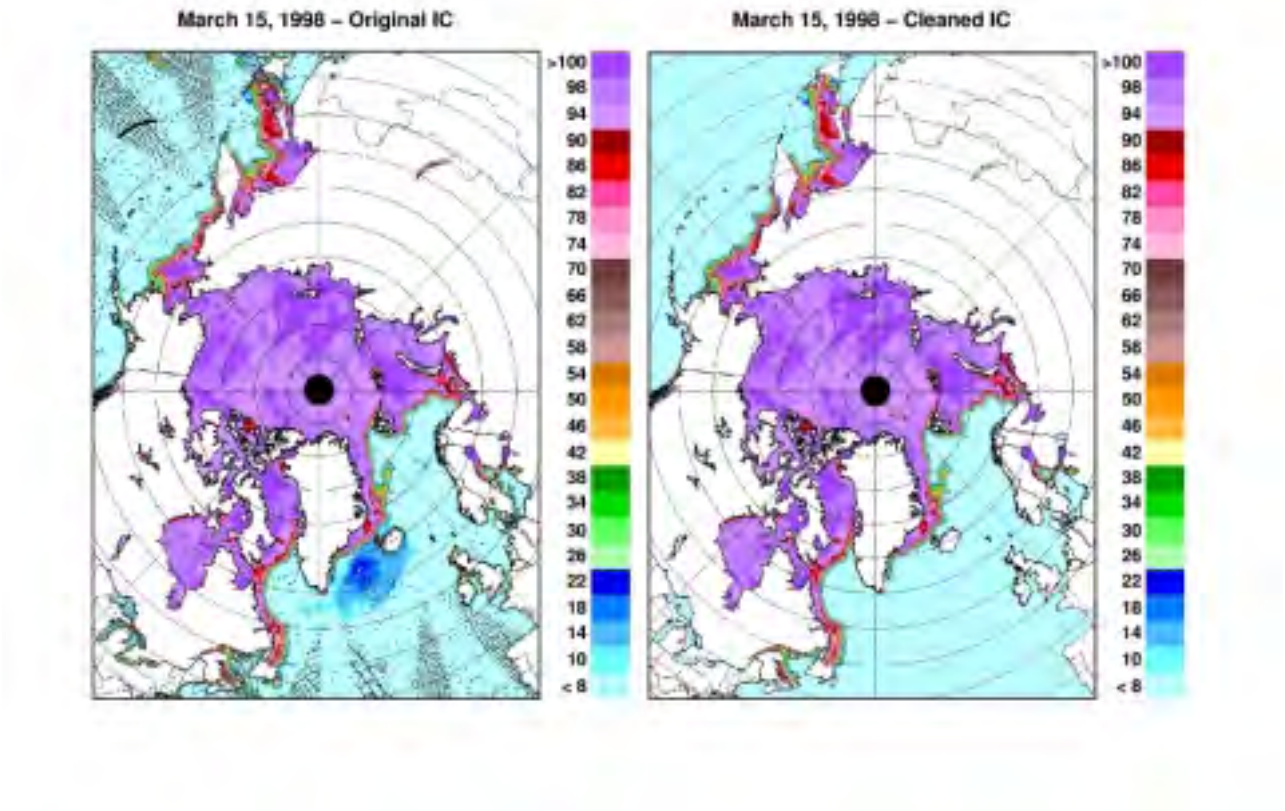

Figure 35. Daily ice concentration map of the entire Arctic (a) before masking is applied and (b) after masking is applied.

3.2 Sea ice temperature

3.2.1 Technique

Equation 10 provides the basis for calculating the temperature of the emitting surface. The technique used for calculating physical temperature from SMMR is similar in concept but quite

different in implementation to what was done by Gloersen et al (1992). In the current algorithm, the input for ice concentration is derived from a combination of 6 GHz data and 37 GHz data at vertical polarization. This enables a more accurate estimate of emissivity at the 6 GHz resolution at the first iteration which in turn is utilized to estimate the initial determination of surface temperature. Furthermore, with the iterative technique, the derived temperature map from ABA matches the resolution of the derived ice concentration product. Also, in Gloersen et al (1992) large areas of the Antarctic were discarded because the derived ice temperatures within the pack exceeded a threshold of 271K whereas with ABA, no data was discarded.

Ice surface temperature maps created using ABA and SMMR data for the Antarctic have already been shown previously. For completeness, surface temperature maps in the Arctic derived for data on January 6, 1979 are presented in Figures 36a and 36b for the values at initial and final iterations, respectively. Again, the maps are coherent with expected spatial distributions, with the coldest temperatures in areas north of Greenland and relatively warmer temperatures at the pheripheral seas. Using the ice concentration product, the surface temperatures inferred within the ice pack can be further converted into surface temperature of only the ice covered areas in each pixel through the use of the ice concentration result and the equation:

$$T_S = (T_P - 271(1-C_I)]/C_I \qquad (15)$$

where T_P and T_S are as defined previously. The monitoring of this ice temperature is important by itself but they may also provide useful information about a changing ice or snow thickness.

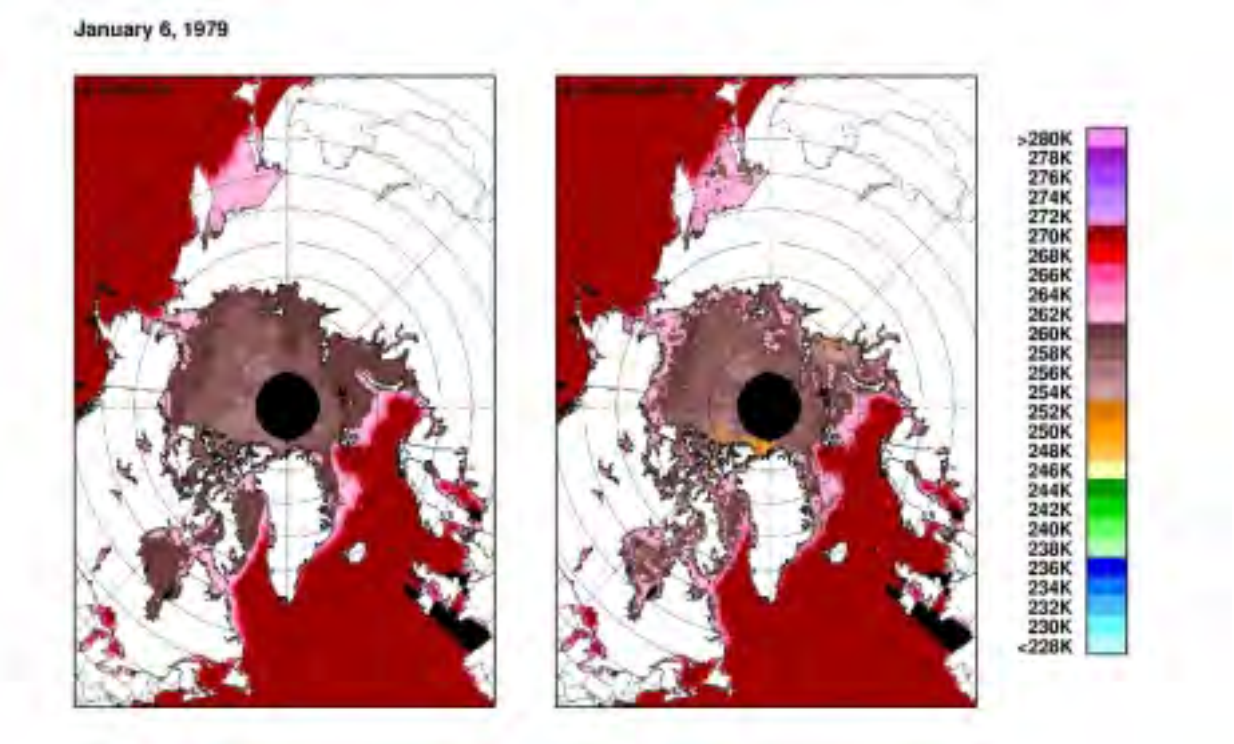

Figure 36. Surface ice temperature maps of the Arctic derived from SMMR (a) during initial iteration and (b) final iteration.

3.2.2 Validation Studies and Uncertainty Estimates

The validation of surface temperature data products will be done primarily with the use of temperatures derived from satellite infrared data (Comiso, 2000). The availability of coincident MODIS data on board AGUA will be most suitable for the purpose and will provide an excellent opportunity to better understand what the temperatures inferred from AMSR really represent. The infrared data provide skin depth surface temperature of the sea ice snow cover or the sea ice surface if a snow cover does not exist. Currently, the regression result from a comparative analysis of field measurements of both skin temperature and snow ice interface temperatures is used for transforming infrared data to snow ice temperature data. Because the regression result was derived from data during one cruise conducted during a particular time of the year, this result may have some bias, especially in other areas, when used globally and for all seasons. Additional field measurements need to be made or analyzed (if they already exist) to better understand spatial and temporal variability of such tranformation equation. Such measurement should also be done over the multiyear ice regions in the Arctic where the temperature retrieved from the 6 GHz data are expected to come from a thicker ice layer. The point measurements will be complemented by a modeling effort that would make use of available in situ data and a time series of surface temperature data derived from infrared systems. Buoy measurements of ice temperatures, which are available in some places of the Arctic and the Antarctic, will also be used for validation and to study the temporal changes of this temperature during the year.

3.3 Snow depth on sea ice

Temporally coincident in situ snow depth and SSMI measurements have been used to derive a relationship between snow depth and SSMI radiances. The specific data sets used in the analysis are given in Markus and Cavalieri [1998]. As we are only interested in changes in brightness temperature resulting from changes in snow cover on sea ice and not changes in sea ice concentration, we first correct the observed brightness temperatures for ice concentration variations. The measured brightness temperature at frequency n and polarization p, TB(n,p), consists of a linear mix of brightness temperatures for open water, $TB_W(n,p)$, and sea ice, $TB_I(n,p)$:

$$TB(n,p) = TB_I(n,p)\, C + TB_W(n,p)\, (1-C) \qquad (16)$$

where C is the ice concentration. The value of C is computed using the revised NASA Team algorithm. The open water brightness temperature TB_W is an average value from the open ocean regions for each channel and is assumed to be constant. From this equation TB_I is calculated and used later in the snow algorithm.

The in situ data represent a wide range of regions and seasons in the Antarctic. Although each in situ data point is an average of up to 600 individual measurements, the areal coverage of these surface measurements is still small compared to the area for a single SSMI pixel, about 625 km^2. Different combinations of TB_I were tried in the regression. The best correlation (0.6) is found using the spectral gradient ratio GR(37V/19V) (see Figure 37). The use of GR(37H/19H) gave similar results, but as the horizontal channels are known to be sensitive to layering [Matzler et al., 1984], the vertical polarization channels are used in the algorithm.

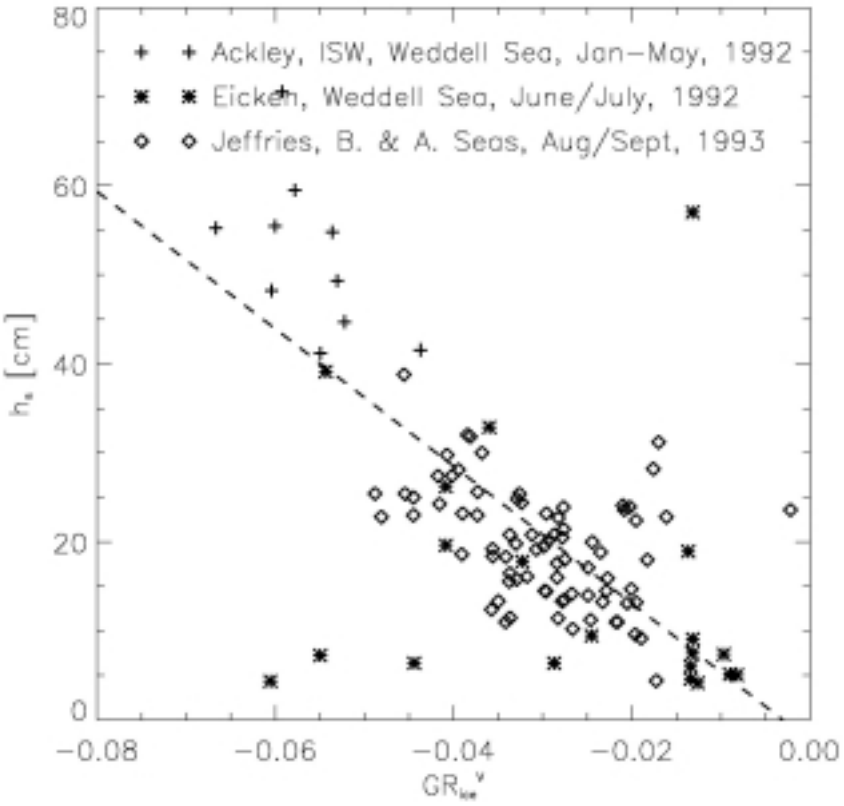

Figure 37. Scatterplot of GR(37V/19V) (corrected for ice concentration) vs in situ snow depth. The different symbols indicate different sources of in situ data. The line represents the linear regression fit (after Markus and Cavalieri, 1998).

Both, the correlation coefficient and the standard deviation of the linear fits are quite sensitive to single outliers. By removing the the three pixels in the lower left and the one pixel in the upper right shown in Figure 37, the correlation coefficient increases to -0.77 with a standard deviation of 7.8 cm. The exclusion of these outliers did not significantly affect the linear regression fit. Using all the data then, the regression of GR against in situ snow depth leads to

$$hs = -2.34 - 771\,(TB_I(37V)-TB_I(19V))/(TB_I(37V)+TB_I(19V)) \qquad (17)$$

where hs is the snow depth in cm.

Although surface and aircraft observations suggest that the 85 GHz data may be useful for developing a snow depth algorithm [Grenfell, 1986; Cavalieri et al., 1986; Comiso et al., 1989], our analysis did not show a significant correlation between these channels and in situ snow depth. This results in part from the shallow penetration of a few centimeters at this frequency. Nonetheless, 85 GHz data may serve as an indicator of the presence of snow even though an accurate estimate of snow depth can not be obtained.

Temporal information is included in the algorithm to identify wet snow or melt-refreeze events which result in large snow depth retrieval errors. Passive microwave algorithms for snow on land misinterpret wet snow areas as snow-free as a result of the blackbody behavior of a wet snow pack, meaning that the brightness temperature difference between 19 and 37 GHz will be very small and the derived snow depth value will be close to zero. Wet snow may also refreeze during the night which results in a frozen crust at the top of the snow layer. This results in very large grain sizes [Colbeck, 1982]. The emissivity decreases (more with increasing frequency) because of enhanced scattering within this layer [Onstott et al., 1987; Matzler, 1994]. Reduced emission at 37 GHz relative to 19 GHz results in a decrease in GR and thus would lead to an overestimate of snow depth. Cyclical wettening and subsequent refreezing of the snow mass can occur at all times in the Antarctic, even in winter particularly in the marginal ice zone [Massom et al., 1997; Sturm et al., 1998]. These events can be identified by large variations in brightness temperatures [Stiles and Ulaby, 1980; Cavalieri et al., 1991; Wankiewicz, 1993]. We therefore, flag pixels where the daily

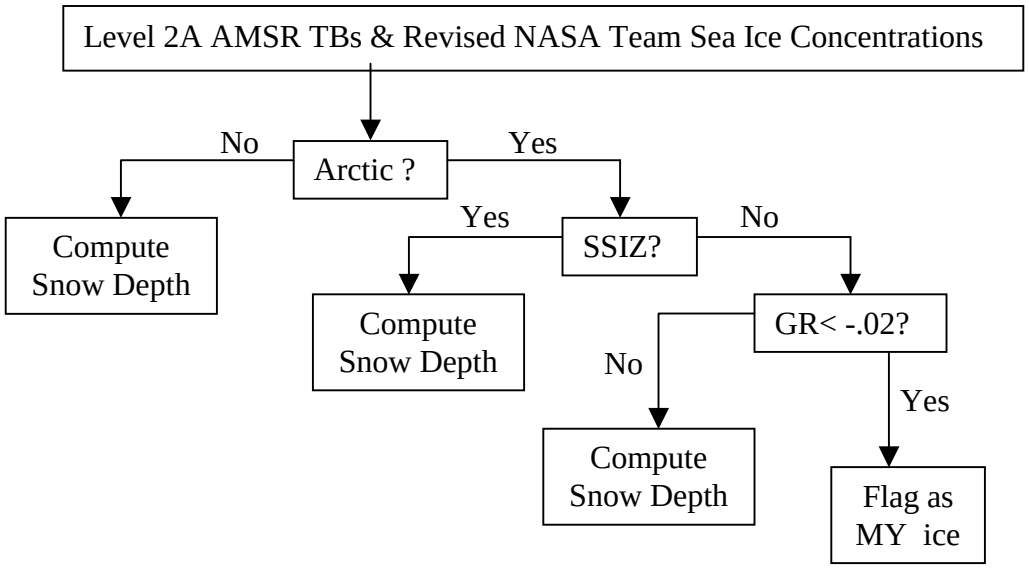

Figure 38. Snow Depth on Sea Ice Algorithm.

variations are above 5 cm d^{-1} over a five-day period. Comparison with detailed snow measurements for September 1989 in the Weddell Sea show that such events are effectively flagged by this procedure. A schematic diagram of the snow depth algorithm is provided in Figure 38.

The large-scale monthly snow depth distributions derived using this algorithm are compared with results from twelve Antarctic cruises covering most months and regions. Figure 39 shows monthly-averaged snow depth maps for the period 1988 through 1994. The segments in this Figure indicate regions where in situ snow depth distributions were available for validation. The snow depth distributions are in reasonable qualitative agreement. Average in situ snow depths, which range from 6.4 cm to 26.2 cm, and SSMI-derived snow depths, which range from 5.7 cm to 23.3 cm, correlate with a coefficient of 0.81. On average, the SSMI snow depths are 3.5 cm are lower than the in situ values. There are primarily two reasons why this negative bias is expected. First, high in situ snow depths are smoothed by the large SSMI footprint (monthly averages further increase this smoothing). Second, during most cruises, the ship passes the marginal ice zone twice

and makes the majority of measurements in the interior ice, whereas the SSMI segments include the whole marginal ice zone where most of the thinner snow cover is expected.

In the Arctic, the retrieval of snow depth is complicated by the presence of multiyear ice which has a signature similar to snow cover on first-year ice. Both, multiyear ice and deep snow on first-year ice result in more negative values for GR. Until we are able to discriminate between variations in multiyear ice and variations in snow depth, snow depth will only be retrieved in the seasonal sea ice zones and in regions where the value of GR(37V/19V) is greater than -0.02. This threshold corresponds to multiyear ice concentration of less than 20% (false indications of multiyear ice of up to 20% have been observed in the seasonal sea ice zones). Where GR(37V/19V) is less than -0.02, the image pixels will be flagged as multiyear ice (see Figure 39). Detailed validation of snow depth retrieval in the Arctic has still to be carried out. Nevertheless, average snow depths for February in the Bering Sea (1 to 10 cm) are in good agreement with measurements from the Bering Sea Experiment in 1973 (snow depths between 1 and 8 cm) (Gloersen et al., 1975). Further validation studies will be undertaken in as many areas as we have independent snow-depth measurements.

The study of the temporal development of the snow cover suggests a retrieval precision of about 3 cm. To increase the precision, the final product will be 5-day average snow depth maps which is consistent with the standard product of snow depth on land for the EOS Aqua mission.

Input parameters to the snow-depth algorithm are the 19 GHz and 37 GHz brightness temperatures both at vertical polarization and the ice concentration. The largest error source in ice concentration retrievals is the presence of new and young ice types. These ice types are interpreted by the algorithm as a mixture of open water and consolidated first-year ice. Ice concentration is underestimated if there is a significant amount of new and young ice within a footprint. This problem has been corrected to a large extent through the application of the thin ice modification of the revised NASA Team algorithm (section 3.1.1.3) to be used in the Bering Sea and the Sea of Okhotsk. In areas of the Antarctic, the problem remains. The sensitivity of the snow depth retrievals to ice concentration variability was investigated as follows. We took a sample data set of brightness temperatures from actual observations and introduced an ice concentration error at different ice concentrations ranging from 20% to 100%. Except for ice concentrations less than 20%, the sensitivity is at or below 1 cm/% with a minimum at 50%. Overestimates in ice concentration result in underestimates in snow depth and vice versa. Because of the higher sensitivity at concentrations less than 20%, we limit the snow depth retrievals to ice concentrations between 20% and 100%. Ice concentrations less than 20% appear almost exclusively near the ice edge.

Gloersen and Campbell [1988] have observed in airborne observations, and Maslanik [1992] has shown in a theoretical study of weather effects on ice concentration retrievals, that at higher ice concentrations weather effects increase GR whereas PR is less affected. This increase in GR will also be reflected as an underestimate of snow depth. A quantitative estimate of this error needs to be computed.

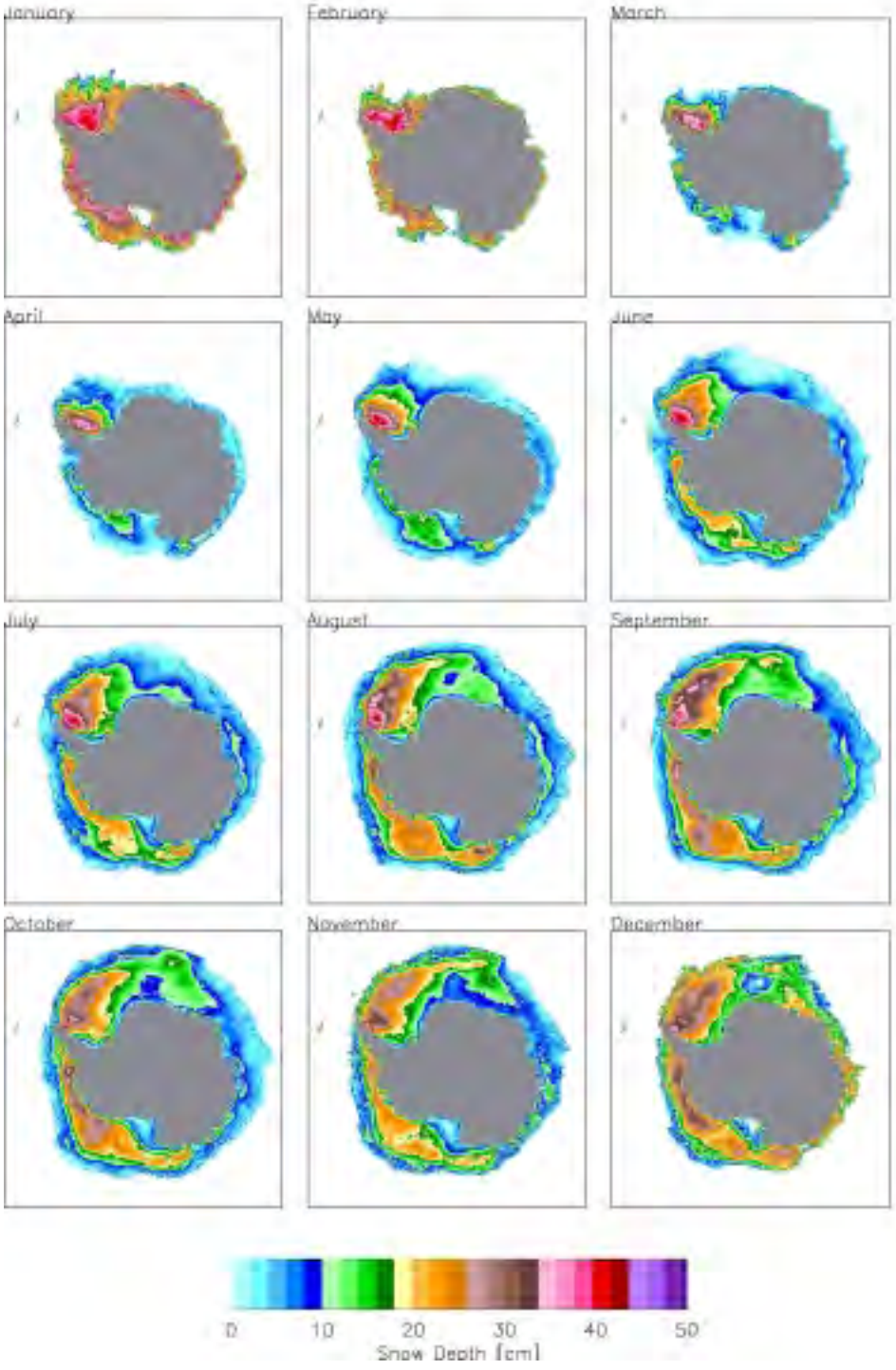

Figure 39. Mean monthly snow depths from the year 1988-1994. The open ocean area is white. Black pixels indicate where more than 3 years of monthly averages have flagged values resulting from meltings effects identified using temporal information.

Grain size variability affects the brightness temperatures and leads to errors in the calculation of snow depth. Larger grain sizes result in enhanced scattering and therefore in decreased brightness temperatures. Because this effect is greater at 37 GHz than at 19 GHz [Chang et al., 1976], larger grain sizes will result in overestimates of snow depth. Grain size generally increases after deposition at the surface. Temperature and humidity gradients within the snow cover result in the development of surface or depth hoar. Another mechanism which results in an increase of grain size is the refreezing of wet snow. Armstrong et al. [1993] have shown from measurements over land that the grain size effect is lower than what has been found from theoretical calculations [Chang et al., 1976]. The grain size effect is further reduced with satellite observations because extreme grain size effects will average out. This is indirectly supported by the good agreement between in situ and SSMI-derived snow depth distributions as shown earlier. As grain sizes are not routinely obtained during the cruises in the Southern Ocean, investigation of how the grain size distribution of snow on sea ice affects our results could not be carried out. In situ grain size measurements require a considerably greater effort than the measurement of snow depths.

4.0 Practical Considerations

4.1 Numerical computation considerations

The original NASA Team and Bootstrap algorithms have been run without problems at the National Snow and Ice Data Center DAAC for routine processing. The NASA Team algorithm has also been run at the Marshall DAAC for processing the SSMI Pathfinder Data Set. The Bootstrap Algorithm has also been tested by the Japanese NASDA/Earth Observation Research Center where ice concentration data from AMSR-E and ADEOS AMSR will be archived. Given this history, we do not anticipate any computational problems with the revised AMSR-E sea ice algorithms. Each of the revised algorithms are currently running on SGI workstations at Goddard; the combined AMSR-E sea ice algorithm is being tested on the processor at MSFC. Even daily Level 3 products will not pose a problem.

4.2 Programming/procedural considerations

Input to the combined AMSR-E sea ice algorithms will consist of Level 2A AMSR-E brightness temperatures, latitude, longitude, time and a land/ocean flag. The standard output sea ice products will consist of sea ice concentration, sea ice temperature and snow depth and will include latitude, longitude, and a time stamp. The computer code and documentation will be delivered to the Marshall Space Flight Center for processing the standard products. The algorithms are coded in C.

4.3 Quality control and diagnostics

Quality control of brightness temperatures will be done during the generation of the Level 2A products. The first step in the quality control of the sea ice products will consist of checking whether or not the retrieved sea ice products fall within reasonable limits. Diagnostics will be based in part on satellite sea ice climatology developed since the launch of the Nimbus 7 SMMR in 1978. These data will provide a useful measure of the seasonal and regional values for sea ice

concentration and to some extent sea ice temperature. Quality control of snow depth will be more difficult, because very little data exist on the spatial scale of AMSR-E footprints.

4.4 Exception handling

Exception handling will consist of flagging missing data, land, and unreasonable retrievals. Missing brightness temperatures will result in setting a missing flag for the sea ice retrieval. The sea ice algorithm will not be run over land. It is presumed that out-of-range brightness temperatures will be handled in the generation of Level 2A products. Out-of-range retrievals will be handled within the algorithm. Diagnostics for checking out-of-range data will be used in the algorithms to determine whether the output should be flagged as unreasonable. In some cases, for example, sea ice concentrations greater than 100% will be set to 100% and sea ice concentrations less than 0 will be set to zero. Much larger discrepancies will be flagged as unreasonable.

5.0 Validation Program

The objectives of the validation program are: (1) to obtain a quantitative measure of the accuracy of the AMSR-E-derived sea ice products; (2) to define problem areas or areas that need improvements; and (3) to provide a means to evaluate how well each of the three standard sea ice products meets the observational requirements specified by the EOS Science Plan (1999). The main emphasis will be the validation of the sea ice concentration products not only because of its relevance to the MTPE, as indicated earlier, but also because success in deriving the other two standard products depends on the accuracy of this parameter. Sea ice temperature and snow depth on sea ice are relatively new products that require substantial validation. Emphasis will be placed on those regions, seasons, and conditions that are major sources of error. For example, summer melt is the largest single source of error in Arctic sea ice concentration retrievals.

The initial phase of the validation program, which is currently being implemented, is to take advantage of existing historical data. For example, the excellent year-long data set including show thickness and temperature profile statistics from SHEBA experiment which ran from Oct. 1997 to Oct. 1998 will be utilized. During this time period, an ER-2 aircraft with passive microwave sensors and a MODIS simulator on board flew over several tracks in the Arctic including the SHEBA ice camp. This data is currently being analyzed. Field experiments in both Arctic and Antarctic regions have been undertaken since the launch of the Nimbus-7 SMMR and new experiments are being planned for the AMSR.

We will take advantage of data from these programs to validate, whenever possible, results from the final version of the algorithms. Historical high resolution satellite data (Landsat, SPOT, MOS, etc.) will be used to extrapolate values from point measurements. Historical passive microwave data (SMMR, SSMI) and also TMI, and Adeos-2 AMSR will be used to test the algorithms before the launch of AMSR-E. . Furthermore, radiative transfer modeling results will be used to improve our understanding of the physics of the emission from sea ice and the effect of the intervening atmosphere. Such information is needed to assess limits in the accuracy of some of the products.

To be able to optimize the performance of the algorithms and assess the accuracy of the sea ice products both pre- and post-launch aircraft missions will be conducted and coordinated with surface measurements whenever possible. A suite of microwave radiometers that measure radiances at frequencies and polarizations close to those planned for AMSR-E will be used including the NOAA/ETL Polarimetric Scanning Radiometers (PSR-A; PSR-C) that have been flown on both the NASA DC-8 and P-3. In addition, NASDA has an airborne AMSR simulator called the Airborne Microwave Radiometer (AMR) will be used when available. Aircraft AMSR-E simulators will be complemented by an infrared system to measure surface temperature, the polarimetric SAR (if available) to help discriminate surface types, especially in the perennial ice regions, and a digital cameras to evaluate surface properties and overall characteristics of the ice cover. The specific areas and times covered would include those where and when the revised NASA Team and the revised Bootstrap algorithms have significant differences. In addition, data is needed to improve ice-weather discrimination at the ice edge and in marginal ice zones. Such missions will be coordinated with validation programs for other AMSR-E parameters. The timing of the aircraft underflights will also be such that accurate comparative analysis with data from SSMI, TRMM TMI, Landsat 7, as well as AMSR-E instruments is possible. When and wherever possible the aircraft underflights will be coordinated with ongoing or planned surface programs to leverage additional information for the validation of the standard products. An example of this would be surface measurements of snow depth and ice temperature.

A NASA sea ice validation program for the DMSP SSMI was completed in 1991 and may be used as a guide for the sea ice data validation plan for the AMSR-E (Cavalieri, 1992; Cavalieri, 1991; Cavalieri et al., 1991; Steffen and Schweiger, 1991). Other validation programs completed include a near simultaneous aircraft, submarine, and ship experiment over the Arctic (Comiso et al., 1991; Wadhams et al., 1992) and several cruises in the Antarctic (Comiso et al., 1989; Grenfell et al., 1994). Many major compaigns in the Arctic regions have also been undertaken (e.g., MIZEX east and west). Results from sea ice validation studies since the launch of the Nimbus 7 SMMR has been summarized (Cavalieri, 1992). We will take advantage of experiences from these programs to optimize the likelihood of success in the new validation missions. Data from the aircraft missions will be supplemented by data from Landsat 7, which has become a NASA system again and will be less expensive, and other high resolution satellite systems. Landsat 7 and other systems will enable extrapolation of data obtained from the aircraft tracks to much wider area. The launch of the 40 channel MODIS system aboard EOS Terra will also open an oportunity to investigate new information about the ice cover that can be derived from such a system. Since MODIS will also be available aboard EOS Aqua, the data will be used synergistically with AMSR-E data to optimize the accuracy of products derived from the latter. The uses of Radarsat (and other satellite SAR data) and NSCAT (and other scatterometers) data for ice applications have not been well established but SAR is expected to be provide some critical information needed to verify ice type discrimination results while SAR, NSCAT, and MODIS will be useful for surface type classification. A list of the standard products and a summary of data to be used to validate each of them is given in Table 9. The list provides examples of systems that would be most suitable for validating the different parameters.

TABLE 9. Validation data sets for the proposed AMSR-E sea ice products.

Standard Products	Validation Data
Sea Ice Extent and Concentration	Landsat 7; RADARSAT; MODIS; ADEOS - II Gobal Imager (GLI); NOAA AVHRR; aircraft underflights.
Sea Ice Temperature	ADEOS - II GLI; EOS Terra MODIS; AVHRR; climatology; buoys; field and ice station data; aircraft underflights
Snow Depth on Sea Ice	In situ snow depth measurements; remotely-sensed snow depth from aircraft.

TABLE 10. Planned schedule of aircraft campaigns for sea ice validation.

Arctic Summer	**June/July 2000**
Aircraft:	NAVY (NAWC) P-3
Objectives:	To estimate the errors incurred by the standard AMSR-E sea ice algorithms resulting from the melt ponds; develop a capability to map melt ponds.
Instruments:	NOAA PSR-A, PSR-C, L-band radiometers, GPS, IR radiometer, aerial cameras.
Arctic Winter	**March 2002**
Aircraft:	NASA Wallops P-3
Objectives:	To validate sea ice concentration and temperature algorithms by underflying the ADEOS-II and EOS-Aqua AMSR sensors
Instruments:	NOAA PSR-A, PSR-C, GPS, nadir-viewing IR radiometer, aerial cameras.
Antarctic Winter	**August 2002**
Aircraft:	NASA Wallops P-3
Objectives:	To validate sea ice concentration and temperature algorithms by underflying the EOS-Aqua AMSR-E.
Instruments:	NOAA PSR-A, PSR-C, GPS, nadir-viewing IR radiometer, aerial cameras.
Antarctic Winter	**September/October 2003**
Aircraft:	NASA Wallops P-3
Objective:	To validate sea ice concentration, snow and temperature algorithms by underflying the ADEOS-II and EOS-PM AMSR sensors
Instruments:	NOAA PSR, GPS, nadir-viewing IR radiometer, aerial cameras.
Arctic Winter	**March 2004**
Aircraft:	Wallops P-3 or UAV
Objective:	To validate snow depth algorithm by underflying the ADEOS-II and EOS-Aqua AMSR sensors
Instruments:	PSR-A, PSR-C, range-gated, step frequency radar, IR radiometer, aerial cameras.

A comprehensive discussion of the validation strategies including specific objectives and implementation details can be found in the EOS-Aqua AMSR-E validation document. Our planned aircraft campaigns are listed in Table 10. As of this writing the field portion of the first aircraft campaign, Meltpond2000, has been completed. Data analysis is underway including an intercomparison of aircraft PSR, DMSP SSMI, Landsat 7, and MODIS data sets (Figure 40). Two of the Navy P-3 flights were coordinated with a Canadian surface meltpond experiment called C-ICE 2000. Canadian scientists, at their ice camp near Resolute, made a series of surface measurements including melt pond temperature and salinity, air temperature, relative humidity, wind speed, incident and reflected radiation. This combined surface/aircraft/satellite data set is expected to provide the comprehensive characterization of the surface and atmosphere needed to meet the validation objectives.

For the planned Arctic campaign in March 2002, we will coordinate aircraft flights with surface measurements made by scientists on the USCG ship Healy as part of the NSF funded Shelf Basin Interaction Project. At the time of the aircraft overflights, measurements including snow depth, ice thickness, snow grain size, density, and wetness. In addition, meteorological measurements will also be made including near-surface air temperature and wind speed. We also plan to coordinate with measurements made at the DOE ARM site in Alaska and with another NSF funded (Office of Polar Programs Long Term Observations) effort to use a UAV for sea ice mapping and atmospheric sounding. The plan here is to fly patterns both above and below cloud cover to determine the atmospheric contribution to sea ice retrievals. For the Arctic 2004 aircraft campaign, we plan to identify planned Arctic surface programs similar to those in 2002 to supplement the measurements made by aircraft and satellite.

The Antarctic compaign in August 2002 will be based in Punta Arenas, Chile and will include overflights over the Weddell Sea and the Bellingshaussen/Amundsen Seas. The principal areas of interest are the marginal ice zone, the coastal polynya areas, and the midsection of the pack, where large discrepancies between the two algorithms were previously reported. In the marginal ice zone and coastal polynyas, the ability of the algorithms to identify the true location of the ice edge and the coastal boundaries will be tested. Also, the effect of new ice in the coastal polynya areas and small pancakes at the ice edges on the accuracy of the retrieved product will be examined. Two ships will also be in the pack during this time period and scientists will be making surface measurements of various physical and radiative properties of the ice cover for comparative analysis with aircraft and satellite measurements.

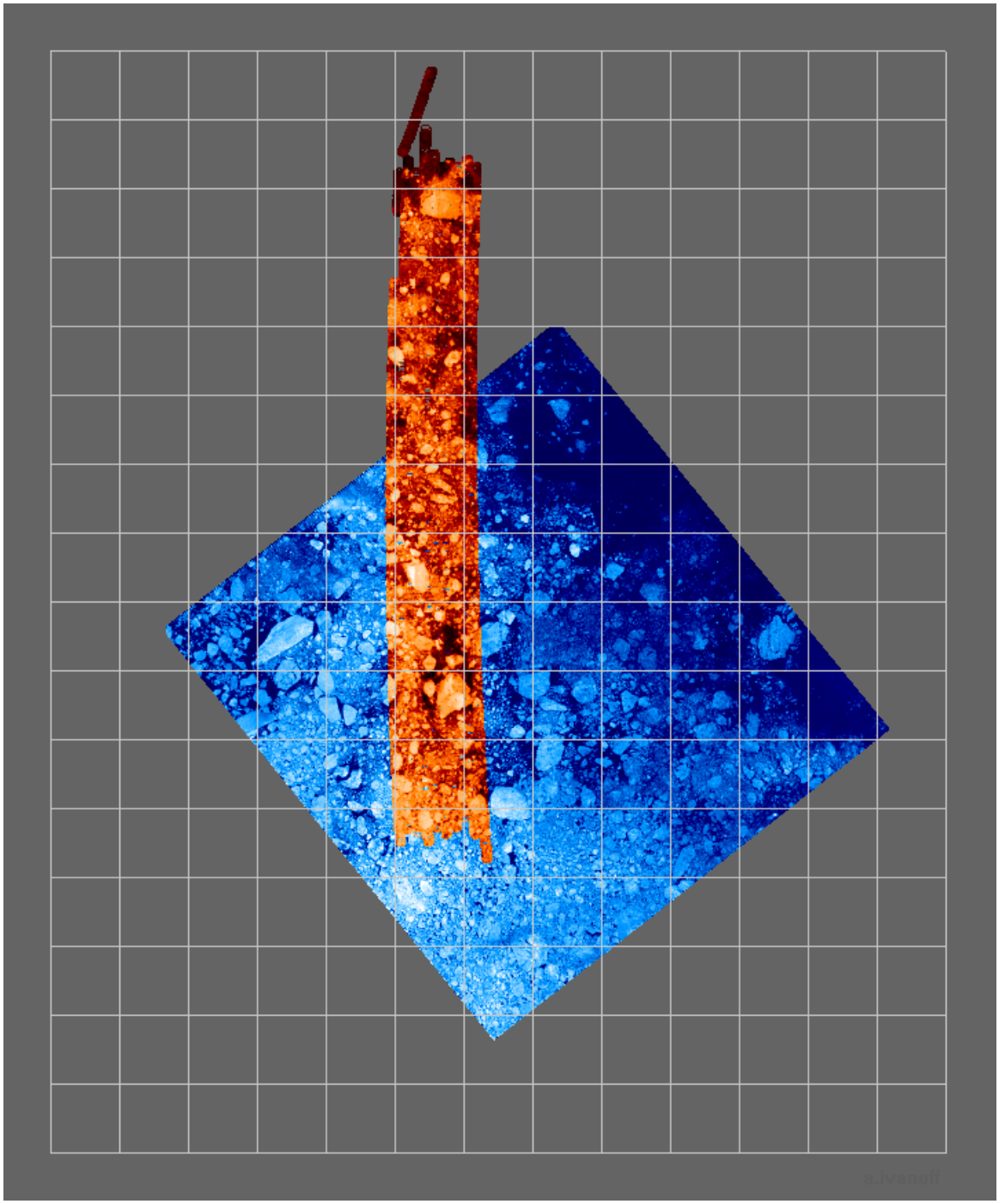

Figure 40. Meltpond2000 PSR-A brightness temperatures (19 GHz, V-pol.) gridded at a resolution of 0.5 km (red) over a Landsat 7 ETM+ image (blue) with a 25-km DMSP SSMI grid shown (white) all for June 27.

6.0 References

Aagaard, K., L. K. Coachman, and E. C.mack, On the halocline of the Arctic ocean, *Deep Sea Res*., 28, 529-545, 1981.

Armstrong, R.L., A. Chang, A. Rango, and E. Josberger, Snow depths and grain-size relationships with relevance for passive microwave studies, Ann. Glaciol, 17, 171-176, 1993.

Badgley, F. I., Heat budget at the surface of the Arctic Ocean, in Proc. of the Symp. on the Arctic Heat Budget and Atmospheric Circulation, J. O. Fletcher, ed., pp. 267-277, 1966.

Bromwich, D.H., T.R. Parish, and C.A. Zorman, The confluence Zone of the intese katabatic winds at the Terra Nova Bay, Antarctica, as derived from airborne sastrugi surves and mesoscal numerical modeling, J. Geophys. res., 95(D5), 5495-5509, 1990.

Budyko, M.I., Polar ice and climate, In Proceedings of the Symposium of the Arctic Hea Budget and Atmospheric Circulation, ed. by J.O. fletcher (ed), RM5233-NSF, Rand Corporation, Santa Monica, CA, 3-21, 1966.

Businger, S., and R. J. Reed, Polar lows, in Polar and Arctic Lows, Twitchell, P. F., E. A. Rasmussen, and K. L. Davidson, eds., A. Deepak, Hampton, VA, pp. 3-45, 1989.

Carleton, A. M., Satellite climatological aspects of the "polar low" and "instant occlusion," Tellus 37A, 433-450, 1985.

Cavalieri, D. J., NASA Sea Ice Validation Program for the Defense Meteorological Satellite Program Special Sensor Microwave Imager, J. Geophys. Res., 96, 21,969-21,970, 1991.

Cavalieri, D. J., The Validation of Geophysical Products Using Multisensor Data, Chapter 11, Microwave Remote Sensing of Sea Ice, (ed. by Frank Carsey), American Geophysical Union, Washington, D.C., 243-259, 1992.

Cavalieri, D. J., P. Gloersen, and T. T. Wilheit, Aircraft and satellite passive-microwave observations of the Bering Sea ice cover during MIZEX West, IEEE *Trans. Geoscience and Remote Sensing* GE-24, 368-377, 1986.

Cavalieri, D. J., J. Crawford, M. Drinkwater, W. J. Emery, D. T. Eppler, L. D. Farmer, M. Goodberlet, R. Jentz, A. Milman, C. Swift, C. Wackerman, and R. L. Weaver, NASA sea ice validation program for the DMSP SSMI: Final report, NASA TM 104559, pp. 126, 1992.

Cavalieri, D., A passive microwave technique for mapping new and young sea ice in seasonal sea ice zones, J. Geophys. Res., 99(C6), 12561-12572, 1994.

Cavalieri, D. J., P. Gloersen, and W. J. Campbell, Determination of sea ice parameters with the Nimbus 7 SMMR, J. Geophys. Res., 89, 5355-5369, 1984.

Cavalieri, D. J., P. Gloersen, C. L. Parkinson, J. C. Comiso, and H. J. Zwally, Observed hemispheric asymmetry in global sea ice changes, SCIENCE, 278,1104-1106, 1997.

Cavalieri, D. J., K. M. St. Germain, and C. T. Swift, Reduction of weather effects in the calculation of sea ice concentration with the DMSP SSMI, J.Glaciology, 41(139), 455-464, 1995.

Cavalieri, D. J., J. P. Crawford, M. R. Drinkwater, D. T. Eppler, L. D. Farmer, R. R. Jentz, C. C. Wackerman, Aircraft active and passive microwave validations of sea ice concentration from the DMSP SSMI, J. Geophys. Res., 96, 21989-22008, 1991.

Cavalieri, D. J., and S. Martin, The contribution of Alaskan, Siberian, and Canadian coastal polynyas to the cold halocline layer of the Arctic Ocean, *J. Geophys. Res*., 18,343-18,362, 1994.

Chang, T. C., P. Gloersen, T. Schmugge, T. T. Wilheit, and H. J. Zwally, Microwave emission from snow and glacier ice, J. Glaciol. 16, 23-39, 1976.

Cho, K., N. Sasaki, H. Shimoda, T. Sakata and F. Nishio, Evaluation and improvement of SSM/I sea ice concentration algorithms for the Sea of Okhotsk, *J. Remote Sensing of Japan, 16*(2), 47-58, 1996.
Colbeck, S.C., An overview of seasonal snow metamorphism, Rev. Geophys. Space Phys., 20, 45-61, 1982.
Comiso, J. C., Sea ice effective microwave emissivities from satellite passive microwave and infrared observations, J. Geophys. Res., 88, 7686-7704, 1983.
Comiso, J. C., Characteristics of Arctic Winter Sea Ice from Satellite Multispectral Micrwave Observations, J. Geophys. Res., 91, 975-994, 1986.
Comiso, J.C., SSMI ice concentrations using the Bootstrap Algorithm, NASA RP 1380, 50pp, 1995.
Comiso, J.C., Variability and trends in Antarctic surface temperatures from in situ and satellite infrared measurements, *J. Climate*, 13, 1674-1696, 2000.
Comiso, J.C., P. Wadhams, L.T. Pedersen, and R. Gersten, The seasonal and interannual variability of the Odden and a study of environmental effects, *J. Geophys. Res.* (In press, 2001).
Comiso, J.C., and R. Kwok, The summer Arctic sea ice cover from satellite observations, J. *Geophys. Res.*,101(C2), 28397-28416, 1996.
Comiso, J.C., and A.L. Gordon, Interannual variabilities of summer ice minimum, coastal polynyas, and bottom water formation in the Weddell Sea, in Antarctic sea ice physical properties and processes, *AGU Antarctic Research Series Volume*, edited by M. Jeffries, 293-315, 1998.
Comiso, J. C., and H. J. Zwally, Antarctic Sea Ice Concentrations Inferred from Nimbus-5 ESMR and LANDSAT imagery, *J. Geophys. Res., 87*(C8), 5836-5844, 1982.
Comiso, J.C., and H.J. Zwally, Temperature Corrected Bootstrap Algorithm, IEEE IGARSS'97 Digest, Volume 3, 857-861, 1997.
Comiso, J. C., D. J. Cavalieri, C. P. Parkinson, and P. Gloersen, Passive Microwave Algorithms for Sea Ice Concentration - A Comparison of Two Techniques, *Remote Sens. Environ*., **60**, 357-384, 1997.
Comiso, J.C, T.C. Grenfell, M. Lange, A. Lohanick, R. Moore, and P. Wadhams, Microwave remote sensing of the Southern Ocean ice cover, Chapter 12, *Microwave Remote Sensing of Sea Ice*, (ed. by Frank Carsey), American Geophysical Union, Washington, D.C., 243-259, 1992.
Comiso, J. C. and C. W. Sullivan, Satellite Microwave and In Situ Observations of the Weddell Sea Ice Cover and its Marginal Ice Zone, *J. Geophys. Res*., 91(C8), 9663-9681, 1986.
Comiso, J. C., S. F. Ackley, and A. L. Gordon, Antarctic Sea Ice Microwave Signature and their Correlation with In Situ Ice Observations, J. Geophys. Res. 89(C1):662-672, 1984.
Comiso, J. C., T. C. Grenfell, D. Bell, M. A. Lange, and S. F. Ackley, Passive Microwave In Situ Observations of Winter Weddell Sea Ice, J. Geophy. Res., 94(C8), 10891-10905, 1989.
Comiso, J. C., P. Wadhams, W. Krabill, R. Swift, J. Crawford, and W. Tucker III, Top/Bottom multisensor remote sensing of Arctic sea ice, J. Geophy. Res., 96(C2), 2693-2711, 1991.
EOS Science Plan, M. D. King, Editor, NASA Goddard Space Flight Center, Code 900, Greenbelt, MD 20771-0001, 1999.
Fraser R.S., Gaut, N.E., Reifenstein, E.C., and H. Sievering, Interaction Mechanisms--Within the Atmosphere, in Manual of Remote Sensing, edited by R.G. Reeves, A. Anson, D. Landen, pp.181-233, American Society of Photogrammetry, Falls Church, VA, 1975.

Eppler, D.T., and 14 others, Passive microwave signatures of sea ice, in Microwave Remote Sensing of Ice, Geophys. Monogr. Ser., vol. 68, edited by F. Carsey, pp. 47-71, AGU, Washington, D.C., 1992.
Gloersen, P. and Barath, F. T., A Scanning Multichannel Microwave Radiometer for Nimbus-G and SeaSat-A, *IEEE Journal of Oceanic Engineering*, *OE-2*, 172-178, 1977.
Gloersen, P., and D. J. Cavalieri, Reduction of weather effects in the calculation of sea ice concentration from microwave radiances, J. Geophys. Res., 91(C3), 3913-3919, 1986.
Gloersen, P. and W. J. Campbell, Satellite and aircraft passive microwave observations during the Marginal Ice Zone Experiment in 1984, J. Geophys. Res. 93, 6837-6846, 1988.
Gloersen P., W. J. Campbell, D. J. Cavalieri, J. C. Comiso, C. L. Parkinson, H. J. Zwally, (1992), Arctic and Antarctic Sea Ice, 1978-1987: Satellite Passive Microwave Observations and Analysis, NASA Spec. Publ. 511, 1992.
Gloersen, P., C. L. Parkinson, D. J. Cavalieri, J. C. Comiso, and H. J. Zwally, Spatial Distribution of Trends and Seasonality in the Hemispheric Sea Ice Covers: 1978-1996, *J. Geophys. Res.*, 104, 20,827-20,836, 1999.
Gloersen, P., R.O. Ramseier, W.J. Campbell, T.C. Chang, and T.T. Wilheit, Variation of Ice Morphology of Selected Mesoscale Test Areas during the Bering Sea Experiment, in USSR/USA Bering Sea Experiment, edited by K.Y. Kondrat'ev, Gidrometeoizdat Publisher, Leningrad, 1975.
Gloersen, P., E. Mollo-Christensen, and P. Hubanks, Observations of Arctic polar lows with the Nimbus 7 Scanning Multichannel Microwave Radiometer, in Polar and Arctic Lows, P. F. Twitchell, E. A. Rasmussen, and K. L. Davidson, eds., A. Deepak, Hampton, Virginia, pp. 359-371, 1989.
Gloersen, P., T. C. Chang, T. T. Wilheit, and W. J. Campbell, Polar sea ice observations by means of microwave radiometry, in Advanced Concepts and Techniques in the Study of Snow and Ice, H. S. Santeford and J. L. Smith, eds., Nat. Acad. Sci, pp. 541-550, 1974.
Gordon, A., Deep Antarctic convection west of Maud Rise, J. *Phys. Oceanography*., 8, 600-612, 1978.
Gordon, A. L., and J. C. Comiso, Polynyas and the Southern Ocean, *Scientific American, 258,* 90-97, 1988.
Grenfell, T. C., A theoretical model of the optical properties of sea ice in the visible and near infrared, *J. Geophys. Res*., 88, 9723-9735, 1983.
Grenfell, T. C., Surface-based passive microwave observations of sea ice in the Bering and Greenland Seas, IEEE *Trans. Geoscience and Remote Sensing* GE-24,378-382, 1986.
Grenfell, T. C., and J. C. Comiso, Multifrequency passive microwave observations of first-year sea ice grown in a tank, IEEE *Trans. Geoscience and Remote Sensing*, GE-24, 826-831, 1986.
Grenfell, T. C., J. C. Comiso, M. A. Lange, H. Eicken, and M. R. Wenshahan, Passive microwave observations of the Weddell Sea during austral winter and early spring, *J. Geophys, Res*., 99(C5), 9995-10010, 1994.
Grenfell, T.C, D.J. Cavalieri, J.C. Comiso, M.R. Drinkwater, R.G. Onstott, I. Rubinstein, K Steffen, I. Rubinstein, D.P. Winebrenner, "Microwave signatures of new and young ice," Chapter 14, *Microwave Remote Sensing of Sea Ice*, (ed. by Frank Carsey), American Geophysical Union, Washington, D.C., 291-301, 1992.
Honda, M., K. Yamazaki, Y. Tachibana, and K. Takeuchi, Influence of Okhhotsk sea-ice extent on atmospheric circulation, *Geophysical Research Letters*, 23, 3595-3598, 1996.
Jacobs, S.S., and J.C. Comiso, A climate anomaly in the Amundsen and Bellingshausen Seas, *J. Climate*, *10*(4), 697-709, 1997.

Jacobs, S. and J. C. Comiso, Satellite passive microwave sea ice observations and oceanic processes in the Ross Sea, Antarctica, *J. Geophys.Res., 94*, 18195-18211, 1989.
Killworth, P. D., Deep convection in the world ocean, Rev. Geophys. and Space Phys. 21, 1-26, 1983.
King, J. C. and S. A. Harangozo, Climate change in the western Antarctic Peninsula since 1945: observations and possible causes, Annals of Glac., 27, 571-575, 1998.
König-Langlo, G., The meteorological data of the Georg-von-Neumayer-Station (Antarctica) for 1988, 1990, 1991, *Rep. Polar Research*, 116, 70 pp., Alfred-Wegener-Instiut für Polar- und Meeresforschung, Bremerhaven, Germany, 1992.
Kummerow, C., On the accuracy of the Eddington approximation for radiative transfer in the microwave frequencies, *J. Geophys. Res*, 98, 2757-2765, 1993.
Lubin, D., C. Garrity, R.O. Ramseier, and R.H. Whritner, Total sea ice concentration retrieval from the SSM/I 85.5 GHz channels during the Arctic summer, *Rem. Sens. Environ*., 62, 63-76, 1997.
Manabe, S. and R. J. Stouffer, Multiple-century response of a coupled ocean-atmosphere model to an increase of atmospheric carbon dioxide, *J. Climate*, 7(1), 5-23, 1994.
Markus, T. and D. J. Cavalieri, An enhancement of the NASA Team sea ice algorithm, *IEEE Trans. Geosci. and Remote Sensing*, 38, 1387-1398, 2000.
Markus, T. and D. J. Cavalieri, Snow depth distribution over sea ice in the Southern Ocean from satellite passive microwave data, Antarctic Sea Ice: Physical Processes, Interactions and Variability, Antarctic Research Series, Volume 74, pp 19-39, American Geophysical Union, Washington, DC, 1998.
Maslanik, J. A., Effects of weather on the retrieval of sea ice concentration and ice type from passive microwave data, *Int. J. Rem. Sens*., 13, 34-57, 1992.
Massom, R. and J. C. Comiso, The classification of Arctic sea ice types and the determination of surface temperature using advanced very high resolution radiometer data, J. Geophys. Res., 99, 5201-5218, 1994.
Massom, R.A., M.R. Drinkwater, and C. Haas, Winter snow cover on sea ice in the Weddell Sea, J. Geophys. Res., 102, 1101-1117, 1997.
Matzler, C., Passive microwave signatures of landscapes in winter, Met. Atm. Physics, 54, 241-260, 1994.
Matzler, C., R. O. Ramseier, and E. Svendsen, Polarization effects in sea ice signatures, IEEE J. Oceanic Engineering, OE-9, 333-338, 1984.
Maykut, G. A., Energy exchange over young ice in the central Arctic, J. Geophys. Res., 83(C7), 3646-3658, 1978.
Oelke, C., Atmospheric signatures in sea-ice concentration estimates from passive microwave: modeled and observed, *Int. J. Remote Sensing*, 18, 1113-136, 1997.
Onstott, R. G., T. C. Grenfell, C. Matzler, C. A. Luther, and E. A. Svendsen, Evolution of microwave sea ice signatures during early summer and midsummer in the marginal ice zone, J. Geophys. Res., 92, 6825-6835, 1987.
Parkinson, C. L., J. C. Comiso, H. J. Zwally, D. J. Cavalieri, P. Gloersen, and W. J. Campbell (1987), Arctic Sea Ice 1973- 1976 from Satellite Passive Microwave Observations, NASA Spec. Publ. 489, pp.296, 1987.
Parkinson, C. L., D. J. Cavalieri, P. Gloersen, H. J. Zwally, and J. C. Comiso, Variability of the Arctic Sea Ice Cover 1978-1996, *J. Geophys. Res*., 104, 20,837-20,856, 1999.

Preller, R. H., J. E. Walsh, and J. A. Maslanik, The use of satellite observations in ice cover simulations, Chapter 22, in Microwave Remoate Sensing of Sea Ice, F. D. Carsey (ed.), Geophysical Monograph 68, American Geophysical Union, Washington, DC, 1992
Rothrock, D. A., D. R. Thomas, A. S. Thorndike, Principal Component Analysis of satellite passive microwave data over sea ice, J. Geophys. Res., 93: 2321-2332, 1988.
Schluessel, P. and H. Grassl, SST in polynyas: A case study, International Journal of Remote Sensing, 11(6), pp.933-945, 1990.
Steffen, K. and A. Schweiger, NASA team algorithm for sea ice concentration retrieval from the Defense Meteo-rological Satellite Program Special SensorMicrowave Imager: Comparison with Landsat Imagery, J. Geophys. Res., 96(12), 21971-21987, 1991.
Stiles, W.H., and F.T. Ulaby, The active and passive microwave response to snow parameters, 1. wetness, J. Geophys. Res., 85, 1037-1044, 1980.
Stommel, H., On the smallness of sinking regions in the ocean, Proc. Nat. Acad. Sc., USA 48, 766-772, 1962.
Svendsen, E., K. Kloster, K., B. Farrelly, O. M. Johannessen, J. A. Johannessen, W. J. Campbell, P. Gloersen, D. J. Cavalieri, and C. Matzler, Norwegian Remote Sensing Experiment: Evaluation of the Nimbus 7 Scanning multichannel microwave radiometer for sea ice research, J. Geophys. Res., 88, 2781-2792, 1983.
Sturm, M., K. Morris, and R. Massom, The character and distribution of the winter snow cover on the sea ice of the Bellingshausen, Amundsen and Ross Seas, Antarctica, 1994-1995, Antarctic Sea Ice: Physical Processes, Interactions and Variability, Antarctic Research Series, Volume 74, pp 1-18, American Geophysical Union, Washington, DC, 1998.
Swift, C. T. and D. J. Cavalieri, Passive Microwave Remote Sensing for Sea Ice Research, EOS, Transactions, American Geophysical Union, 66, (49), Washington DC, 1985.
Swift, C. T., L. S. Fedor, and R. O. Ramseier, An algorithm to measure sea ice concentration with microwave ra-diometers, J. Geophys. Res., 90, 1087-1099, 1985.
Vowinckel, E., and S. Orvig, The climate in the north polar basin, in Climate of the Polar Regions, Vol.14 of World Survey of Climatology, Elsevier, Amsterdam, pp. 129-252, 1970.
Wadhams, P., W. Tucker, W. Krabill, R. Swift, J. Comiso, and N. Davis, The relationship between sea ice free-board and draft in the Arctic Basin, and implications for ice thickness monitoring, J. Geophys. Res., 97(C12), 20325-20334, 1992.
Wankiewicz, A., Multi-temporal microwave satellite observations of snowpacks, Ann. Glaciol., 17, 155-160, 1993.
Wensnahan, M., Maykut, G. A., Grenfell, T. C., and D. P. Winebrenner, Passive microwave remote sensing of thin sea ice using principal component analysis, J. Geophys. Res., 98, 12,453-12,468, 1993.
Wharton, S.W. and Y.C. Lu, The land analysis system: A general purpose system for multispectral image processing, Prodeedings of IGARSS87 Symposium, Ann Arbor, Michigan, 18-21, 1987.
Worby, A. P., and R. A. Massom, The structure and properties of sea ice and snow cover in East Antarctic pack ice, Antarctic CRC, Research report, 7, 191 pp., 1995.
Zwally, H. J., J. C. Comiso, C. L. Parkinson, W. J. Campbell, F. D. Carsey, F.D., and P. Gloersen, Antarctic sea ice, 1973-1976: satellite passive microwave observations, NASA SP-459, 1983.